Analytical and computational investigations in atomic attosecond physics

Dissertation
zur Erlangung des Doktorgrades
an der Fakultät für Mathematik, Informatik und Naturwissenschaften
Fachbereich Physikder
der Universität Hamburg

vorgelegt von

Daria Kolbasova

Hamburg

2021

Gutachter der Dissertation:	Prof. Dr. Robin Santra Dr. Sang-Kil Son
Zusammensetzung der Prüfungskommission:	Prof. Dr. Robin Santra Prof. Dr. Francesca Calegari Dr. Sang-Kil Son Dr. Christian Ott
Vorsitzende der Prüfungskommission:	Prof. Dr. Daniela Pfannkuche
Datum der Disputation:	August 10^{th}, 2021.
Vorsitzender Fach-Promotionsausschusses PHYSIK:	Prof. Dr. Wolfgang Hansen
Leiter des Fachbereichs PHYSIK:	Prof. Dr. Günter H. W. Sigl
Dekan der Fakultät MIN:	Prof. Dr. Heinrich Graener

Eidesstattliche Versicherung / Declaration on oath

Hiermit versichere ich an Eides statt, die vorliegende Dissertationsschrift selbst verfasst und keine anderen als die angegebenen Hilfsmittel und Quellen benutzt zu haben.

Hamburg, den 12.08.2021

Unterschrift der Doktorandin

Abstract

Understanding the interaction of matter with ultrashort attosecond light pulse provides fundamental insights into the structure of matter. The electronic properties are reflected in wave packets dynamics. The ability to trace the evolution of electrons in wave packets is a big challenge. It requires ultrashort pulse duration and precise pulse characterization. In this thesis the time-delayed scanning of the atom is used to (1) characterize the inner atomic dynamics, via excitation of the atom by a time-delayed attosecond extreme ultraviolet (XUV) and femtosecond optical field, and to (2) characterize a laser field, via multiphoton ionization of the atom by the autocorrelation function of the field.

The first part of the thesis explores the capability of attosecond transient absorption spectroscopy to characterize the dynamics of inner-shell-excited systems. I discuss an unusual kind of pump-probe experiment, where information is gained from the absorption spectrum of an attosecond XUV pulse, which serves as a pump pulse at the same time. The optical pulse in this kind of experiment gives a reference time that provides a possibility to measure the time evolution of a system of interest. In the study, I use different theoretical approaches, treating one or both of the pulses as perturbative or non-perturbative. I present an analytical theory of attosecond transient absorption spectroscopy for perturbatively dressed systems and illustrate how the attosecond transient absorption signal reveals the real-time attosecond dynamics of the atom. In addition, I apply our study to atomic Xe and compare the theoretical predictions with experimental results.

In the second part of the thesis a new method for laser pulse characterization is presented. It is based on a machine learning algorithm and is used to study multiphoton autocorrelations in Ar. I analyze the time-delay dependence of the ionization probability for given laser pulse parameters, such as photon energy, pulse intensity and pulse duration. Taking into consideration the mapping between the ionization-probability time-delay pattern and pulse parameters I use a machine-learning algorithm to retrieve the best approximation function for the laser pulse from experimentally measured multiphoton autocorrelation in Ar.

Deutsche version:

Zusammenfassung

Das Verständnis der Wechselwirkung von Materie mit ultrakurzen Attosekunden-Lichtpulsen liefert grundlegende Einsichten in die Struktur von Materie. Die elektronischen Eigenschaften zeigen sich in der Dynamik von Wellenpaketen. Die Entwicklung der Elektronen in Wellenpaketen zu verfolgen, stellt eine große Herausforderung dar. Ultrakurze Pulsdauern und präzise Puls-Charakterisierung sind dafür erforderlich. In dieser Arbeit wird das zeitverzögerte Scannen des Atoms verwendet, um (1) die inneratomare Dynamik zu charakterisieren, durch Anregung des Atoms mit einem zeitverzögerten Attosekunden-Feld im extrem ultravioletten (XUV) Bereich und einem Femtosekunden-Feld im optischen Bereich. Das zeitverzögerte Scannen des Atoms wird darüber hinaus dazu verwendet, um (2) das Laserfeld zu charakterisieren, über Multiphotonen-Ionisation des Atoms durch die Autokorrelationsfunktion des Feldes.

Der erste Teil der Arbeit untersucht das Potenzial der transienten AttosekundenAbsorptionsspektroskopie im Hinblick auf die Charakterisierung der Dynamik von Innerschalenangeregten Systemen. Ich diskutiere eine ungewöhnliche Art von Pump-Probe-Experiment, bei dem Information aus dem Absorptionsspektrum eines Attosekunden-XUV-Pulses gewonnen wird, welcher gleichzeitig auch als Anregungspuls dient. Der optische Puls in dieser Art von Experiment liefert eine Referenzzeit und so die Möglichkeit, die Zeitentwicklung eines Systems von Interesse zu messen. In der Studie verwende ich unterschiedliche theoretische Ansätze, die einen oder beide Pulse störungstheoretisch oder nicht-störungstheoretisch behandeln. Ich stelle eine analytische Theorie zu transienter Attosekunden-Absorptionsspektroskopie für störungstheoretisch beeinflusste Systeme vor und zeige auf, wie das transiente Attosekunden-Absorptionssignal die Echtzeit-AttosekundenDynamik des Atoms offenbart. Überdies wird die Theorie auf atomares Xe angewandt und die theoretischen Vorhersagen werden mit experimentellen Ergebnissen verglichen.

Im zweiten Teil der Arbeit wird eine neue Methode zur Laserpuls-Charakterisierung präsentiert. Sie basiert auf einem Algorithmus für maschinelles Lernen und wird

verwendet, um MultiphotonenAutokorrelationen in Ar zu untersuchen. Die Abhängigkeit der Ionisationswahrscheinlichkeit von der Zeitverzögerung wird für bestimmte Laserpulsparameter analysiert, wie Photonenergie, Pulsintensität und Pulsdauer. Unter Berücksichtigung der Zuordnung zwischen Ionisationswahrscheinlichkeits-Zeitverzögerungsmuster und Pulsparametern wende ich einen Algorithmus für maschinelles Lernen an, um die beste Näherungsfunktion für den Laserpuls zu finden, ausgehend von experimentell gemessener Multiphotonen-Autokorrelation in Ar.

Contents

List of Publications

1. *"Analytical Theory of Attosecond Transient Absorption Spectroscopy of Perturbatively Dressed Systems"*,
   D. Kolbasova and R. Santra, *Appl. Sci.* **9**, 1350 (2019).

2. *"Probing ultrafast coherent dynamics in core-excited xenon by using attosecond XUV-NIR transient absorption spectroscopy"*,
   D. Kolbasova, M. Hartmann, R. Jin, A. Blättermann, C. Ott, S.-K. Son, T. Pfeifer and R. Santra, *Phys. Rev. A* **103**, 043102 (2021).

List of Abbreviations

ATAS	**A**ttosecond **T**ransient **A**bsorption **S**pectroscopy
ATA	**A**ttosecond **T**ransient **A**bsorption
XUV	e**X**treme **U**ltra**V**iolet
UV	**U**ltra**V**iolet
NIR	**N**ear **I**nfra**R**ed
TDCIS	**T**ime-**D**ependent **C**onfiguration-**I**nteraction-**S**ingles
XCID	**C**onfiguration-**I**nteraction **D**ynamics package
HF	**H**artree **F**ock
CI	**C**onfiguration **I**nteraction
MCDF	**M**ulti**C**onfiguration **D**irac-**F**ock
HHG	**H**igh **H**armonic **G**eneration
MATLAB	**MAT**rix **LAB**oratory
LAPACK	**L**inear **A**lgebra **PACK**age
GS	**G**round **S**tate
DS	**D**ark **S**tate
BS	**B**right **S**tate
LIS	**L**ight **I**nduced **S**tate

Dedicated to my beloved grandfather

Chapter 1

Introduction

The key mechanisms that provide ways to observe and control the complicated dynamics inside of an atom are electron excitations and ionizations, induced by ultrashort laser pulses [1]. As a many-particle system evolves, the time scale of the electronic motion is determined by the energy difference between the electronic states that the electron evolves into. Since the typical energy difference between the electronic states of molecules and atoms is in the range of 0.1 - 100 eV, the corresponding time scales lie in the range of 0.05 - 50 fs. The rapid technological progress in building lasers with attosecond light pulses [2, 3, 4, 5, 6] has opened up the possibility of studying fundamental questions related to the quantum dynamics of electrons on their natural time scale and explore fundamental mechanisms in chemical and physical processes in a time-resolved manner [7]. The attosecond physics community is closely tied to the strong-field physics community since intense laser pulses are involved, especially in the generation of attosecond pulses. In this context several review articles have been written in strong-field physics [8, 9, 10, 11, 12] and attosecond physics [13, 14, 15], which focus more on ionization processes and system dynamics, respectively.

More than a decade after the generation of isolated attosecond extreme ultraviolet (XUV) pulses, various types of attosecond spectroscopy have been developed to investigate time-resolved electron dynamics in a variety of systems ranging from noble gas atoms and polyatomic molecules to metallic, dielectric, and semiconducting materials. This technology is now being extended to study more complex gas-phase and solid-state phenomena, primarily caused by strong electron correlation effects [16, 17, 18, 19]. Broadband attosecond XUV pulses provide multiple electronic excitations in a system, which gives an opportunity to reveal quantum interferences

and determine the lifetimes of short-lived states.

One of the most effective methods for time-resolved studies is the pump-probe experiment [20]. In such a pump-probe setup, the first light pulse (pump) initiates the dynamics being studied and the interaction with the second light pulse (probe) probes it. By scanning the delay time between the two pulses one obtains a sequence of probe measurements that can be seen as a movie of the pump-induced dynamics. The time resolution in pump-probe approaches is determined mostly by the ability to accurately control the pump-probe delay τ, which can be already measured up to subattosecond precision [21].

Various physical processes can be studied, depending on the intensity and photon energy, and the specific combination of pump and probe pulses. Most of attosecond pump-probe experiments use a femtosecond near-infrared (NIR) pulse and an attosecond ultraviolet (UV) pulse [1]. Either pulse can be used as a pump or as a probe pulse. NIR pulses are usually strong-field pulses, which lead to non-perturbative tunnel ionization. UV pulses, on the other hand, generally lead to electronic excitation and to perturbative ionization. To date, a number of attosecond experiments have involved strong-field interaction with a few-cycle laser pulse and a perturbative interaction with an attosecond XUV pulse [22]. Understanding results from these experiments is nontrivial and often requires high-level theoretical calculations to model strong-field light-matter interactions that significantly affect the electronic states of the system.

A common measure for characterizing the nature of field-induced ionization is the Keldysh parameter γ [23], which is given by

$$\gamma = \sqrt{\frac{I_p}{2U_p}}, \tag{1.1}$$

where I_p is the ionization potential of the electronic state and $U_p = E^2/(4\omega^2)$ is the ponderomotive potential, which is the average energy of a free electron oscillating in the electric field with amplitude E and frequency ω. The Keldysh parameter distinguishes between two ionization regimes: perturbative ($\gamma \gg 1$) and non-perturbative ($\gamma \ll 1$) multiphoton ionization (or tunneling). However, γ alone is not always a sufficient measure to reveal whether ionization is perturbative or non-perturbative [24]. In particular, at photon energies comparable or larger than

the ionization potential ($\omega \gtrsim I_p$) the ionization process is rather more accurately described by a perturbative picture also for $\gamma < 1$, contrary to what the Keldysh parameter would suggest. In general, for the case of ($\gamma \gg 1$), the ionization lies in the perturbative regime and the light-matter interaction can be seen as a correction to the field-free system. The system gets ionized by absorbing a certain number of photons and the final state of the system is a result of a countable and well-defined number of light-matter interactions. These n light-matter interactions are exactly captured by the n^{th} - order perturbation correction. In case of the non-perturbative regime $\gamma \ll 1$, the light-matter interaction can be considered as a local potential that strongly distorts the Coulomb potential and already after a few Bohr radii the field-induced potential starts to dominate the motion of the electrons. In this regime it is reasonable to treat the Coulomb potential of the system rather than the field as the perturbation. This distortion of the Coulomb potential by the electric field creates a potential barrier, which can be overcome by the electron by tunneling through this barrier and, consequently, out of the system. The Coulomb potential becomes negligible for an electron once it has tunneled to the outer side of the barrier, and its dynamics are governed by the field-induced potential. In pump-probe experiments, where strong-field ionization is induced by an optical pump pulse, and the XUV pulse serves as a probe, information on the strong-field induced dynamics in the residual ion can be obtained, such as ion quantum-state distributions [25, 26] and orbital alignment [27, 28]. At lower field strengths, when the XUV pulse is the pump and the optical field acts as the probe, laser-dressing and molecular alignment effects may be investigated [29, 30, 31, 32, 33, 15, 34, 35, 36].

1.1 Transient absorption spectroscopy

A pump-probe delay experiment can measure the spectral properties of a probe pulse, which are transmitted through a sample excited by a pump pulse [37, 38, 39, 40, 41, 42, 43, 44, 45, 46, 47, 48, 49, 50, 51]. This technique is called transient absorption spectroscopy [52, 53, 54, 55] because the information is obtained from the absorbed/transmitted light. It is a versatile method that can be used to study real-time dynamics in various states of matter like gas, liquid, and plasma phases.

Initially, transient absorption spectroscopy has been used on the femtosecond time scale for probing solid state systems [56] and chemicals [57, 58]. However, with

the advent of attosecond light pulses [2, 3, 4, 5, 6], it has been extended into the attosecond regime as well [59, 60]. There are two important factors that determine the quality of the time resolution: the duration of the probe pulse and the variation of time delay from pulse to pulse in the pump-probe delay. Due to the advancement in attosecond technology, especially in controlling the phase of single frequency components in ultrashort pulses, this uncertainty has been decreased up to a few femtoseconds.

By using attosecond pulses, not only does one obtain high attosecond resolution, but also a broad frequency spectrum, due to their short duration. Using the broad spectrum, we can access different atomic excitations with a single pulse. This allows one, for example, to access the phase relations between the different probed electronic states. The coherent superposition of quantum states leads to the dynamical evolution of the system under investigation. This coherent superposition is a result of an attosecond pulse which coherently populates bright (dipole allowed) electronic states creating an electronic wave packet. Each system under investigation has a characteristic time scale at which its physical properties vary in accordance with the frequency spacing between the coherently excited states of the wave packet. In literature we can find a number of studies regarding pump-probe pulses to investigate Rydberg-electron dynamics in atoms [59, 61, 62, 63, 64, 65, 66, 67]. The studies reveal that electronic coherences were seen under various conditions ranging from one-photon one-electron excitations, multiphoton one-electron excitation to one-photon two-electron excitation. In these studies, the key point in probing the wave packet was light-induced interference of the investigated states. This leads to the modulation of those quantities that are experimentally observed, i.e., the transmitted photons or the emitted photoelectrons. In the aforementioned studies, a missing factor for the characterization of electronic wave packets is that it has only been limited to the excited valence or Rydberg electron, but not to the deeply bound electrons or the corresponding holes. Extending the observation of electronic coherences to deeply bound electronic states one can expect it to serve as a marker in site-selective and element-specific studies of complex systems.

In our studies [68, 69], we address the possibility for the experimental observation of core-excited wave-packet coherence by attosecond transient absorption spectroscopy (ATAS) of atoms. We initiate a core-excited wave packet by using an attosecond XUV pulse. A time-delayed ultrashort laser pulse in the NIR regime is

considered to probe the wave packet and thus monitor its time evolution. We detect the resulting modification of the transmitted XUV spectrum. The aim of our study is to explore XUV-NIR transient absorption spectra and to validate as to whether excited-electron dynamics or inner-shell hole dynamics are encoded in the time-resolved spectra. We employ a complete theoretical analysis in order to completely understand and maximize the information content [70, 60, 71, 72, 73, 67, 74, 75, 76, 77, 78] of the attosecond transient absorption signal. We provide insight through elementary explanations of the signals observed in attosecond transient absorption (ATA) experiments. We demonstrate that various aspects of coherent electron dynamics can be revealed when wave packets prepared by an attosecond pump pulse are probed using an NIR pulse. We show that the presence of a dressing field or a slight modification of the spectrum of the probe pulse can dramatically change the simulated ATAS results. Thus, our work also suggests that a precise NIR pulse characterization in the target region is necessary for a qualitatively and quantitatively accurate interpretation of experimental ATAS data, due to the high sensitivity of Rydberg electrons to the NIR electric fields.

1.2 Pulse characterization

A comprehensive characterization of laser beams is of great importance [79]. However, an accurate characterization of ultrashort picosecond or femtosecond pulses is known to be difficult due to the slow operation of the electronic devices. Photodiodes and oscilloscopes provide at best a response time of 200 fs approximately, whereas laser pulses can be as short as few femtoseconds. Alternatively, laser pulses can be analyzed using autocorrelators. There are devices for measuring the autocorrelation function of the pulse's electric field or its intensity. An autocorrelation function is described by the correlation of a signal with a delayed copy of itself as a function of delay. The basic principle of an autocorrelator operation is to check the correlation of the temporal pulse trace with itself when a beam splitter creates two copies of the incoming pulse, which are superimposed in a nonlinear medium. The interaction between the two is based on some non-linearity, while a necessary condition is to have a temporal overlapping between the two. In principle it sounds simple, however it is complicated to measure the duration of the pulse with an autocorrelation trace being unaware of the pulse shape. This is due to the fact that the information about the phase profile is not provided by most of the intensity

autocorrelation techniques. For very short pulses with a duration below 10 fs, accurate autocorrelation measurements are difficult to perform due to limited phase-matching bandwidth of the nonlinear crystal, even if these crystals are constructed really thinly.

I have developed a method based on a machine learning algorithm for the characterization of laser pulses by analyzing the ionization probability of Argon (Ar) gas by time-delayed replicas of the laser field. It exploits the autocorrelation technique for measuring the pulse parameter as was suggested by Prof. F. Calegari and Dr. A. Trabattoni. As a first step our method requires theoretical simulation of the multiphoton autocorrelation for a larger variety of pulse parameters. Multiphoton autocorrelations were calculated with the time-dependent configuration-interaction singles (TDCIS) approach (see Chapter 2). Exposing a gas to a strong laser field one can excite or ionize its atoms. The probability of ionization depends on the pulse parameters, such as photon energy, pulse intensity, and pulse duration. These parameters can directly be extracted from the laser field autocorrelation function. Further I have trained a machine learning model to these data and eventually have obtained a tool to retrieve pulse parameters from observed ionization probabilities. Exploiting the unknown functional relationship between the combination of these parameters and the ionization probability, I use a machine-learning algorithm to model the multiphoton autocorrelation in Ar to retrieve the best approximation function for the laser pulse.

1.3 Structure of the thesis

This work consists of two main parts that discuss important aspects of attosecond science, respectively. The first part is devoted to a theoretical study of physical processes inside the atom and exploring the capabilities of ATAS to monitor deep inner-shell dynamics. In the transient absorption spectroscopy setup considered, wave packets are prepared by an attosecond XUV pulse and probed by a femtosecond NIR pulse. I clarify which aspects of the dynamics can be revealed when the wave packets are probed using an NIR pulse, and which are more difficult to detect — excited-electron dynamics or inner-shell hole dynamics. I also investigate the effect of an additional NIR dressing field on the transient absorption spectrum.

In the second part I present a new method for pulse characterization, which is based on a machine learning technique. This method is based on the dependence of ion yields on the laser autocorrelation function. I perform ab-initio calculations of the Ar gas ionization by the overlapping femtosecond laser fields, and use these data to train the machine learning algorithm for precise characterization of the field.

In Chapter 2 I provide a theoretical background of the *ab-initio* simulation of a light-matter interaction and, in particular, the background of the time-dependent configuration-interaction-singles approach.

In Chapter 3 I focus specifically on the theory of ATAS for overlapping pump and probe pulses. The theory is derived for pump-probe experiment, where the information is gained from the absorption spectrum of an attosecond XUV pulse, which serves as a pump pulse at the same time, whereas the optical probe pulse gives a reference time that provides a possibility to measure the time evolution of a system of interest.

In Chapter 4 I illustrate the basic features of the ATAS experiment by applying the analytical expressions obtained in Chapter 3 to an artificial few-level system characterized by level spacings matching XUV and optical energies. By focusing on a simple few-level atom, I perform an analysis of the ATA signal dependence on the time decay between the attosecond XUV pulse and the optical dressing pulse. An elementary explanation of the signals one can obtain in such experiments is provided.

In Chapter 5 I present the numerical simulation of ATAS experiment for a Xe atom. I provide a comparison of our theoretical predictions with experiment and discuss the importance of the careful characterization of the pulse when studying real-time attosecond dynamics of the electrons inside the atom.

In Chapter 6 I explore the multiphoton autocorrelation in Ar. I present the analysis of a big set of calculations performed using TDCIS approach in order to study the ionization-probability delay-patterns dependence on parameters of the autocorrelated field. Analysis of these delay patterns allowed to approximate them with a rather simple function of a few parameters, which are eventually used for a pulse characterization.

In Chapter 7 I present the machine learning technique for the characterization of the femtosecond laser pulses using multiphoton autocorrelation in Ar.

1.4 My Contributions

1.4.1 Theoretical contributions

An analytical theory of ATAS was derived for perturbatively dressed systems. This theory is applicable to the analysis of processes observed in pump-probe experiments if both pump and probe fields are sufficiently weak. A two-stage approach based on perturbation theory was used to obtain an analytical expression for the attosecond-resolved transient absorption signal.

1.4.2 Code development

Based on the resulting analytical expressions a MATLAB code was written that allows the simulation of a transient absorption spectroscopy signal and explore the physical reasons behind certain parts of the signal in detail. Several different routines were written to efficiently compute the results and produce plots.

Another MATLAB code was written that allows to carry out similar simulations by solving the time-dependent Schrödinger equation numerically. Non-perturbative treatment of an optical pulse allows us to perform calculations for any shape of the optical pulse. In addition, the code includes an option to add multiple optical fields, which can be temporally centered arbitrarily - the middle of the pulse can be fixed relative to the attosecond pump pulse or can be shifted with the time delay. This flexibility allows for experiments to be reproduced more thoroughly.

1.4.3 Machine learning modeling

In order to have a proper characterization of the pulse, a python based code was developed and implemented. It uses a machine learning algorithm to analyze and reconstruct the shape of a laser pulse from the probability of its autocorrelation function to ionize argon gas. This code is based on modern machine learning algorithm implementations using libraries like scikit-learn, pandas, matplotlib and

seaborn. The regression method was employed along with the grid search cross-validation for the tuning of the hyper-parameters. Given a set of ion yields, the training model provides a careful characterization of the pulse, allowing for the retrieval of the pulse intensity, spectrum and the chirp, which can appear as the pulse travels through the lenses and mirrors, which may significantly modify the pulse duration.

Chapter 2

Theoretical Background

The analysis of the absorption and emission of electromagnetic radiation is a powerful method for exploring the quantum world of atoms and molecules. The ability to produce well-defined laser pulses provides an opportunity to study the underlying structure and mechanisms of these microscopic systems with a very high resolution. By knowing the spectrum of the radiation pulse as it enters the system, it is possible to establish a direct relationship between the final spectrum of the pulse after having passed through the system and the internal structure of the system.

My work is devoted to the theoretical study of the electron dynamics inside an atom using ultrashort electromagnetic pulses. This requires the solution of the time-dependent Schrödinger equation. In my research, I use an ab-initio approach when performing the calculations with the configuration interaction dynamics package for multichannel dynamics (XCID) code [80], and when deriving a theory for attosecond transient absorption spectroscopy of a dressed system [68, 69].

The XCID code is ideal for the simulation of strong-field interactions with an atom. In our work, we use it to calculate the probability of multiphoton ionization of an atom. However, it is not suited to use this approach to study the dynamics of atomic deep shells, which is the subject of the first part of our work. Since the XCID code does not fully take into account relativistic effects, some information may be lost and the data obtained can be misleading. Therefore, we derive a theory for ATAS employing an atomic model built within the relativistic Dirac-Fock approach thus allowing us to take into account relativistic effects.

2.1 Time-dependent Schrödinger equation

A nonstationary processes driven in a system by an electromagnetic field can be described with the time-dependent Schrödinger equation (TDSE)

$$i\frac{\partial}{\partial t}|\Psi,t\rangle = \hat{H}(t)|\Psi,t\rangle, \tag{2.1}$$

where $\hat{H}(t)$ is the Hamiltonian and $|\Psi,t\rangle$ is the wave function of the system. The atom under consideration is a multi-electron system and its electrons are interacting with each other due to the Coulomb interaction among them. The dynamics of any given electron thus depends on the dynamics of all the other electrons in the system. A precise description of electron correlations remains a difficult task, although their importance for physical and chemical properties had been realized already in the early years of quantum mechanics. The exact wave function is analytically not known even for the simplest multielectron system, that being the helium atom, containing two electrons. For any realistic system, the exact N-electron wave function needs to be approximated to make it computationally tractable. In the commonly used mean-field approximation the N electrons are treated as being independent, but interact with each other via a common mean-field potential.

2.2 Mean-field approximation

The Hartree–Fock (HF) method is one of the most popular theories, that treats many-body electronic states based on a mean-field approximation, where the N-electron wave function $|\Psi\rangle$ is approximated as a single Slater determinant, $|\Phi\rangle$, comprised of one-particle wave functions $|\phi_n\rangle$:

$$|\Psi\rangle \approx |\Phi\rangle = \frac{1}{\sqrt{N!}}\begin{vmatrix} \phi_1(r_1) & \phi_1(r_2) & ... & \phi_1(r_N) \\ \phi_2(r_1) & \phi_2(r_2) & ... & \phi_2(r_N) \\ ... & ... & ... & ... \\ \phi_N(r_1) & \phi_N(r_2) & ... & \phi_N(r_N) \end{vmatrix}. \tag{2.2}$$

The set of one-particle functions ϕ_n is obtained by minimizing the electronic energy $E = \langle\Phi|\hat{F}|\Phi\rangle$ resulting in the Hartree-Fock equation

$$\hat{F}|\phi_n\rangle = \varepsilon_n|\phi_n\rangle. \tag{2.3}$$

The Fock operator reads

$$\hat{F} = \hat{T} + \hat{V}_{\text{nuc}} + \hat{V}^H(\mathbf{r}) + \hat{V}^x(\mathbf{r}), \tag{2.4}$$

where the kinetic energy operator $\hat{T} \equiv \sum_{n=1}^{N} \hat{\boldsymbol{p}}_n^2/2$, and the nucleus-electron interaction $\hat{V}_{\text{nuc}} \equiv -\sum_{n=1}^{N} Z/|\hat{\boldsymbol{r}}_n|$. The Hartree potential

$$\hat{V}^H(\mathbf{r}) = \sum_{n=1}^{N} \int d^3\mathbf{r}' \frac{|\phi_n(\mathbf{r}')|^2}{|\mathbf{r} - \mathbf{r}'|} \tag{2.5}$$

together with the last term $V^x(\mathbf{r})$ describes electron interactions with each other and compose the mean-field potential $V_{MF}(\mathbf{r}) = \hat{V}^H(\mathbf{r}) + \hat{V}^x(\mathbf{r})$. The last term $\hat{V}^x(\mathbf{r})$ is the exchange interaction operator. In Hartree-Fock approach the exchange interaction is a nonlocal one-particle operator

$$\hat{V}^x(\mathbf{r})\phi_i(\mathbf{r}) = -\sum_{k=1}^{N} \int d^3\mathbf{r}' \frac{\phi_k^*(\mathbf{r}')\phi_i(\mathbf{r}')\phi_k(\mathbf{r})}{|\mathbf{r} - \mathbf{r}'|}. \tag{2.6}$$

Hartree-Fock method can be simplified into Hartree-Fock-Slater by replacing the exchange interaction with a local potential,

$$\hat{V}^x(\mathbf{r}) = -\frac{3}{2}\left[\frac{3}{\pi}\sum_{k=1}^{N}|\phi_k(\mathbf{r})|^2\right]^{1/3}. \tag{2.7}$$

The set $\{\phi_n\}$ has to be optimized for each different electronic configuration under consideration. Self-consistency of the HF solution is achieved when the HF equations are satisfied for all orbitals $|\phi_n\rangle$.

The Hartree-family methods usually overestimate the energy of the ground state by an amount known as the correlation energy, which plays an important role in

many chemical problems. The multiconfiguration Hartree-Fock approach avoids this problem considering a linear combination of Slater determinants to approximate the N-electron wave function. This brings the model closer to the full N-body problem, and, in the limit of an infinite number of determinants, recovers the real ground state energy.

The full N-electron Hamiltonian including the light-matter interaction is given by

$$\hat{H}(t) = \sum_{n=1}^{N} \left(\hat{T} + \hat{V}_{nuc} + \hat{V}_{MF}(\boldsymbol{r}) \right) + \hat{H}_1 + \hat{\boldsymbol{p}}\boldsymbol{A}(\boldsymbol{r}, t), \tag{2.8}$$

where

$$\hat{H}_1 = \frac{1}{2} \sum_{n \neq n'}^{N} \frac{1}{|\hat{\boldsymbol{r}}_n - \hat{\boldsymbol{r}}_{n'}|} - \sum_{n=1}^{N} \hat{V}_{MF}(\boldsymbol{r}), \tag{2.9}$$

denotes the many-electron part, which describes the Coulomb interactions beyond the HF mean-field level. The light-matter interaction is described within the velocity form $\hat{\boldsymbol{p}}\boldsymbol{A}(\boldsymbol{r}, t)$, where $\boldsymbol{A}(\boldsymbol{r}, t)$ is the vector potential of the electromagnetic field and $\hat{\boldsymbol{p}}$ is a momentum. Here we make a dipole approximation, thus $\boldsymbol{A}(\boldsymbol{r}, t) \rightarrow \boldsymbol{A}(t)$.

A convenient basis set must be found in order to solve the electronic structure problem in which the wave function can be expanded. A big disadvantage of quantum many-body theories is that they quickly become too hard to be solvable on a computer, and the amount of correlation that can be described has to be restricted. The time-dependent-configuration-interaction-singles (TDCIS) approach is an ab-initio electronic-structure technique, where the time-dependent wave function is restricted to single particle-hole excitations from the ground-state determinant into spin-singlet configurations.

2.3 Time-Dependent-Configuration-Interaction-Singles

The configuration-interaction (CI) method is based on the idea that an N-electron state is expressed as a linear combination of the HF ground state $|\Phi_0\rangle$ and all possible n-particle-n-hole (np-nh) configurations $|\Phi^{a_1\dots a_n}_{i_1\dots i_n}\rangle$,

$$\begin{aligned}|\Psi(t)\rangle &= \left(\alpha_0(t) + \sum_{n=1}^{N}\sum_{\substack{a_1<\dots<a_n\\ i_1<\dots<i_n}}^{n} \alpha^{a_1\dots a_n}_{i_1\dots i_n}(t)\hat{c}^\dagger_{a_1}\hat{c}_{i_1}\dots\hat{c}^\dagger_{a_n}\hat{c}_{i_n}\right)|\Phi_0\rangle \\ &= \underbrace{\alpha_0(t)|\Phi_0\rangle}_{\text{ground state}} + \underbrace{\sum_{a_1,i_1}\alpha^{a_1}_{i_1}(t)|\Phi^{a_1}_{i_1}\rangle}_{\text{singles 1p-1h}} + \underbrace{\sum_{\substack{a_1<a_2\\ i_1<i_2}}\alpha^{i_1 i_2}_{a_1 a_2}(t)|\Phi^{i_1 i_2}_{a_1 a_2}\rangle}_{\text{doubles 2p-2h}} + \underbrace{\dots}_{\text{multiples np-nh}}.\end{aligned} \tag{2.10}$$

In the Full-CI method all np-nh configurations are included, providing in such a way an exact N-electron wave function.

Within the CI-Singles (CIS) approach, only one-particle—one-hole excitations $|\Phi^a_i\rangle$ with respect to the Hartree-Fock ground state $|\Phi_0\rangle$ are considered. Therefore, the wave function is expanded in the CIS basis as

$$|\Psi(t)\rangle = \alpha_0(t)|\Phi_0\rangle + \sum_{a,i}\alpha^a_i(t)|\Phi^a_i\rangle, \tag{2.11}$$

where the index i symbolizes an initially occupied orbital and a denotes an unoccupied (virtual) orbital, which the particle can be excited into. Specifically, the singlet excitations,

$$|\Phi^a_i\rangle = \frac{1}{\sqrt{2}}\left(c^\dagger_{a\uparrow}c_{i\uparrow} + c^\dagger_{a\downarrow}c_{i\downarrow}\right)|\Phi_0\rangle, \tag{2.12}$$

are considered here, where the operators $c^\dagger_{p\sigma}$ and $c_{p\sigma}$ create and annihilate electrons, respectively, in the spin orbitals $|\phi_{p\sigma}\rangle$, with p and σ denoting indices for the spatial and spin part of the wave function.

Inserting the wave function expansion [Eq. (2.11)] into the Schrödinger equation [Eq. (2.1)] and projecting onto the states $|\Phi_0\rangle$ and $|\Phi_i^a\rangle$ yields

$$i\dot{\alpha}_0(t) = \boldsymbol{A}(t) \sum_{i,a} \langle \Phi_0 | \hat{\boldsymbol{p}} | \Phi_i^a \rangle \alpha_i^a(t), \tag{2.13}$$

$$\begin{aligned} i\dot{\alpha}_i^a(t) =& (\varepsilon_a - \varepsilon_i)\alpha_i^a(t) + \sum_{j,b} \langle \Phi_i^a | \hat{H}_1 | \Phi_j^b \rangle \alpha_j^b(t) \\ &+ \boldsymbol{A}(t) \left(\langle \Phi_i^a | \hat{\boldsymbol{p}} | \Phi_0 \rangle \alpha_0(t) + \sum_{j,b} \langle \Phi_i^a | \hat{\boldsymbol{p}} | \Phi_j^b \rangle \alpha_j^b(t) \right), \end{aligned} \tag{2.14}$$

where ε_p denotes the energy of the orbital $|\phi_p\rangle$ (see Eq. 2.3.).

In our calculations we use the XCID program package [80], which employs the TD-CIS method to calculate time-resolved quantum wavepacket dynamics triggered by electric field pulses. The differential equations (2.13) and (2.14) in XCID code are solved by numerical time propagation using either the fourth order Runge-Kutta algorithm or the Lanczos propagation. Thus, the coefficients $\alpha_i^a(t)$ can be used to analyze ionization and excitation processes in a channel-resolved manner. In this way, quantities that can be inferred from the N-electron wave function, such as the ionization probability, cross sections, and other quantities can be calculated. In order to retrieve an ionization or excitation probability of the atom we use a special quantity provided by XCID code: the ion density matrix [80, 81],

$$\rho_{IDM}(t) = \mathrm{Tr}_\alpha \Big[|\Psi(t)\rangle\langle\Psi(t)| \Big], \tag{2.15}$$

which entails information about the statistical state of the full system. Here Tr_α stands for the trace over al virtual orbitals α.

2.4 Spin-orbit coupling in XCID

In large atoms, whose Z is comparable to the speed of light $c \approx 137$ (in atomic units), core electrons reach relativistic speeds. This causes a length contraction which affects the screening of the attractive nuclei potential by the core electrons. This has important consequences for the valence electrons and the chemistry of large Z-elements. In order to treat heavy atoms appropriately it is, in particular, necessary to include relativistic spin-orbit splitting in the Hamiltonian. In the XCID treatment

spin-orbit splitting is introduced for the occupied orbitals. The degenerate-state perturbation theory is used to treat spin-orbit coupling within the (n, l)-subshell. The occupied orbitals ϕ_i that are approximate eigenstates to the spin-orbit coupled Hamiltonian with quantum numbers $i = (n_i, l_i, s_i, j_i, m_i^j)$ can be written as

$$\phi_i(r,\theta,\varphi) = \frac{u_i^{n_i,l_i}(r)}{r} \begin{pmatrix} \langle l_i, m_i - \frac{1}{2}; \frac{1}{2}, +\frac{1}{2} | j_i, m_i \rangle Y_{l_i, m_i - \frac{1}{2}}(\theta,\varphi) \\ \langle l_i, m_i + \frac{1}{2}; \frac{1}{2}, -\frac{1}{2} | j_i, m_i \rangle Y_{l_i, m_i + \frac{1}{2}}(\theta,\varphi) \end{pmatrix}. \tag{2.16}$$

The radial $u^{n,l}(r)$ and spherical $Y_{l,m}(\theta,\varphi)$ parts are given by the non-relativistic HF model. For the virtual orbitals the derivative of the potential decreases rapidly such that spin-orbit splitting decreases and may be neglected. The optimal representation for the virtual orbital is, therefore, $a = (n_a, l_a, s_a, m_a^l, m_a^s)$. Specifically, the $|n_a, l_a, s_a, m_a^l\rangle$ doublet is given

$$\phi_a(r,\theta,\varphi) = \frac{u_a^{n_a,l_a}(r)}{r} Y_{l_a,m_a^l}(\theta,\varphi) \begin{pmatrix} \delta_{m_a^s,\frac{1}{2}} \\ \delta_{m_a^s,-\frac{1}{2}} \end{pmatrix} \tag{2.17}$$

The XCID framework was developed on the basis of non-relativistic electronic-structure theory, and artificially introduced spin-orbit coupling affects exclusively the hole, not the particle. Thus, some electron dynamics inside of an atom that may be observed in a real experiment when studying inner-shell electron dynamics are not covered in the simulations. In contrast, in relativistic atomic structure, only total momentum J and parity P are conserved by the atomic (light-unperturbed) Hamiltonian, and unless the excited electron is ionized, the angular momentum j of the hole is not conserved. To be able to capture the relativistic effects in ATAS we perform analytical and numerical calculations, in which the atomic model we use is built using the multiconfiguration Dirac-Hartree-Fock method.

2.5 Dirac–Fock-Slater method in FAC

For a fully relativistic treatment of the electrons, one should use quantum electrodynamics. But this very precise theory is also extremely complex for all but the simplest systems. Therefore, we use approximate Hamiltonians to avoid working in the full Fock space of quantum electrodynamics. The relativistic analogue of the

Hartree–Fock self-consistent field method is the Dirac–Hartree–Fock method. The multiconfiguration Dirac-Fock model is obtained by using the Dirac operator

$$H_D = \beta mc^2 + c\sum_{i=1}^{3} \alpha^i p_i, \tag{2.18}$$

where m is a mass of a particle, p_i are the components of its momentum operator, and c is the speed of light. It incorporates relativistic effects into the Hartree-Fock model. The energy levels of an atom with N-electrons are obtained by diagonalizing the relativistic Fock matrix

$$\hat{H}_R = \sum_{i=1}^{N} \hat{H}_D(i) + \hat{V}_{nuc} + \hat{V}_{MF}(\hat{\boldsymbol{r}}). \tag{2.19}$$

Both Hartree–Fock and Dirac–Hartree–Fock methods are independent particle models where each electron "feels" the field of nuclei $\hat{V}_{nuc}$ and the average field of other electrons $\hat{V}_{MF}(\hat{\boldsymbol{r}})$. The derivation of Dirac–Hartree–Fock equations is the same as in the nonrelativistic framework. The basis-state wave functions $|\Phi_n\rangle$ are approximated with the Slater determinant of relativistic one–particle functions, built of four–component spinors of the one–electron state

$$\phi_{n,\kappa,m}(r,\theta,\varphi) = \frac{1}{r}\begin{pmatrix} P_{n,\kappa}(r)\chi_{\kappa,m}(\theta,\varphi,\sigma) \\ iQ_{n,\kappa}(r)\chi_{-\kappa,m}(\theta,\varphi,\sigma) \end{pmatrix}, \tag{2.20}$$

where $\chi_{\kappa,m}$ is the usual spin-angular function, n is the principal quantum number, $\kappa = (l-j)(2j+1)$ is the relativistic angular quantum number, and m is the z-component of the total angular momentum j. The one-electron radial orbitals $P_{n,\kappa}(r)$ and $Q_{n,\kappa}(r)$ must satisfy the coupled Dirac equation

$$\begin{aligned} \left(\frac{d}{dr} + \frac{\kappa}{r}\right) P_{n,\kappa}(r) &= \alpha\left(\epsilon_{n\kappa} - V(r) + \frac{2}{\alpha^2}\right) Q_{n,\kappa}(r) \\ \left(\frac{d}{dr} - \frac{\kappa}{r}\right) Q_{n,\kappa}(r) &= -\alpha\Big(\epsilon_{n\kappa} - V(r)\Big) P_{n,\kappa}(r) \end{aligned} \tag{2.21}$$

where α is the fine structure constant, $\epsilon_{n\kappa}$ are the energy eigenvalues of the radial orbitals, and $V(r)$ is a local central field.

In FAC Dirac-Fock-Slater approach (with Slater form of exchange potential from

Eq. (2.7)) is used to calculate the ground state configuration and to obtain a mean-field $V(r)$. The basis function (including high Rydberg orbitals) are obtained by solving Dirac equation (Eq. (2.21)). The approximate atomic state functions are given by mixing the basis states $|\Phi_n\rangle$ with the same symmetry

$$|\Psi\rangle = \sum_a b_a |\Phi_a\rangle \tag{2.22}$$

where b_n are the mixing coefficients obtained from diagonalizing the Hamiltonian $H'_R = H_D + V_{nuc} + \sum_{i<j} 1/|\mathbf{r}_i - \mathbf{r}_j|$. The radiative transition rates are calculated in the single multipole approximation. This means that the interference between different multipoles is not taken into account, although rates corresponding to arbitrary multipoles can be calculated. For a given multipole operator $\hat{O}^L_M$, and initial and final states of the transition $|\Phi_i\rangle$ and $|\Phi_f\rangle$, the line strength of the transition is

$$S_{fi} = |\langle \Phi_f || \hat{O}^L_M || \Phi_i \rangle|^2 \tag{2.23}$$

Part I

Inner atomic dynamics using ATAS

Chapter 3

Theoretical description of ATAS

This chapter is based on the results published in Ref. [68]. Here I derive a theoretical description of ATAS for temporally and spatially overlapping XUV and optical pulses. The information is gained from the absorption spectrum of an attosecond XUV pulse, which coherently excites a system. The optical pulse dresses a system and in such a way gives a reference time that provides a possibility to measure the evolution of a system. The intensity of the optical laser field is assumed to be low enough to provide only a dressing of the system, which means that due to interaction with a laser field all states of the atom can be described in terms of a Floquet picture [82]. For the theoretical description of the processes of relevance here the semiclassical approximation is used, by treating the electronic system under study as a quantum object and using the classical Maxwell equations for the electromagnetic field. In view of the rather small pulse intensities of currently available attosecond sources, perturbation theory may be considered as an excellent framework for treating the effect of the attosecond pulse.

The theoretical description of ATAS allows one to study intra-atomic dynamics in detail and draw conclusions from the resulting ATAS spectrum.

3.1 Perturbative treatment of XUV probe pulse

I perform analysis of the transient absorption signal as a function of the time delay between the attosecond excitation pulse and the femtosecond pulse, treating the XUV pulse perturbatively. I employ the electric-dipole approximation and assume that the XUV and optical pulses are both linearly polarized along the z-axis. Following the logic presented in Ref. [60], I start by solving the time-dependent

Schrödinger equation:

$$i\frac{\partial}{\partial t}|\Psi,t\rangle = \hat{H}(t)|\Psi,t\rangle, \tag{3.1}$$

$$\hat{H}(t) = \hat{H}_0 - E_0 - \varepsilon_d(t)\hat{Z} - \varepsilon_{\text{xuv}}(t)\hat{Z}, \tag{3.2}$$

where $\hat{H}_0$ is the unperturbed Hamiltonian of the electronic system, E_0 is its ground-state energy, $\hat{Z}$ is the component of the electric dipole operator along the polarization direction of the electromagnetic field, and $\varepsilon_d(t)$ and $\varepsilon_{\text{xuv}}(t)$ are the amplitude of the dressing (NIR) and attosecond (XUV) electric fields, respectively. Assuming the effect of the attosecond XUV pulse can be treated perturbatively, the solution of Eq. (3.1) is:

$$|\Psi,t\rangle = |\Psi_d,t\rangle + |\Psi_d,t\rangle^{(1)} + ..., \tag{3.3}$$

where $|\Psi_d,t\rangle$ is the optically-dressed electronic state vector in the absence of the attosecond pulse and $|\Psi_d,t\rangle^{(1)}$ is the first-order correction with respect to the attosecond pulse, evolving in the optical dressing field $\varepsilon_d(t)$. I employ the time-evolution operator $\hat{U}_d(t,\tau)$ to determine the optically-dressed state vector

$$|\Psi_d,t\rangle = \hat{U}_d(t,\tau)|\Psi_0\rangle. \tag{3.4}$$

Here τ is a time before the system is optically dressed and $|\Psi_0\rangle$ is the initial state. The dipole moment of the electronic system along the z-axis can be expressed as:

$$D(t) = \langle\Psi,t|\hat{Z}|\Psi,t\rangle = D_d(t) + D^{(1)}(t) + ... \tag{3.5}$$

The term $D_d(t)$ describes harmonic generation driven by the dressing pulse only, and $D^{(1)}(t)$ is the dipole moment correction to first order with respect to $\varepsilon_{\text{xuv}}(t)$,

$$D_d(t) = \langle\Psi_d,t|\hat{Z}|\Psi_d,t\rangle, \tag{3.6}$$

$$D^{(1)}(t) = i\int_{-\infty}^{t} dt'\varepsilon_{\text{xuv}}(t')\langle\Psi_d,t|\hat{Z}\hat{U}_d(t,t')\hat{Z}|\Psi_d,t'\rangle + c.c. \tag{3.7}$$

3.2 Wave-packet time-propagation method

Assuming that the attosecond pulse is shorter than all relevant electronic time scales [60], I approximate it by a delta function $\varepsilon_{\text{xuv}}(t) = A_{\text{xuv}}\delta(t - t_0)$, where t_0 is the moment when the attosecond pulse interacts with the system. Hence,

$$D^{(1)}(t) = \begin{cases} 0, & t < t_0, \\ iA_{\text{xuv}}\langle\Psi_d, t|\hat{Z}\hat{U}_d(t, t_0)\hat{Z}|\Psi_d, t_0\rangle + c.c., & t \geq t_0. \end{cases} \tag{3.8}$$

It is assumed throughout that the dressing field $\varepsilon_d(t)$ is not strong enough to excite the ground state of the system. Therefore, $\langle\Psi_d, t| \approx \langle\Psi_0|$ and $|\Psi_d, t_0\rangle \approx |\Psi_0\rangle$. As a consequence,

$$D^{(1)}(t) = \begin{cases} 0, & t < t_0, \\ iA_{\text{xuv}}\langle\tilde{\Psi}, t_0|\hat{U}_d(t, t_0)|\tilde{\Psi}, t_0\rangle + c.c., & t \geq t_0, \end{cases} \tag{3.9}$$

where

$$|\tilde{\Psi}, t_0\rangle = \hat{Z}|\Psi_0\rangle \tag{3.10}$$

is the initial state of the electronic wave packet right after excitation by the XUV pulse at $t = t_0$. Thus, introducing the autocorrelation function

$$C(t, t_0) = \langle\tilde{\Psi}, t_0|\tilde{\Psi}, t\rangle, \tag{3.11}$$

where

$$|\tilde{\Psi}, t\rangle = \hat{U}_d(t, t_0)|\tilde{\Psi}, t_0\rangle \tag{3.12}$$

reflects the time evolution of the XUV-excited system in the dressing field, the dipole moment is given by

$$D^{(1)}(t) = \begin{cases} 0, & t < t_0, \\ iA_{\text{xuv}}C(t, t_0) + c.c., & t \geq t_0. \end{cases} \tag{3.13}$$

Autocorrelation function $C(t, t_0)$ is computed by employing the following numerical strategy. Unitary wave-packet propagation (in the absence of Auger decay) is ensured by approximating the relevant time-evolution operator for a time step from

t to $t + \Delta t$ through

$$\hat{U}_d(t + \Delta t, t) \approx e^{-i\hat{H}_d(t+\frac{\Delta t}{2})\Delta t}, \tag{3.14}$$

which has an error that, to leading order, scales as Δt^3. Note that the Hamiltonian in Eq. (3.14),

$$\hat{H}_d(t) = \hat{H}_0 - E_0 - \varepsilon_d(t)\hat{Z}, \tag{3.15}$$

does not include the XUV field.

To perform a numerical solution a finite set of inner-shell-excited eigenstates $\{|\Psi_I\rangle\}$ is calculated and the corresponding inner-shell-excited wave packet is expanded in this subspace

$$|\tilde{\Psi}, t\rangle = \sum_I a_I(t)|\Psi_I\rangle. \tag{3.16}$$

Upon combining Eqs. (3.14) and (3.16) an expression for the propagation of the vector of expansion coefficients is obtained

$$\boldsymbol{a}(t + \Delta t) = e^{-i\boldsymbol{H}_d(t+\frac{\Delta t}{2})\Delta t}\boldsymbol{a}(t), \tag{3.17}$$

where $(\boldsymbol{a})_I = a_I$ and $(\boldsymbol{H}_d)_{IJ} = \langle\Psi_I|\hat{H}_d|\Psi_J\rangle$, and I,J are indices that run from 1 to N where N is the size of the finite set. Taking into account the initial condition

$$a_I(t_0) = \langle\Psi_I|\tilde{\Psi}, t_0\rangle = \langle\Psi_I|\hat{Z}|\Psi_0\rangle. \tag{3.18}$$

Eq. (3.17) is solved. The diagonalization of the instantaneous Hamiltonian matrix in each time step provides the eigenvalues $\tilde{E}_k$ and eigenvectors $\boldsymbol{v}_k$ of the operator $\mathbf{H}_d$ in efficient way. Hence,

$$\boldsymbol{a}(t + \Delta t) = \sum_k e^{-i\tilde{E}_k(t+\frac{\Delta t}{2})\Delta t}\boldsymbol{v}_k(t + \Delta t)\boldsymbol{v}_k^\dagger(t + \Delta t)\boldsymbol{a}(t). \tag{3.19}$$

Via

$$C(t, t_0) = \sum_I a_I^*(t_0)a_I(t) \tag{3.20}$$

I obtain the autocorrelation function required for the evaluation of Eq. (3.13).

Once the XUV-induced dipole moment in the presence of laser dressing is available, the XUV cross section can be calculated

$$\sigma^{(1)}(\omega) = \frac{4\pi\omega}{c}\mathrm{Im}\Big[\frac{\tilde{D}^{(1)}(\omega)}{\tilde{\varepsilon}_x(\omega)}\Big], \tag{3.21}$$

where $\tilde{D}^{(1)}(\omega)$ and $\tilde{\varepsilon}_x(\omega)$ are the Fourier transforms of $D^{(1)}(t)$ and $\varepsilon_x(t)$, respectively. Computed with Eq. (3.21) XUV cross sections for the dressed Xe atom are presented and discussed in Chapter 5 on the example of Xe.

3.3 Perturbative treatment of the dressing pulse

For the case of a weak NIR pulse perturbation theory can be used for both XUV and optical pulses. A perturbative analysis of the transient absorption signal as a function of the time delay between the attosecond excitation pulse and the femtosecond dressing pulse is performed. Treating the dressing field perturbatively allows for an elementary explanation of the signals one can obtain in ATA experiments.

To perform a perturbative analysis I separate the t dependence in $\langle\Psi_d, t|\hat{Z}\hat{U}_d(t,t')\hat{Z}|\Psi_d, t'\rangle$ from the t' dependence in Eq. (3.7). To this end the following identity is employed

$$\hat{U}_d(t,t') = \hat{U}_d(t,t_0)\hat{U}_d^{\dagger}(t',t_0), \tag{3.22}$$

which is correct for any reference time t_0. Employing Eqs. (3.7) and (3.22), the dipole moment correction along the z-axis can be written as

$$\begin{aligned} D^{(1)}(t) &= i\sum_f \Big[\int_{-\infty}^{t} dt' \varepsilon_{\mathrm{xuv}}(t') F_{0f}(t) F_{f0}(t') - \int_{-\infty}^{t} dt' \varepsilon_{\mathrm{xuv}}(t') F_{0f}^*(t) F_{f0}^*(t')\Big] \\ &= iA_{\mathrm{xuv}} \sum_f \big[F_{0f}(t)F_{f0}(\tau) - F_{0f}^*(t)F_{f0}^*(\tau)\big]\,\theta(t-\tau), \end{aligned} \tag{3.23}$$

where $\theta(t-\tau)$ is the Heaviside function. The functions $F_{mn}(t)$ in Eq. (3.23) represent transition dipole matrix elements between optically dressed states $|\Psi_m\rangle$ and $|\Psi_n\rangle$,

$$F_{mn}(t) = \langle\Psi_m|\hat{U}_d^{\dagger}(t,t_0)\hat{Z}\hat{U}_d(t,t_0)|\Psi_n\rangle. \tag{3.24}$$

Using Eq. (3.23) and taking into account that the dipole moment $D^{(1)}(t)$ is a real function, I obtain from Eq. (3.21)

$$\begin{aligned}\sigma^{(1)}(\omega,\tau) &= i\frac{4\pi\omega}{c}\sum_f \int_{-\infty}^{\infty} dt\left[F_{0f}(t)F_{f0}(\tau) - F_{0f}^*(t)F_{f0}^*(\tau)\right]\theta(t-\tau)\mathrm{Im}\left[e^{i\omega(t-\tau)}\right] \\ &= \frac{2\pi\omega}{c}\sum_f \int_{\tau}^{\infty} dt\left[F_{0f}(t)e^{i\omega t}F_{f0}(\tau)e^{-i\omega\tau} - F_{0f}(t)e^{-i\omega t}F_{f0}(\tau)e^{i\omega\tau} + c.c.\right].\end{aligned} \tag{3.25}$$

In order to explore the spectroscopic properties of the atomic cross-section function $\sigma^{(1)}(\omega,\tau)$ I perform a perturbative analysis of the impact of the dressing field on a system. Applying perturbation theory, the time-evolution operator $\hat{U}_d(t,t_0)$ in the presence of the dressing field [see Eq. (3.4)] can be written as follows:

$$\begin{aligned}\hat{U}_d(t,t_0) &= e^{-i(\hat{H}_0-E_0)(t-t_0)}\left[1 - i\int_{t_0}^{t} dt'\hat{V}_d(t')\hat{U}_d^I(t',t_0)\right] \\ &= e^{-i(\hat{H}_0-E_0)(t-t_0)}\left[1 - i\int_{t_0}^{t} dt'\hat{V}_d(t') - \int_{t_0}^{t} dt'\int_{t_0}^{t'} dt''\hat{V}_d(t')\hat{V}_d(t'') + ...\right],\end{aligned} \tag{3.26}$$

where

$$\hat{U}_d^I(t,t_0) = 1 - i\int_{t_0}^{t} dt'\hat{V}_d(t')\hat{U}_d^I(t',t_0) \tag{3.27}$$

is the time-evolution operator in the interaction picture and

$$\hat{V}_d(t) = -\varepsilon_d(t)e^{i\{\hat{H}_0-E_0\}(t-t_0)}\hat{Z}e^{-i\{\hat{H}_0-E_0\}(t-t_0)} \tag{3.28}$$

is the perturbation by the optical dressing field.

When evaluating Eq. (3.23), I make use of a complete set of eigenstates of $\hat{H}_0$. Because the excited states accessed may lie in the electronic continuum, this involves, strictly speaking, an integration over states. However, by focusing on bound states

and autoionizing states only, I replace the integration by a summation over a discrete set of states $|\Psi_f\rangle$ with a complex energy

$$\hat{H}_0|\Psi_f\rangle = (E_f - i\frac{\Gamma_f}{2})|\Psi_f\rangle. \tag{3.29}$$

Here E_f is the real part of the energy and the non-negative real number Γ_f is the decay rate of the state $|\Psi_f\rangle$ ($\Gamma_f = 0$ for bound states). As a consequence of this choice, $\hat{H}_0$ is not Hermitian, and, therefore, the time-evolution operator $\hat{U}_d$ is not unitary, i.e. $\hat{U}_d^{-1}(t,t_0) \neq \hat{U}_d^{\dagger}(t,t_0)$. This is important, because in the analytical treatment that follows, the inverse of $\hat{U}_d(t,t_0)$ is required

$$\begin{aligned}\hat{U}_d^{-1}(t,t_0) &= \Big[1 + i\int_{t_0}^{t} dt'(\hat{U}_d^I(t',t_0))^{-1}\hat{V}_d(t')\Big]e^{i(\hat{H}_0-E_0)(t-t_0)} \\ &= \Big[1 + i\int_{t_0}^{t} dt'\hat{V}_d(t') - \int_{t_0}^{t} dt'\int_{t_0}^{t'} dt''\hat{V}_d(t'')\hat{V}_d(t') + ...\Big]e^{i(\hat{H}_0-E_0)(t-t_0)},\end{aligned} \tag{3.30}$$

which differs from $\hat{U}_d^{\dagger}(t,t_0)$ as conjugation is not applied to the Hamiltonian $\hat{H}_0$.

I now apply Eqs. (3.26) and (3.30) to Eq. (3.24). Resonant excitation involving XUV light tends to lead to the formation of an inner-shell hole accompanied by an excited electron (for atoms heavier than helium). For a given inner-shell hole, the decay rate is relatively insensitive to the state of the excited electron. Thus, I assume the decay rates to be equal to each other for all states ($\Gamma_n = \Gamma_f$), except for the ground state ($\Gamma_0 = 0$). As a consequence, through second order in the dressing field, F_{f0} can be

decomposed as follows:

$$\begin{aligned} F_{f0}(t) =& F_{f0}^{00}(t) + F_{f0}^{01}(t) + F_{f0}^{10}(t) + F_{f0}^{02}(t) + F_{f0}^{20}(t) + F_{f0}^{11}(t) + ... \\ =& \; f_{f0}^{00}(t) e^{\frac{\Gamma_f}{2}t} \langle \Psi_f | \hat{Z} | \Psi_0 \rangle \\ &+ \sum_a f_{fa0}^{01}(t) e^{\frac{\Gamma_f}{2}t} \langle \Psi_f | \hat{Z} | \Psi_a \rangle \langle \Psi_a | \hat{Z} | \Psi_0 \rangle \\ &+ \sum_\alpha f_{f\alpha 0}^{10}(t) e^{\frac{\Gamma_f}{2}t} \langle \Psi_f | \hat{Z} | \Psi_\alpha \rangle \langle \Psi_\alpha | \hat{Z} | \Psi_0 \rangle \\ &+ \sum_{ab} f_{fba0}^{02}(t) e^{\frac{\Gamma_f}{2}t} \langle \Psi_f | \hat{Z} | \Psi_b \rangle \langle \Psi_b | \hat{Z} | \Psi_a \rangle \langle \Psi_a | \hat{Z} | \Psi_0 \rangle \\ &+ \sum_{\alpha\beta} f_{f\alpha\beta 0}^{20}(t) e^{\frac{\Gamma_f}{2}t} \langle \Psi_f | \hat{Z} | \Psi_\alpha \rangle \langle \Psi_\alpha | \hat{Z} | \Psi_\beta \rangle \langle \Psi_\beta | \hat{Z} | \Psi_0 \rangle \\ &+ \sum_{a\alpha} f_{f\alpha a 0}^{11}(t) e^{\frac{\Gamma_f}{2}t} \langle \Psi_f | \hat{Z} | \Psi_\alpha \rangle \langle \Psi_\alpha | \hat{Z} | \Psi_a \rangle \langle \Psi_a | \hat{Z} | \Psi_0 \rangle + ... \end{aligned} \tag{3.31}$$

The functions f_{fxy0}^{mn} are $[n+m]$-th order integrals for transitions from the initial $|\Psi_0\rangle$ to the final state $|\Psi_f\rangle$ through the states $|\Psi_x\rangle$, $|\Psi_y\rangle$ (see Table 3.1). I use letters a and b for states associated with the perturbation of the initial state by the dressing field and the letters α and β for the dressing of the final state. The expression for $F_{0f}(t)$ differs from that for $F_{f0}^*(t)$ solely by the sign of the exponents proportional to Γ_f.

3.4 Analytical structure of the cross section

3.4.1 Atomic cross section in a time-delay domain

Assuming that initial-state dressing is negligible, all the terms involving indices a and b in Eq. (3.31) can be set to zero, thus perturbative expansion of $F_{0f}(t)$ can be simplified to the following expression:

$$\begin{aligned} F_{0f}(t) =& \; \left[f_{f0}^{00}(t) \right]^* e^{-\frac{\Gamma_f}{2}t} \langle \Psi_0 | \hat{Z} | \Psi_f \rangle \\ &+ \sum_x \left[f_{fx0}^{10}(t) \right]^* e^{-\frac{\Gamma_f}{2}t} \langle \Psi_0 | \hat{Z} | \Psi_x \rangle \langle \Psi_x | \hat{Z} | \Psi_f \rangle \\ &+ \sum_{xy} \left[f_{fxy0}^{20}(t) \right]^* e^{-\frac{\Gamma_f}{2}t} \langle \Psi_0 | \hat{Z} | \Psi_y \rangle \langle \Psi_y | \hat{Z} | \Psi_x \rangle \langle \Psi_x | \hat{Z} | \Psi_f \rangle + ... \end{aligned} \tag{3.32}$$

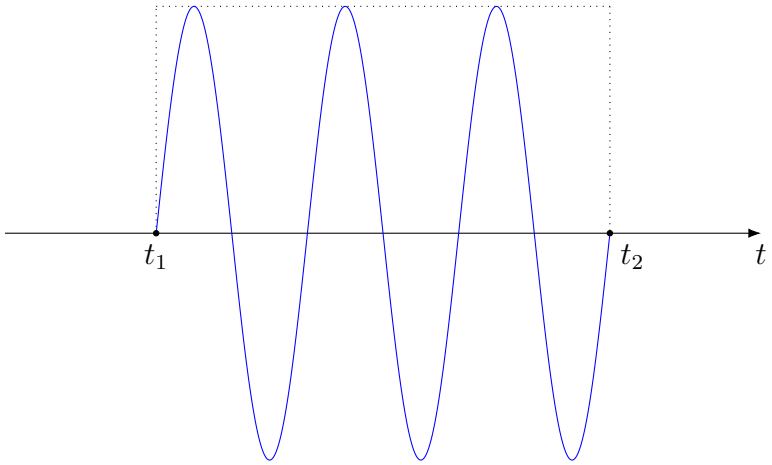

FIGURE 3.1: Rectangular-shaped dressing pulse that starts at time $t_1 = 0$ and ends at t_2. Duration of the pulse is cosen to be an integer multiple of the period $2\pi/\omega_d$.

In the following, I assume that the optical dressing pulse has a rectangular shape:

$$\varepsilon_d(t) = A_d\Big(\theta(t-t_1) - \theta(t-t_2)\Big)\sin(\omega_d t), \tag{3.33}$$

as shown in Figure 3.1. In Eq. (3.33), ω_d is the photon energy of the dressing field and A_d is the field amplitude. The dressing pulse is assumed to start at $t_1 = 0$. Thus, the time τ associated with the attosecond XUV pulse is the delay of the attosecond XUV pulse relative to the beginning of the optical dressing pulse.

Functions $f^{mn}_{fxy0}(t)$ introduced in Eq. (3.32) are given in Table 3.1 for the dressing pulse in Eq. (3.33).

Here, I made the choice $t_0 \to -\infty$ when evaluating Eq. (3.24) using Eqs. (3.26) and (3.30). The energy differences $\Delta^{(n)}_{x\pm}$ appearing in Table 3.1 are

$$\Delta^{(0)}_{x} = E_x - E_0; \tag{3.34}$$
$$\Delta^{(1)}_{x\pm} = E_x - E_0 \pm \omega_d; \tag{3.35}$$
$$\Delta^{(2)}_{x\pm} = E_x - E_0 \pm 2\omega_d. \tag{3.36}$$

TABLE 3.1: Functions $f^{mn}_{fxy0}(t)$

Function	**Condition**	**Expression**
$\boldsymbol{f^{00}_{f0}(t)}$	$-\infty < t < \infty$	$e^{i\Delta^{(0)}_f t}$
$\boldsymbol{f^{10}_{fx0}(t)}$	$-\infty < t < t_1$	0
	$t_1 < t < t_2$	$B^{fx}_1 e^{i\Delta^{(1)}_{f+}t} - B^{fx}_2 e^{i\Delta^{(1)}_{f-}t} - A^{fx}(t_1)e^{i\Delta^{(0)}_x t}$
	$t_2 < t < \infty$	$\Big[A^{fx}(t_2) - A^{fx}(t_1)\Big]e^{i\Delta^{(0)}_x t}$
$\boldsymbol{f^{20}_{fxy0}(t)}$	$-\infty < t < t_1$	0
	$t_1 < t < t_2$	$D^{fxy}_1 e^{i\Delta^{(2)}_{f+}t} - D^{fxy}_2 e^{i\Delta^{(0)}_f t} + D^{fxy}_3 e^{i\Delta^{(2)}_{f-}t}$ $-D^{fxy}_4 e^{i\Delta^{(1)}_{x+}t} + D^{fxy}_5 e^{i\Delta^{(1)}_{x-}t} - C^{fxy}(t_1)e^{i\Delta^{(0)}_y t}$
	$t_2 < t < \infty$	$\Big[C^{fxy}(t_2) - C^{fxy}(t_1)\Big]e^{i\Delta^{(0)}_y t}$

The other quantities used in Table 3.1 are listed in the following:

$$B^{fx}_1 = \frac{A_d}{2}\frac{1}{i(E_f - E_x + \omega_d)}; \tag{3.37}$$

$$B^{fx}_2 = \frac{A_d}{2}\frac{1}{i(E_f - E_x - \omega_d)}; \tag{3.38}$$

$$A^{fx}(t) = \frac{A_d}{2} f_1(E_f - E_x, \omega_d, t), \tag{3.39}$$

where

$$f_1(\Delta, \omega, t) = \frac{\mathrm{e}^{i(\Delta+\omega)t}}{i(\Delta+\omega)} - \frac{\mathrm{e}^{i(\Delta-\omega)t}}{i(\Delta-\omega)}; \tag{3.40}$$

$$D^{fxy}_1 = -\frac{A^2_d}{4}\frac{1}{(E_f - E_x + \omega_d)(E_f - E_y + 2\omega_d)}; \tag{3.41}$$

$$D^{fxy}_2 = -\frac{A^2_d}{4}\left(\frac{1}{(E_f - E_x + \omega_d)(E_f - E_y)} + \frac{1}{(E_f - E_x - \omega_d)(E_f - E_y)}\right); \tag{3.42}$$

$$D^{fxy}_3 = -\frac{A^2_d}{4}\frac{1}{(E_f - E_x - \omega_d)(E_f - E_y - 2\omega_d)}; \tag{3.43}$$

$$D_4^{fxy} = \frac{A_d^2}{4}\frac{f_1(E_f - E_x, \omega_d, t_1)}{i(E_x - E_y + \omega_d)}; \tag{3.44}$$

$$D_5^{fxy} = \frac{A_d^2}{4}\frac{f_1(E_f - E_x, \omega_d, t_1)}{i(E_x - E_y - \omega_d)}; \tag{3.45}$$

$$\begin{aligned} C^{fxy}(t) =& D_1^{fxy} e^{i(E_f - E_y + 2\omega_d)t} - D_2^{fxy} e^{i(E_f - E_y)t} + D_3^{fxy} e^{i(E_f - E_y - 2\omega_d)t} \\ & - \frac{A_d^2}{4} f_1(E_f - E_x, \omega_d, t_1) f_1(E_x - E_y, \omega_d, t). \end{aligned} \tag{3.46}$$

XUV one-photon cross section from Eq. (3.25) can be written as:

$$\sigma^{(1)}(\omega, \tau) = \frac{2\pi\omega}{c} \sum_f \left(\tilde{F}_{0f}(\omega, \tau) F_{f0}(\tau) e^{-i\omega\tau} - \tilde{F}_{0f}(-\omega, \tau) F_{f0}(\tau) e^{i\omega\tau} + c.c. \right), \tag{3.47}$$

where

$$\tilde{F}_{0f}(\omega, \tau) = \int_{-\infty}^{\infty} dt\ F_{0f}(t)\theta(t - \tau) e^{i\omega t} \tag{3.48}$$

is the Fourier transform of the function $F_{0f}(t)\theta(t - \tau)$. In order to construct the XUV one-photon cross section [Eq. (3.47)], I further require $\tilde{F}_{0f}(\omega, \tau)$. The function $\tilde{F}_{0f}(\omega, \tau)$ has the same structure as Eq. (3.32), but with the functions $\left[\ f_{fxy0}^{mn}(t)\right]^* e^{-\frac{\Gamma_f}{2}t}$ replaced with

$$\tilde{f}_{0yxf}^{nm}(\omega, \tau) = \int_{\tau}^{\infty} dt \left[\ f_{fxy0}^{mn}(t)\right]^* e^{-\frac{\Gamma_f}{2}t} e^{i\omega t}. \tag{3.49}$$

Explicit form of functions $\tilde{f}_{fxy0}^{mn}(t)$ is listed in Table 3.2 below.

The functions $f_2(\Delta, \omega)\Big|_{t_a}^{t_b}$ appearing in Table 3.2 are

$$f_2(\Delta, \omega)\Big|_{t_a}^{t_b} = f_0(\Delta + \omega, t_b) - f_0(\Delta + \omega, t_a), \tag{3.50}$$

$$f_0(\Delta, t) = \frac{e^{i\Delta t}}{i\Delta}. \tag{3.51}$$

In view of Eq. (3.47), the analytical structure of $\tilde{F}_{0f}(\omega, \tau)$ determines the resonance

TABLE 3.2: Functions $\tilde{f}^{mn}_{fxy0}(t)$

Function	Condition	Expression
$\tilde{f}^{00}_{f0}(\omega,\tau)$	$-\infty < \tau < \infty$	$f_0(\Delta_f^{(0)},\omega)\Big\vert_\tau^\infty$
$\tilde{f}^{10}_{fx0}(\omega,\tau)$	$-\infty < \tau < t_1$	0
	$t_1 < \tau < t_2$	$B_1^{fx} f_2(\Delta_{f+}^{(1)},\omega)\Big\vert_\tau^{t_2} - B_2^{fx} f_2(\Delta_{f-}^{(1)},\omega)\Big\vert_\tau^{t_2} - A^{fx}(t_1) f_2(\Delta_x^{(0)},\omega)\Big\vert_\tau^{t_2}$
	$t_2 < \tau < \infty$	$\left[A^{fx}(t_2) - A^{fx}(t_1)\right] f_2(\Delta_x^{(0)},\omega)\Big\vert_{t_2}^\infty$
$\tilde{f}^{20}_{fxy0}(\omega,\tau)$	$-\infty < \tau < t_1$	0
	$t_1 < \tau < t_2$	$D_1^{fxy} f_2(\Delta_{f+}^{(2)},\omega)\Big\vert_\tau^{t_2} - D_2^{fxy} f_2(\Delta_f^{(0)},\omega)\Big\vert_\tau^{t_2} + D_3^{fxy} f_2(\Delta_{f-}^{(2)},\omega)\Big\vert_\tau^{t_2} -$ $-D_4^{fxy} f_2(\Delta_{x+}^{(1)},\omega)\Big\vert_\tau^{t_2} + D_5^{fxy} f_2(\Delta_{x-}^{(1)},\omega)\Big\vert_\tau^{t_2} - C^{fxy}(t_1) f_2(\Delta_y^{(0)},\omega)\Big\vert_\tau^{t_2}$
	$t_2 < \tau < \infty$	$\left[C^{fxy}(t_2) - C^{fxy}(t_1)\right] f_2(\Delta_y^{(0)},\omega)\Big\vert_\tau^\infty$

peaks in the XUV one-photon cross section as a function of ω. In general $\tilde{F}_{0f}(\omega,\tau)$ has the form

$$\tilde{F}_{0f}(\omega,\tau) = \sum_k C_k \frac{e^{-i(\Delta_k - i\frac{\Gamma_f}{2} - \omega)\tau}}{i(\Delta_k - i\frac{\Gamma_f}{2} - \omega)}, \tag{3.52}$$

where each Δ_k is one of the quantities presented in Eqs. (3.34)-(3.36). Thus, the Δ_k define the poles of $\tilde{F}_{0f}(\omega,\tau)$ in the complex ω plane. The peaks of $\sigma^{(1)}(\omega,\tau)$ at the Δ_k correspond to XUV transitions accompanied by the absorption or emission of zero [Eq. (3.34)], one [Eq. (3.35)], or two [Eqs. (3.36)] dressing laser photons, or one absorption and one emission Eq. (3.34).

In such a way, the presence of a dressing field allows for an excitation of the light-induced states (LIS) [83, 84, 85]. The XUV absorption spectrum contains all absorption lines corresponding to states that can be excited according to the dipole selection rules: bright states [Eq. (3.34)] and LIS [Eq. (3.35)]. The magnitude of the corresponding peak is determined by the coefficient C_k. This coefficient in Eq. (3.52) depends on whether the attosecond pulse precedes the dressing pulse ($-\infty < \tau < t_1$), whether the attosecond pulse overlaps with the dressing pulse ($t_1 < \tau < t_2$), or whether the attosecond pulse arrives after the dressing pulse is over ($t_2 < \tau < \infty$), but remains constant and does not change with τ inside these regions. Thus, from

Eq. (3.47) it follows, that positions of atomic absorption peaks are determined by the $\tilde{F}_{0f}(\omega,\tau)$ function and are located at the photon energy $\omega = \Delta_k$, and their oscillation with the time delay τ is described by the product of the function $F_{f0}(\tau)$ and the exponential numerator of function $\tilde{F}_{0f}(\omega,\tau)$.

3.4.2 Atomic cross section in a Fourier-energy domain

In order to identify the associated oscillation frequencies, I take the Fourier transform of $\sigma^{(1)}(\omega,\tau)$ with respect to the delay τ between the attosecond XUV pulse and the optical dressing pulse:

$$\tilde{\sigma}^{(1)}(\omega,\omega') = \int_{-\infty}^{\infty} d\tau\, \sigma^{(1)}(\omega,\tau) e^{i\omega'\tau}. \tag{3.53}$$

From Eq. (3.47) one can see that the cross-section function $\tilde{\sigma}^{(1)}(\omega,\omega')$ in a Fourier-energy domain can be written as

$$\tilde{\sigma}^{(1)}(\omega,\omega') = \frac{2\pi\omega}{c} \sum_f \Big(\tilde{\mathcal{F}}_f(\omega,\omega') - \tilde{\mathcal{F}}_f(-\omega,\omega') + \tilde{\mathcal{F}}_f^*(\omega,-\omega') - \tilde{\mathcal{F}}_f^*(-\omega,-\omega') \Big), \tag{3.54}$$

where

$$\tilde{\mathcal{F}}_f(\omega,\omega') = \int_{-\infty}^{\infty} d\tau \tilde{F}_{0f}(\omega,\tau) F_{f0}(\tau) e^{i(\omega'-\omega)\tau}. \tag{3.55}$$

To get the analytical structure of $\tilde{\mathcal{F}}_f(\omega,\omega')$ function it is useful to view it as a sum of $\tilde{\mathcal{F}}_f^{xy}(\omega,\omega')$ functions as

$$\begin{aligned} \tilde{\mathcal{F}}_f(\omega,\omega') = \sum_{xy} \Big(& \tilde{\mathcal{F}}_f^{xy}(\omega,\omega')\Big|_{\tau<t_1} + \tilde{\mathcal{F}}_f^{xy}(\omega,\omega')\Big|_{t_1<\tau<t_2} + \tilde{\mathcal{F}}_f^{xy}(\omega,\omega')\Big|_{t_2<\tau} \Big) \\ & \times \langle\Psi_0|\hat{Z}|\Psi_f\rangle\langle\Psi_f|\hat{Z}|\Psi_x\rangle\langle\Psi_x|\hat{Z}|\Psi_y\rangle\langle\Psi_y|\hat{Z}|\Psi_0\rangle. \end{aligned} \tag{3.56}$$

In Eq. (3.56) I separate $\tilde{\mathcal{F}}_f^{xy}(\omega,\omega')$ functions with respect to excitation time τ, whether it precedes the dressing pulse, overlaps with it, or happens after the dressing pulse is over. Here the indexes x and y are used for the dark and bright intermediate states correspondingly, which can serve as an intermediate state for the electron

while getting excited from the ground state $|\Psi_0\rangle$ to the final state $|\Psi_f\rangle$. Due to our assumption that the dressing pulse can not affect the ground state $|\Psi_0\rangle$, the function

$$\tilde{\mathcal{F}}_f^{xy}(\omega,\omega')\Big|_{t_2<\tau} = 0. \tag{3.57}$$

It means, that if the excitation takes place when the dressing field is over, the amount of XUV light, transmitted through the sample will remain constant, because there will be no dynamics driven by the dressing field and thus no oscillations in a cross-section function. For the $\tau < t_1$ scenario, when the XUV excitation precedes the dressing pulse, $\tilde{\mathcal{F}}_f^{xy}(\omega,\omega')$ reads

$$\begin{aligned}\tilde{\mathcal{F}}_f^{xy}(\omega,\omega')\Big|_{\tau<t_1} = &\left[f_{fxy0}^{20}(-\omega,t_1)\Big|_{\tau<t_1} + f_{fxy0}^{20}(-\omega,t_1)\Big|_{t_1<\tau<t_2} + f_{fxy0}^{20}(-\omega,t_1)\Big|_{t_2<\tau} \right]^* \\ &\times f_0(\Delta_f^{(0)} - \omega + \omega_1, t_1).\end{aligned} \tag{3.58}$$

for the case, when the XUV overlaps with the dessing pulse

$$\tilde{\mathcal{F}}_f^{xy}(\omega,\omega')\Big|_{t_1<\tau<t_2} = \frac{1}{i(\Delta_f^{(0)}-\omega)}\tilde{f}^{20}_{fxy0}(\omega'-\Delta_f^{(0)},t_1)$$

$$+$$

$$\left[B_1^{yx} f_0(\Delta_{x+}^{(1)}-\omega,t_2) - B_2^{yx} f_0(\Delta_{x-}^{(1)}-\omega,t_2) - A^{yx}(t_1) f_0(\Delta_y^{(0)}-\omega,t_2)\right]^* \tilde{f}^{10}_{xf0}(\omega'-\omega,t_1) -$$

$$\left[\frac{B_1^{yx}}{i(\Delta_{x+}^{(1)}-\omega)}\right]^* \tilde{f}^{10}_{xf0}(\omega'-\Delta_{x+}^{(1)},t_1) - \left[\frac{B_2^{yx}}{i(\Delta_{x-}^{(1)}-\omega)}\right]^* \tilde{f}^{10}_{xf0}(\omega'-\Delta_{x-}^{(1)},t_1) -$$

$$\left[\frac{A^{yx}(t_1)}{i(\Delta_y^{(0)}-\omega)}\right]^* \tilde{f}^{10}_{xf0}(\omega'-\Delta_y^{(0)},t_1) - \left[\Big(A^{yx}(t_2)-A^{yx}(t_1)\Big) f_0(\Delta_y^{(0)}-\omega,t_2)\right]^* \tilde{f}^{10}_{xf0}(\omega'-\omega,t_1)$$

$$+$$

$$\Bigg[D_1^{yxf} f_0(\Delta_{f+}^{(2)}-\omega,t_2) - D_2^{yxf} f_0(\Delta_f^{(0)}-\omega,t_2) + D_3^{yxf} f_0(\Delta_{f-}^{(2)}-\omega,t_2) - D_4^{yxf} f_0(\Delta_{x+}^{(1)}-\omega,t_2) +$$

$$D_5^{yxf} f_0(\Delta_{x-}^{(1)}-\omega,t_2) - C^{yxf}(t_1) f_0(\Delta_y^{(0)}-\omega,t_2)\Bigg]^* f_2(\Delta_f^{(0)}-\omega,\omega_1)\Big|_{t_1}^{t_2} -$$

$$\Bigg[\frac{D_1^{yxf} f_2(-2\omega_{IR},\omega_1)\Big|_{t_1}^{t_2}}{i(\Delta_{f+}^{(2)}-\omega)} - \frac{D_2^{yxf} f_2(0,\omega_1)\Big|_{t_1}^{t_2}}{i(\Delta_f^{(0)}-\omega)} + \frac{D_3^{yxf} f_2(2\omega_{IR},\omega_1)\Big|_{t_1}^{t_2}}{i(\Delta_{f-}^{(2)}-\omega)} - \frac{D_4^{yxf} f_2(\Delta_f^{(0)}-\Delta_{x+}^{(1)},\omega_1)\Big|_{t_1}^{t_2}}{i(\Delta_{x+}^{(1)}-\omega)} +$$

$$\frac{D_5^{yxf} f_2(\Delta_f^{(0)}-\Delta_{x-}^{(1)},\omega_1)\Big|_{t_1}^{t_2}}{i(\Delta_{x-}^{(1)}-\omega)} - \frac{C^{yxf}(t_1) f_2(\Delta_f^{(0)}-\Delta_y^{(0)},\omega_1)\Big|_{t_1}^{t_2}}{i(\Delta_y^{(0)}-\omega)}\Bigg]^* f_2(\Delta_f^{(0)}-\omega,\omega_1)\Big|_{t_1}^{t_2}$$

$$+$$

$$\left[\Big(C^{yxf}(t_2)-C^{yxf}(t_1)\Big) f_2(\Delta_y^{(0)},-\omega)\Big|_{t_2}^{\infty})\right]^* f_2(\Delta_f^{(0)}-\omega,\omega_1)\Big|_{t_1}^{t_2}.$$

(3.59)

By making use of the analytical results presented in Equations (3.58) and (3.59), one can see that the function $\tilde{\mathcal{F}}_f(\omega,\omega')$ has the following structure:

$$\tilde{\mathcal{F}}_f(\omega,\omega') = \sum_{kj} \frac{A_{kj}(\omega,\omega')}{i(\Delta_k - \Delta_j + \omega')}, \tag{3.60}$$

where the functions $A_{kj}(\omega,\omega')$ have no poles as a function of ω'. The XUV one-photon cross section $\tilde{\sigma}^{(1)}(\omega,\omega')$ has poles, as a function of ω', at positions $\Delta_j - \Delta_k$, in which Δ's are the energies of states allowed to be excited: bright states [Eq. (3.34)] and LIS [Eqs. (3.35)-(3.36)]. In physical terms, the states excited by the XUV pulse interfere with each other, causing the oscillation in the XUV absorption spectrum. The energy of these oscillations is determined by the energy difference of these states.

3.5 Summary

Using the analytical framework presented in this chapter, one can roughly predict what kind of oscillations can be observed in a particular system under the action of overlapping fields, in the case when the system can be represented as a superposition of states. The analysis of the structure of $\sigma(\omega,\tau)$ and $\tilde{\sigma}(\omega,\omega')$ reveals how the cross section changes as a function of delay time τ. From Eqs. (3.25) and (3.24) it follows that nonzero cross section requires nonzero dipole moment:

$$\langle\Psi_0|\hat{Z}| \times (...)|\Psi_f\rangle\langle\Psi_f|(...) \times |\hat{Z}|\Psi_0\rangle, \tag{3.61}$$

where $\langle\Psi_f|(...) \times |\hat{Z}|\Psi_0\rangle$ corresponds to dipole matrix elements of excitation processes, and $\langle\Psi_0|\hat{Z}| \times (...)|\Psi_f\rangle$ corresponds to de-excitation process. Reading the total dipole matrix element and estimating which field is responsible for each transition I can figure out the amount of energy gained by the system at each step of excitation. Here I show it as an example of the excitation of the system from the ground state $|\Psi_0\rangle$ to the final state $|\Psi_f\rangle$ by one XUV photon ω_{xuv} and two dressing photons ω_d with a following de-excitation from the final to the ground state directly:

$$\underbrace{\langle\ \Psi_0\ |\ \hat{Z}\ |\ \Psi_f\ \rangle}_{E_0 - E_f - \omega'_{\text{xuv}}}\underbrace{\langle\ \Psi_f\ |\ \hat{Z}\ |\ \Psi_x\ \rangle}_{E_f - E_x \pm \omega_d}\underbrace{\langle\ \Psi_x\ |\ \hat{Z}\ |\ \Psi_y\ \rangle}_{E_x - E_y \pm \omega_d}\underbrace{\langle\ \Psi_y\ |\ \hat{Z}\ |\ \Psi_0\ \rangle}_{E_y - E_0 + \omega_{\text{xuv}}},$$

where $|\Psi_x\rangle$ and $|\Psi_y\rangle$ are the intermediate states which appear only in the presence of the dressing photon ω_d. Blue arrows represent the processes driven by the attosecond XUV field and red arrows represent the processes driven by the dressing pulse. The direction of the arrows (left or right) defines the type of the process (emission or absorption). Keeping in mind that the total amount of energy in a system remains conserved one can find the energy of the absorption peaks by reading the excitation dipole moment from right to left and summarize the energy gained by the system: from the first bracket I get main absorption peaks $\omega_{\text{xuv}} = E_0 - E_y$. The next steps give the energy of additional absorption peaks (LIS):

$$\begin{aligned} \omega_{\text{xuv}} &= E_0 - E_y + E_y - E_x \pm \omega_d = E_0 - E_x \pm \omega_d \\ \omega_{\text{xuv}} &= E_0 - E_y + E_y - E_x \pm \omega_d + E_x - E_f \pm \omega_d = \begin{cases} E_0 - E_f \\ E_0 - E_f \pm 2\omega_d \end{cases} \end{aligned} \tag{3.62}$$

The oscillation energies of those absorption peaks with a time delay τ may be retrieved in a similar way by simply adding together absorbed and emitted energy the way it is shown in a table below:

emission	absorption	corresponding oscillation
$E_0 - E_f - \omega'_{\text{xuv}}$	$E_y - E_0 + \omega_{\text{xuv}}$	$E_y - E_f$
	$E_x - E_0 \pm \omega_d + \omega_{\text{xuv}}$	$E_x - E_f \pm \omega_d + \omega_{\text{xuv}}$
	$E_f - E_0 \pm 2\omega_d + \omega_{\text{xuv}}$	$\pm 2\omega_d$
	$E_f - E_0 + \omega_{\text{xuv}}$	0

3.6 Conclusion

The analytical treatment of the ATA spectrum, presented in this chapter, provides an instrument to study the interference effects and correlations inside the system in detail. The presented technique is suitable not only for atoms, but for more complex systems as well. In the next chapter (Chapter 4) I demonstrate, using a model atom as an example, which effects can be recorded on the ATA spectrum and how different excitation pathways interfere with each other.

Chapter 4

Analysis of ATA signal of perturbatively dressed system

The results presented in this chapter have been published in Ref. [68], of which I am the first author, and has been included verbatim: Kolbasova, Santra, Appl. Sci., 9(7), 1350 (2019).

In order to have a better understanding of how the attosecond transient absorption signal reveals the real-time attosecond dynamics of the system I illustrate it by applying our analytical solution from Section 3.4 to a model atom. I focus on the situation in which the attosecond XUV pulse is used to create a coherent superposition of electronic states. The resulting dynamics can be detected in the spectrum of the transmitted XUV pulse by manipulating the electronic wave packet using a carrier-envelope-phase-stabilized optical dressing pulse. In addition to coherent electron dynamics triggered by the attosecond pulse, the transmitted XUV spectrum encodes information on electronic states made accessible by the optical dressing pulse. I illustrate these concepts through calculations performed for a few-level model.

4.1 Few-level model atom

By focusing on a simple few-level atom, I perform an analysis of the ATA signal dependence on the time delay between the attosecond XUV pulse and the optical dressing pulse. The model considered is shown in Figure 4.1. The corresponding energy levels and transition dipole matrix elements, which underlie the numerical results shown in the following, are presented in Tables 4.1 and 4.2, respectively. The numbers employed do not correspond to any real atom. In order to illustrate the basic features of the kind of ATA spectroscopy considered in this research, we employ an artificial few-level system characterized by level spacings matching XUV and optical energies. A key assumption is that parity is a good

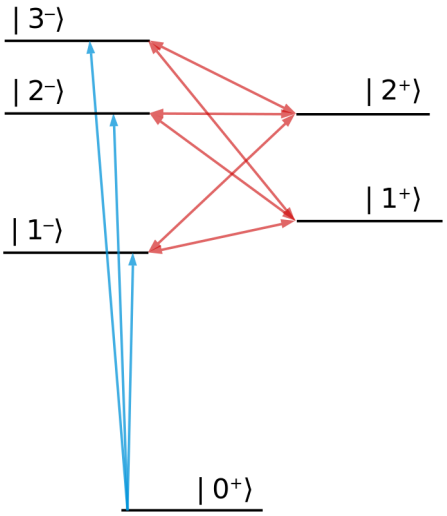

FIGURE 4.1: Level structure of the few-level atom employed to illustrate ATA spectroscopy. XUV transitions from the ground state are shown in blue. Red arrows indicate laser dressing of the excited states. The superscripts represent the parity of each state.

TABLE 4.1: Energy levels of the model atom in atomic units.

$\mathbf{E_{0^+}}$	$\boldsymbol{E_{1^-}}$	$\boldsymbol{E_{2^-}}$	$\boldsymbol{E_{3^-}}$	$\boldsymbol{E_{1^+}}$	$\boldsymbol{E_{2^+}}$
0	2.1888	2.2238	2.2360	2.1889	2.2238

quantum number, which allows us to clearly distinguish between bright and dark states (with respect to excitation from the ground state). The model in Figure 4.1 is intended as a pedagogical tool for identifying generic features of $\sigma^{(1)}(\omega,\tau)$ and $\tilde{\sigma}^{(1)}(\omega,\omega')$.

As a consequence of its large spectral bandwidth, the attosecond XUV pulse can excite the atom from its ground state 0^+ to any of the bright states i^-, $i=1,2,3$, which have a negative parity (see Figure 4.1). The dressing pulse with photon energy ω_d is weak and cannot, by assumption, affect the ground state, but can couple a bright state i^- to a dark state j^+, by exchanging with the atom one dressing-laser photon (energy change by $\pm\omega_d$) or to a bright state j^- by exchanging with the atom two dressing-laser photons (energy change by $\pm 2\omega_d$).

TABLE 4.2: Transition dipole matrix elements $\langle i^-|\hat{Z}|j^+\rangle$.

$\boldsymbol{\hat{Z}}$	$\boldsymbol{\|0^+\rangle}$	$\boldsymbol{\|1^+\rangle}$	$\boldsymbol{\|2^+\rangle}$
$\boldsymbol{\langle 1^-\|}$	0.25	0.33	0.33
$\boldsymbol{\langle 2^-\|}$	0.42	0.33	0.33
$\boldsymbol{\langle 3^-\|}$	0.33	0.33	0.33

Because 0^+ and the dark states j^+, $j = 1, 2$, have the same parity (see Figure 4.1), the latter cannot be excited via one-photon absorption from the ground state, i.e., the corresponding transition dipole moments are zero. However, in the presence of the dressing laser, they can give rise to light-induced states (LIS) [83, 84, 85]. In general, the energy of a LIS is determined by the energy difference to the dark state, however LIS associated with the valence transitions could be Stark shifted in the presence of the IR field. As a function of the XUV photon energy ω, the following transition energies can be observed in the transmitted spectrum of the attosecond pulse:

$\omega = E_{i^-} - E_{0^+}$ for a transition to a bright state i^-, and

$\omega = E_{i^+} \pm \omega_d - E_{0^+}$ and $\omega = E_{i^-} \pm 2\omega_d - E_{0^+}$, respectively, for LIS.

Excited states of the atom have a finite decay rate $\Gamma = \Gamma_f$ and relax through fluorescence or Auger decay, which leads to a finite width of the absorption peaks. In our model, the decay rate Γ is assumed to be the same for all excited states i^+ and i^- ($\Gamma = 1/263$ a.u.).

4.2 XUV induced dynamics inside the model atom

In Figure 4.2, the XUV one-photon cross section $\sigma^{(1)}(\omega, \tau)$ [Eq. (3.25)] for our model atom is presented for three different time delays τ. In all figures below I use a rectangular dressing pulse [see Eq. (3.33)] with amplitude $A_d = 0.06$ a.u., photon energy ω_d = 0.10 a.u. and duration $t_2 = 3141$ a.u. $\approx 11.95/\Gamma$ a.u., unless stated otherwise. As there are three bright states i^- in our model atom, one can see three main peaks in all panels of Figure 4.2, which correspond to the XUV transitions $0^+ \to i^-$. The small additional peaks in Figure 4.2 (b,c) correspond to transitions to LIS. Numerical values for the transition energies are listed in Table 4.3.

TABLE 4.3: Resonance energies (dressing photon energy ω_d = 0.10 a.u.).

	i=1	**i=2**	**i=3**
$\boldsymbol{E_{i^-} - E_{0^+} - 2\omega_d}$	1.9889	2.0238	2.0361
$\boldsymbol{E_{i^-} - E_{0^+}}$	2.1888	2.2238	2.2360
$\boldsymbol{E_{i^-} - E_{0^+} + 2\omega_d}$	2.3888	2.4238	2.4360
$\boldsymbol{E_{i^+} - E_{0^+} - \omega_d}$	2.089	2.124	
$\boldsymbol{E_{i^+} - E_{0^+} + \omega_d}$	2.289	2.324	

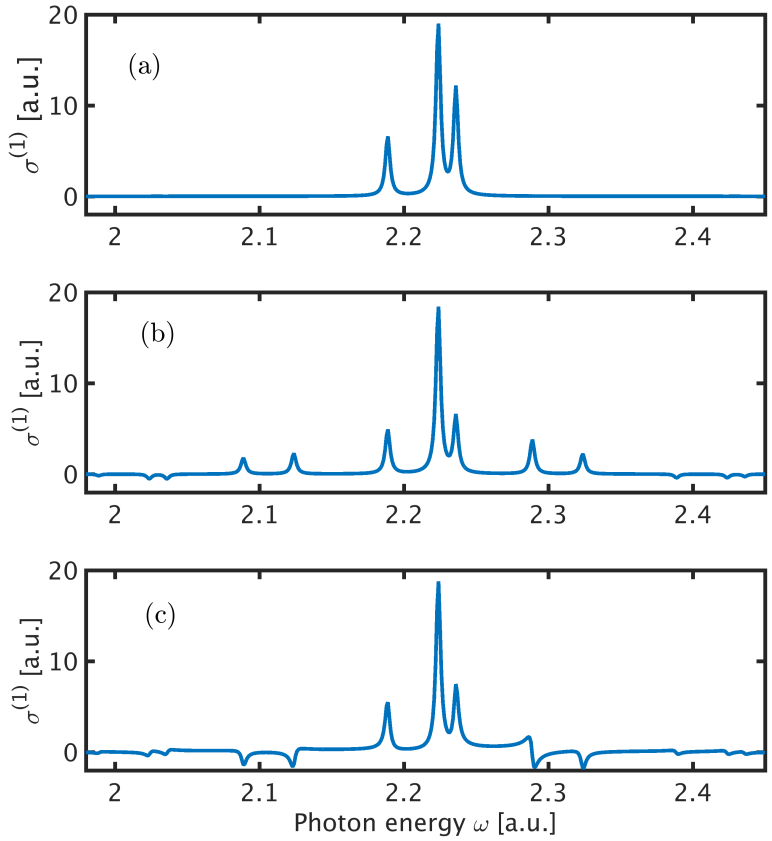

FIGURE 4.2: Atomic cross section $\sigma^{(1)}(\omega, \tau)$ of a model atom dressed by a laser pulse with a field strength $A_d = 0.06$ a.u., photon energy $\omega_d = 0.10$ a.u. and duration $t_2 = 3141$ a.u. $\approx 11.95/\Gamma$ a.u., at different excitation time delay: (a) $\tau \ll -1/\Gamma$; (b) $\tau = 0$; (c) $\tau = -0.05/\Gamma$. Panel (a) corresponds to a cross section of a non-dressed model atom, only three main absorption peaks are present. Small side peaks on panels (b) and (c) correspond to LIS, which can be detected on a ATA spectrum as an emitted light (positive cross section) or absorbed light (negative cross section).

If dressing comes long after or before the excitation by the attosecond pulse, only the peaks associated with the bright states can be observed in the absorption spectrum as illustrated in Figure 4.2 (a). When the time delay between the pulses gets shorter, optical dressing becomes possible, causing the appearance of LIS transition peaks as well as changes in the height of the bright-state transition peaks. New features can be positive or negative indicating whether the attosecond XUV beam is attenuated or amplified at the corresponding photon energy ω.

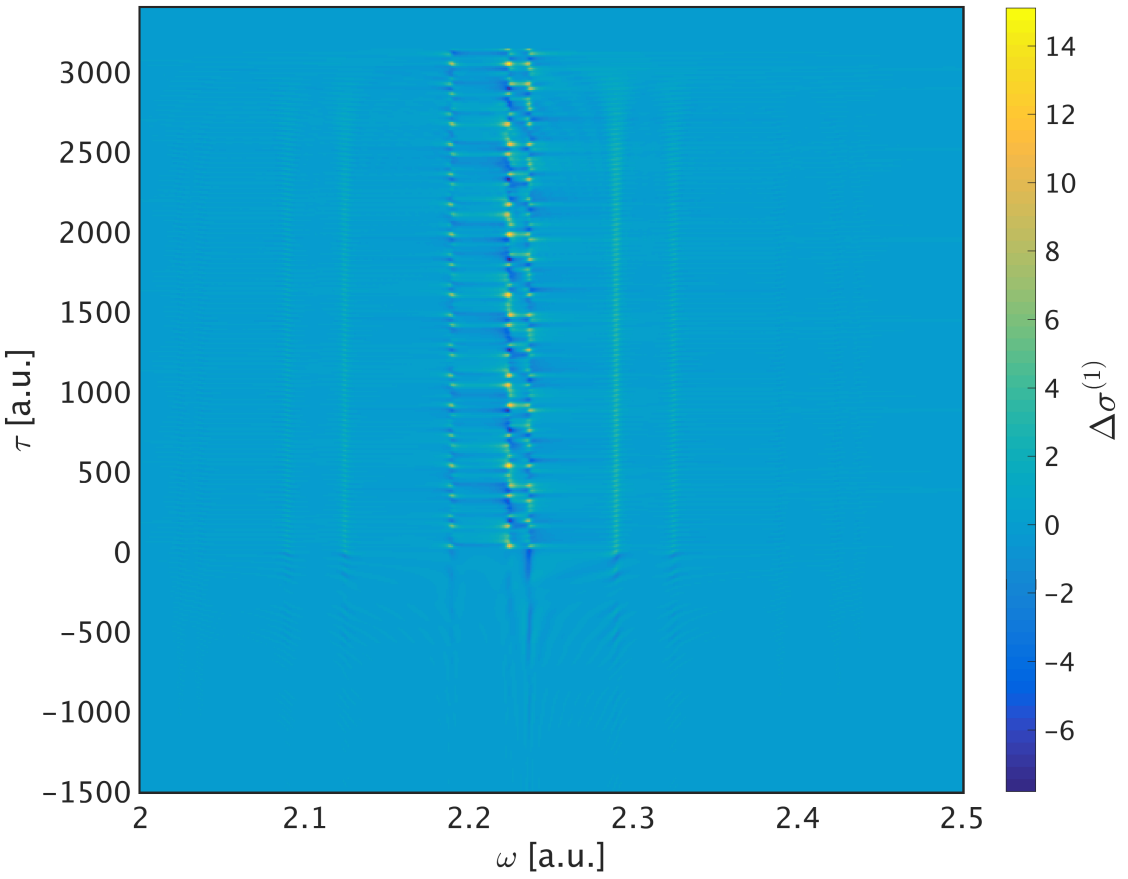

FIGURE 4.3: Difference in absorption spectrum of attosecond XUV pulse $\Delta_{\sigma^{(1)}} = \sigma^{(1)}(\omega,\tau) - \sigma^{(1)}(\omega,\infty)$ caused by delayed dressing by NIR pulse (Eq. 3.33). The time delay τ between the attosecond XUV pulse and start $t_1 = 0$ a.u. of a NIR pulse is shown in y-axes, and the photon energy ω is shown on x-axes. In the middle of the plot one can see three main absorption peaks oscillating with the time delay τ in the overlapping region [0 3141 a.u.]. Blurring yellow lines on the sides from the main absorption peaks correspond to a LIS, which become accessible in a presence of a dressing field.

In Figure 4.3 the full map of a difference $\Delta\sigma^{(1)} = \sigma^{(1)}(\omega,\tau) - \sigma^{(1)}(\omega,\infty)$ is shown as a function of photon energy ω and excitation time delay τ. Interference of different excitation paths from the ground state 0^+ to a final f state [see Eq. (3.25)] gives rise to an oscillation in the XUV one-photon cross section of all peaks [86], which can be observed in Figure 4.3 in the overlap region between the optical dressing pulse and the attosecond XUV pulse. Focusing at the LIS peaks in Figure 4.3 one can see that the oscillations become weaker after

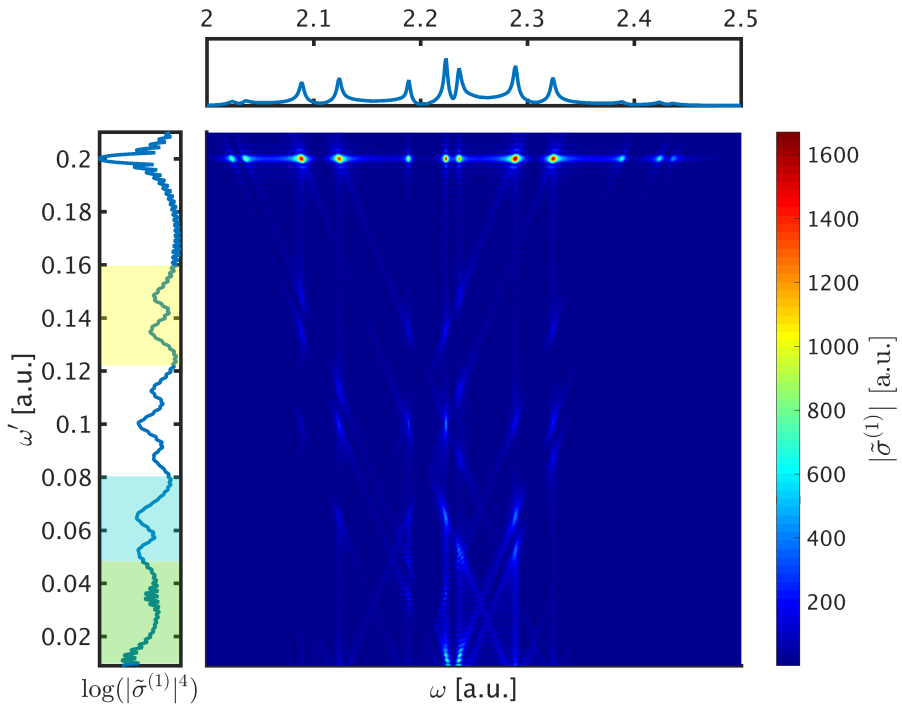

FIGURE 4.4: $|\tilde{\sigma}^{(1)}(\omega,\omega')|$, i.e., the modulus of the Fourier transform of the XUV one-photon cross section $\sigma^{(1)}(\omega,\tau)$, calculated with Eq. (3.54). Upper panel represents the the integral of $|\tilde{\sigma}^{(1)}(\omega,\omega')|$ over Fourier range, and the left panel the integral over photon energy range.

$\tau \approx 2230$ a.u. as the time available to dress an excited state gets shorter and becomes comparable with the excited-state lifetime. Thus, the probability of interference with another transition path through a dressed state goes down. This "ringing" of the system driven by the excitation pulse can be observed even if the dressing pulse comes after the excitation and the pulses do not overlap, if the excited state can survive till the dressing comes. This can be seen in the region of negative τ in Figure 4.3. Finally, if the attosecond pulse comes after the dressing pulse, the XUV one-photon cross section remains constant and the height of the three main peaks at $\omega = E_{i^-} - E_{0^+}$ does not change with the time delay τ, as the dressing pulse, by assumption, does not affect the ground state of the system.

Studying the "ringing" allows us to reveal the real-time attosecond dynamics inside the atom. To this end, I take the Fourier transform of $\sigma^{(1)}(\omega,\tau)$ with respect to the time delay, which gives an opportunity to study the reasons behind the oscillations observed. The absolute value of the resulting function $\tilde{\sigma}^{(1)}(\omega,\omega')$ [Eq. (3.54)] is plotted in Figure 4.4. The oscillations of $\sigma^{(1)}(\omega,\tau)$, caused by the excitation-paths interference, have the energies $\omega' = \Delta_i - \Delta_j$ [see Sec. 3.4]. In accordance with the dipole selection rules, these are

TABLE 4.4: Oscillation energies ω' [a.u.] of the ATA peaks, dependent on the electronic structure of the atom ($2\omega_d = 0.20$ a.u. is not in the table).

	i=1	**i=2**	**i=3**
$\lvert \boldsymbol{E_{i^-}} - \boldsymbol{E_{(i+1)^-}} \rvert$	0.0350	0.0122	0.0472*
$\lvert \boldsymbol{E_{1^+}} - \boldsymbol{E_{i^-}} + \boldsymbol{\omega_d} \rvert$	0.1000	0.0650	0.0528
$\lvert \boldsymbol{E_{2^+}} - \boldsymbol{E_{i^-}} + \boldsymbol{\omega_d} \rvert$	0.1350	0.1000	0.0878
$\lvert \boldsymbol{E_{1^+}} - \boldsymbol{E_{i^-}} - \boldsymbol{\omega_d} \rvert$	0.0999	0.1350	0.1472
$\lvert \boldsymbol{E_{2^+}} - \boldsymbol{E_{i^-}} - \boldsymbol{\omega_d} \rvert$	0.0650	0.0999	0.1122

* *Energy difference* $E_{3^-} - E_{1^-}$

$$\omega' = 2\omega_d,$$

$$\omega' = |E_{i^-} - E_{j^-}|,$$

$$\omega' = |E_{i^+} - E_{j^-} \pm \omega_d|.$$

Corresponding values for our model atom are shown in Table 4.4. All these energies are present in the oscillations of main peaks of the ATA spectrum, except those that do not include this concrete state in the interference process, such as $\omega' = |E_{i^-} - E_{j^-}|$ for the absorption peak $\omega = |E_{k^+} - E_{0^+}|$, where $k \neq i$ and $k \neq j$.

Set of peaks of the Fourier spectrum of the XUV one-photon cross section (which is projected onto the ω'-axis in Figure 4.4 is marked with a green color), corresponds to the energy differences

$$\omega' = |E_{i^-} - E_{j^-}|.$$

They appear due to the coupling of two bright i^- states by the dressing field. This makes it possible for the atom to be excited into the state i^- with a following de-excitation from the j^- state. The rest of the peaks of the Fourier spectrum of the XUV one-photon cross section, except the peaks at the $\omega' = 2\omega_d$, are caused by the interference of the bright state with a LIS. These interferences can be observed as diagonal features, which go from one interfering state to another. In such a way, in the middle of Figure 4.4 there are the peaks corresponding to the energy differences,

$$\omega' = |E_{i^-} - E_{j^+} \pm \omega_d|,$$

which are caused by the interference of the bright state E_{i^-} with a LIS $\omega = E_{j^+} \pm \omega_d$. To be more precise, the oscillation energies marked in blue on the left in Figure 4.4 correspond to the oscillations caused by the interference of the state i^- ($i = 2, 3$) with the positively dressed LIS ($\omega = E_{1^+} + \omega_d$):

$$\omega' = |E_{1^+} - E_{i^-} + \omega_d|,$$

and interference of the state 1^- with the negatively dressed LIS ($\omega = E_{2^+} - \omega_d$)

$$\omega' = |E_{2^+} - E_{1^-} - \omega_d|.$$

In a same way, the oscillation energies marked with yellow color correspond to the case of opposite sign of a dressing:

$$\omega' = |E_{1^+} - E_{i^-} - \omega_d|,$$

and

$$\omega' = |E_{2^+} - E_{1^-} + \omega_d|.$$

The remaining energies of this type in the very middle of Figure 4.4 correspond to:

$$\omega' = |E_{2^+} - E_{3^-} \pm \omega_d|.$$

Oscillation at the energy $\omega' = 2\omega_d = 0.2$ a.u. is characteristic for all cross section peaks. This feature was theoretically predicted and measured as subcycle fringes in laser-dressed helium atoms [83, 84, 85]. It is noteworthy that the oscillation energy of these LIS peaks depends only on the photon energy of the dressing pulse and not on the electronic structure of the atom. In contrast, the energy $\omega' = |E_{i^-} - E_{j^-}|$ of the main peaks' oscillations does not depend on the energy of the dressing pulse at all, which testifies that the XUV excitation creates a coherent superposition of the i^- states.

4.3 Analysis of sensitivity of ATAS

In this section I analyze the dependence of the oscillation strengths on parameters of the system and the parameters of the dressing pulse to see which information could be imprinted on a ATAS spectrum and what the conditions are to observe them.

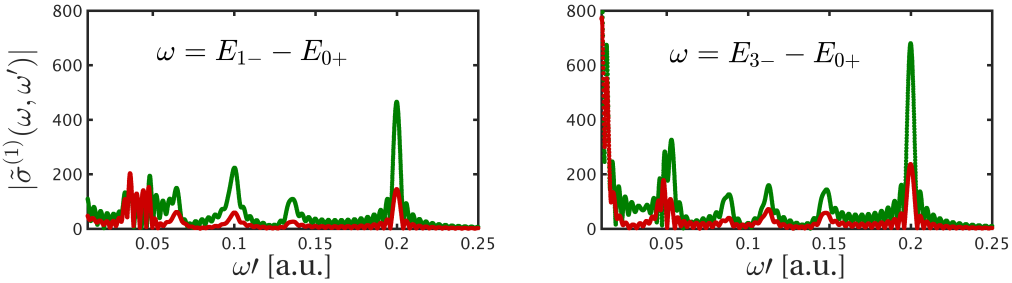

FIGURE 4.5: Fourier spectrum of the oscillations it the dressing field ω_d = 0.10 a.u. of the absorption lines $\omega = E_{3^-} - E_{0^+}$ and $\omega = E_{1^-} - E_{0^+}$ (green: $\langle 3^-|\hat{Z}|0^+\rangle = 0.33$; red: $\langle 3^-|\hat{Z}|0^+\rangle = -0.33$).

One of the important atomic parameters is the transition dipole matrix element between two states$\langle i^-|\hat{Z}|j^-\rangle$. Its magnitude defines the probability of the dipole transition. In Figure 4.2 one can see that the Fourier peaks of the transition into 1^- are markedly weaker in comparison with 2^- and 3^-, as the 1^- transition dipole matrix element from the ground state is smaller (see Table 4.2). Moreover, our results obtained with Eq. (3.54) show a sensitivity of ATA spectroscopy to the relative signs of the transition dipole matrix elements involved in the process. In Figure 4.5, I compare Fourier spectra of the oscillations of two different absorption peaks, where two cases are shown that differ from each other only through the sign of the transition dipole matrix. One can see significant changes in the amplitude of the Fourier peaks not only in the spectrum at $\omega = E_{3^-} - E_{0^+}$, which directly depends on parameters of the 3^- state, but also in the spectrum at $\omega = E_{1^-} - E_{0^+}$. This underscores the strong effective coupling between the 3^- and 1^- states. The change of the relative phase of these two dipole moments strongly affects the oscillation amplitudes that are explicitly dependent on transitions into LIS, whereas oscillations at the energies $\omega' = E_{i^-} - E_{j^-}$ remain almost the same (the $\omega' = E_{3^-} - E_{1^-} = 0.0472$ a.u. on Figure 4.5). The sensitivity to the relative phase, for transitions into LIS, can be understood as follows. If two bright states, here 1^- and 3^-, are coupled by the dressing pulse to a dark state j^+, and the products $\langle 0^+|\hat{Z}|1^-\rangle\langle 1^-|\hat{Z}|j^+\rangle$ and $\langle 0^+|\hat{Z}|3^-\rangle\langle 3^-|\hat{Z}|j^+\rangle$ have opposite signs, then their contributions to the corresponding LIS peaks will attenuate each other. As a consequence of the destructive interference of the two pathways to the state j^+, the LIS peaks are suppressed.

The impact of the parameters of the dressing pulse is shown in Figure 4.6. The panels show $\tilde{\sigma}^{(1)}(\omega,\omega')$ for the absorption peaks $\omega = E_{1^-} - E_{0^+}$ (green line) and $\omega = E_{1^+} - E_{0^+} + \omega_d$ (red line) calculated with Eq. (3.54) for two different dressing photon energies $\omega_d = 0.10$ a.u. (left panels) and $\omega_d = 0.15$ a.u. (right panels) and different durations $t_2 - t_1$ of the dressing pulse. Comparing the left and right panels of Figure 4.6 one can see that position of the peaks $\omega' = E_{i^-} - E_{j^-}$ remain unaffected, and the peaks that depend on ω_d are shifted.

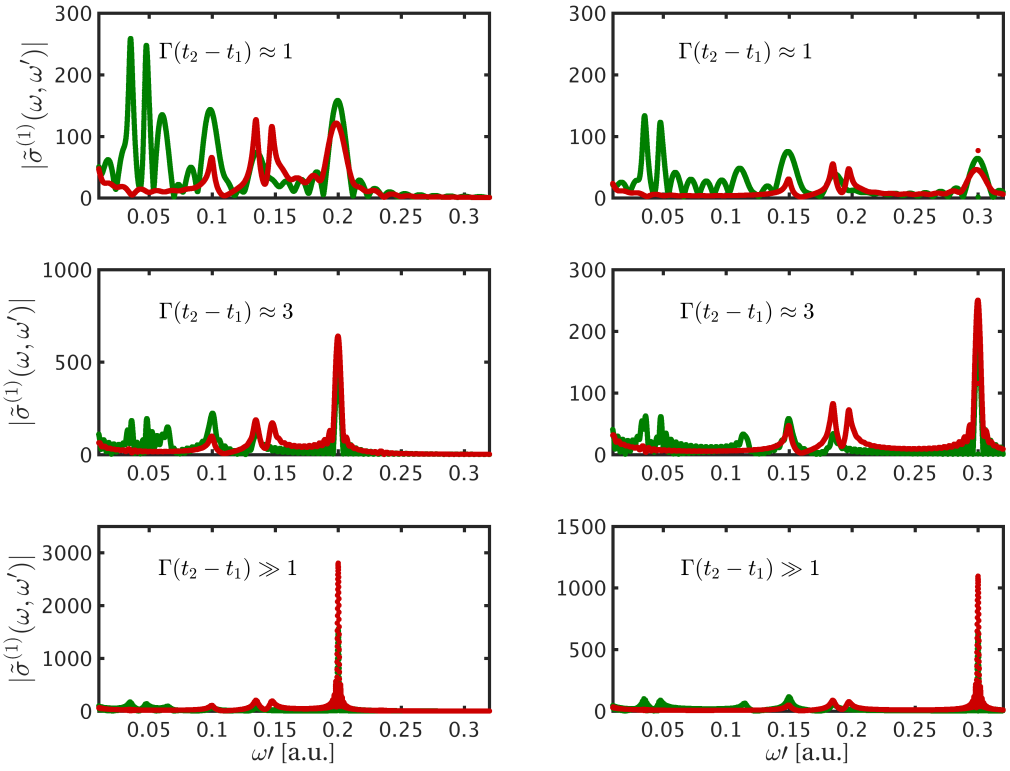

FIGURE 4.6: Fourier spectra $\tilde{\sigma}^{(1)}(\omega, \omega')$ at $\omega = E_{1^-} - E_{0^+}$ (green line) and $\omega = E_{1^+} - E_{0^+} + \omega_d$ (red line) for different pulse durations of the dressing field (decay rate of all excited states Γ is kept constant). The pulse durations used are integers of the dressing field period. Left and right panels correspond to the dressing photon energies ω_d = 0.10 a.u. and ω_d = 0.15 a.u., respectively.

As the effective coupling strength depends on the photon energy of the dressing field, the amplitudes of all peaks are affected by the ω_d change. The peak heights are sensitive to how close ω_d is to a resonant transition energy between the states i^- and j^+. With increasing dressing-pulse duration the relative heights of the peaks remain the same and all the peaks become sharp and clear.

In Figure 4.7 $|\tilde{\sigma}^{(1)}(\omega, \omega')|$ is shown, i.e., the modulus of the Fourier transform of the XUV one-photon cross section $\sigma^{(1)}(\omega, \tau)$, calculated with Eq. (3.54), calculated separately for the regions $\tau < t_1$ and $t_1 < \tau < t_2$. In case of the XUV excitation happening strictly before the dressing pulse the initial wave packet is simply a superposition of bright states. The dynamics inside the system will be defined by the evolution of this wave packet with time. However if the life time of the excited state is long enough for the state to survive until the

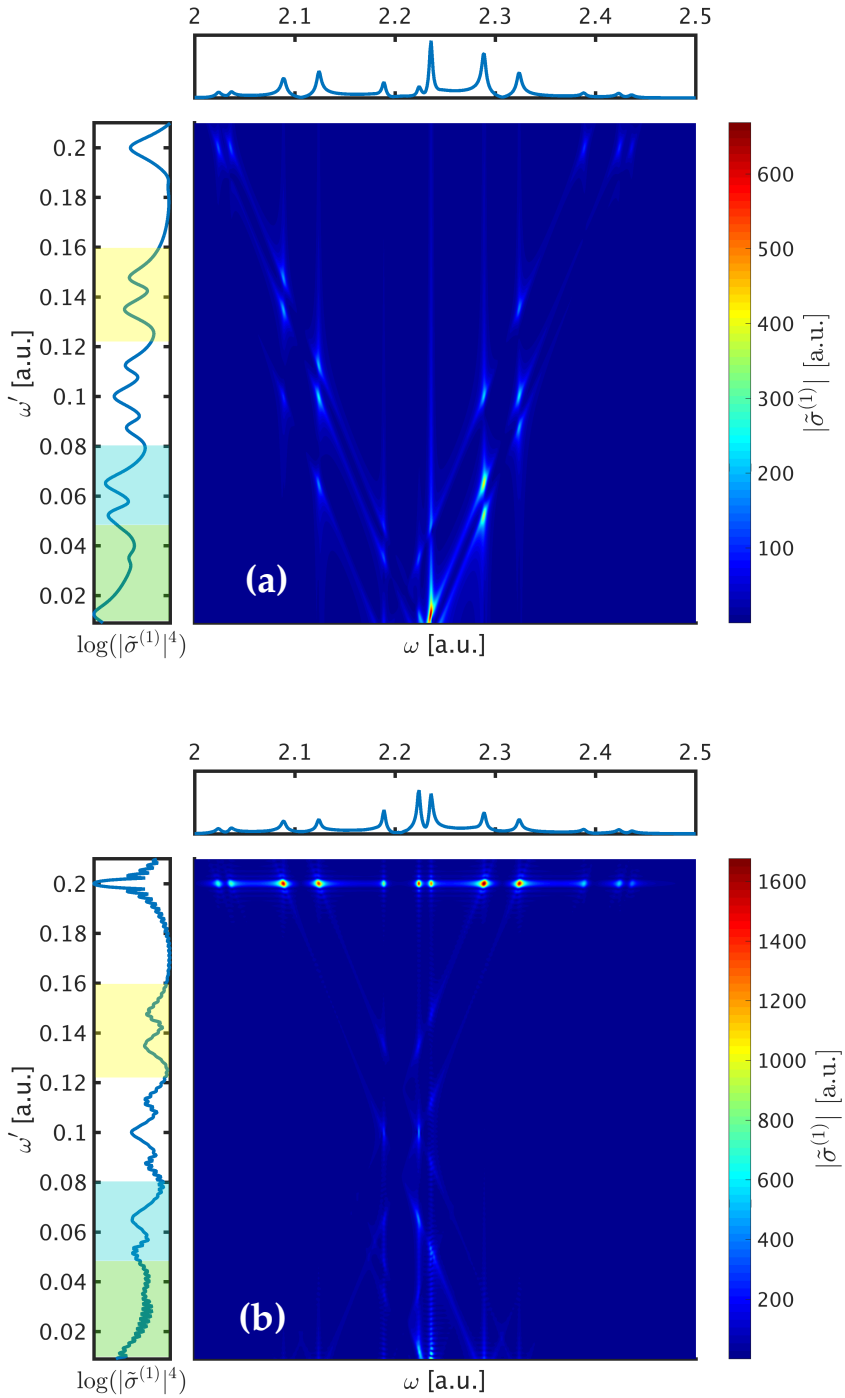

FIGURE 4.7: $|\tilde{\sigma}^{(1)}(\omega, \omega')|$, i.e., the modulus of the Fourier transform of the XUV one-photon cross section $\sigma^{(1)}(\omega, \tau)$, calculated with Eq. (3.54) separately for the region (a) $\tau < t_1$ and (b) $t_1 < \tau < t_2$.

dressing field comes, it can decay after being dressed. For these reasons in Figure 4.7 (a) not only the bright peaks $\omega = E_{i^-}$ of a cross section are imprinted, but the dark states as well. All the cross section peaks oscillate with the energy $\omega' = E_k - E_{i^-}$, where E_k is the energy of a cross section peak of the photon energy ω. If the excitation by the XUV pulse happens in a presence of a dressing pulse, initial wave packet is a superposition of the bright states together with LIS. It provides much more complicated dynamics inside the system. In Figure 4.7 (b) the oscillations of the main cross-section peaks ($\omega = E_{i^-} - E_0$) are not restricted by $\omega' = E_{j^-} - E_{i^-}$ components, but also indicate an interference with all LIS through the $\omega' = E_{LIS} - E_{i^-}$ oscillations. All the possible oscillations are imprinted on a Fourier transform spectrum of the XUV one-photon cross section $t_1 < \tau < t_2$, but the oscillations caused by the excited state interference of the main peaks are more prominent than those for the LIS. For the later ones, whose accessibility strongly depends on a a period of the dressing field, oscillation $\omega' = 2\omega_d$ is so much stronger that the inference packs are not visible.

In Figure 4.8 the influence of different excitation paths in $|\tilde{\sigma}^{(1)}(\omega, \omega')|$ are explored separately from each other. We evaluate the $|\tilde{\sigma}^{(1)}(\omega, \omega')|$ from Eq. (3.54) reducing the set of possible excitation scenarios. Function $\tilde{\mathcal{F}}_f(\omega, \omega')$ from Eq. (3.56) can be decomposed as:

$$\tilde{\mathcal{F}}_f(\omega, \omega') = \sum_{abcd} \tilde{\mathcal{F}}_f^{abcd}(\omega, \omega'), \tag{4.1}$$

where

$$\tilde{\mathcal{F}}_f^{abcd}(\omega, \omega') = \int_{-\infty}^{\infty} d\tau \tilde{F}_{0f}^{ab}(\omega, \tau) F_{f0}^{cd}(\tau) e^{i(\omega' - \omega)\tau}. \tag{4.2}$$

Taking into account second order of perturbation by the dressing pulse, function $\tilde{\mathcal{F}}_f(\omega, \omega')$ in general reads

$$\tilde{\mathcal{F}}_f(\omega, \omega') = \tilde{\mathcal{F}}_f^{0020}(\omega, \omega') + \tilde{\mathcal{F}}_f^{0110}(\omega, \omega') + \tilde{\mathcal{F}}_f^{0200}(\omega, \omega') + \tilde{\mathcal{F}}_f^{0220}(\omega, \omega'). \tag{4.3}$$

The last term requires interaction with 4 dressing photons instead of 2, so the probability of the corresponding processes is negligibly small comparing to the processes described by the other terms. In Figure 4.8 we solve Eq. (3.54) considering the $\tilde{\mathcal{F}}_f(\omega, \omega')$ to be equal to:

(a) simply the $\tilde{\mathcal{F}}_f^{0200}(\omega, \omega')$ term

(b) all terms except $\tilde{\mathcal{F}}_f^{0200}(\omega, \omega')$: in other words $\tilde{\mathcal{F}}_f^{0110}(\omega, \omega') + \tilde{\mathcal{F}}_f^{0020}(\omega, \omega')$.

Similar for the lower panels of Figure 4.8:

(c) $\tilde{\mathcal{F}}_f^{0110}(\omega,\omega')$, and

(d) $\tilde{\mathcal{F}}_f^{0020}(\omega,\omega') + \tilde{\mathcal{F}}_f^{0200}(\omega,\omega')$,

(e) $\tilde{\mathcal{F}}_f^{0020}(\omega,\omega')$ and

(f) $\tilde{\mathcal{F}}_f^{0200}(\omega,\omega') + \tilde{\mathcal{F}}_f^{0110}(\omega,\omega')$.

This representation give us a way to see clearly that the $\tilde{\mathcal{F}}_f^{0200}(\omega,\omega')$ term is responsible for the situations described above for the Figure 4.7 (a), and $\tilde{\mathcal{F}}_f^{0020}(\omega,\omega')$ describes the opposite situation, when the initial wave packet is a superposition of the bright and light-induced states, but is allowed to decay only through one of the bright states. Finally, the term $\tilde{\mathcal{F}}_f^{0110}(\omega,\omega')$ represents the situation where both excited and decaying states in a process have to be one-time dressed.

It is worthy of note that some of the terms interfere constructively whereas another terms interfere destructively. An example of constructive interference are the terms $\tilde{\mathcal{F}}_f^{0200}(\omega,\omega')$ and $\tilde{\mathcal{F}}_f^{0020}(\omega,\omega')$, shown in Figures 4.8 (a) and (e) correspondingly. In a summation they give exactly the $\tilde{\mathcal{F}}_f^{0020}(\omega,\omega') + \tilde{\mathcal{F}}_f^{0200}(\omega,\omega')$ picture, shown in Figure 4.8 (d). The term $\tilde{\mathcal{F}}_f^{0110}(\omega,\omega')$ instead interferes with two other terms destructively. The result of its interference with the $\tilde{\mathcal{F}}_f^{0200}(\omega,\omega')$ or $\tilde{\mathcal{F}}_f^{0020}(\omega,\omega')$ terms removes the oscillation frequencies in common from the $|\tilde{\sigma}^{(1)}(\omega,\omega')|$ picture, as imprinted in Figure 4.8 (b) and Figure 4.8 (f) correspondingly. As one can see in Figure 4.4 the strongest oscillation for all cross-section peaks is $\omega' = 2\omega_d$, and observation of the frequencies, which reflect more interesting wave-packet dynamics is complicated.

4.4 Conclusion

We have applied our analytical theory of attosecond transient absorption spectroscopy for perturbatively dressed systems (see Chapter 3), to a model atom in order to study in detail which aspects of real-time attosecond dynamics inside the atom can be revealed from the ATA spectrum. When a broadband attosecond XUV pulse excites a superposition of bright states, the presence of an optical dressing pulse gives rise to modulations of the absorption peaks connected to the population of bright states and, in addition, allows the population of LIS, which can be observed as new absorption lines in the ATA spectrum. Their positions depend on the photon energy of the dressing pulse. The modulations of the bright-state absorption peaks are caused by the dressing-laser-driven coherent coupling of the bright states to dark states and, via the dark states, to other bright states. The amplitude of a bright state excited by the attosecond XUV pulse can, thus, be enhanced or reduced via

population transfer from or to other bright states by the dressing pulse. Therefore, the interference between the direct and the dressing-field-mediated pathways gives rise to periodic modulations of the bright-state absorption peaks as a function of the pump-probe delay. The energies associated with these modulations do not depend on the photon energy of the optical dressing pulse but on the energy differences among the bright states coherently populated by the attosecond XUV pulse. The developed theory also shows the sensitivity of ATA spectroscopy to the relative signs of the transition dipole moments among the states involved in the interaction. A change in sign affects the interference of different quantum pathways, which can be observed via the strength of the corresponding modulations of an absorption peak.

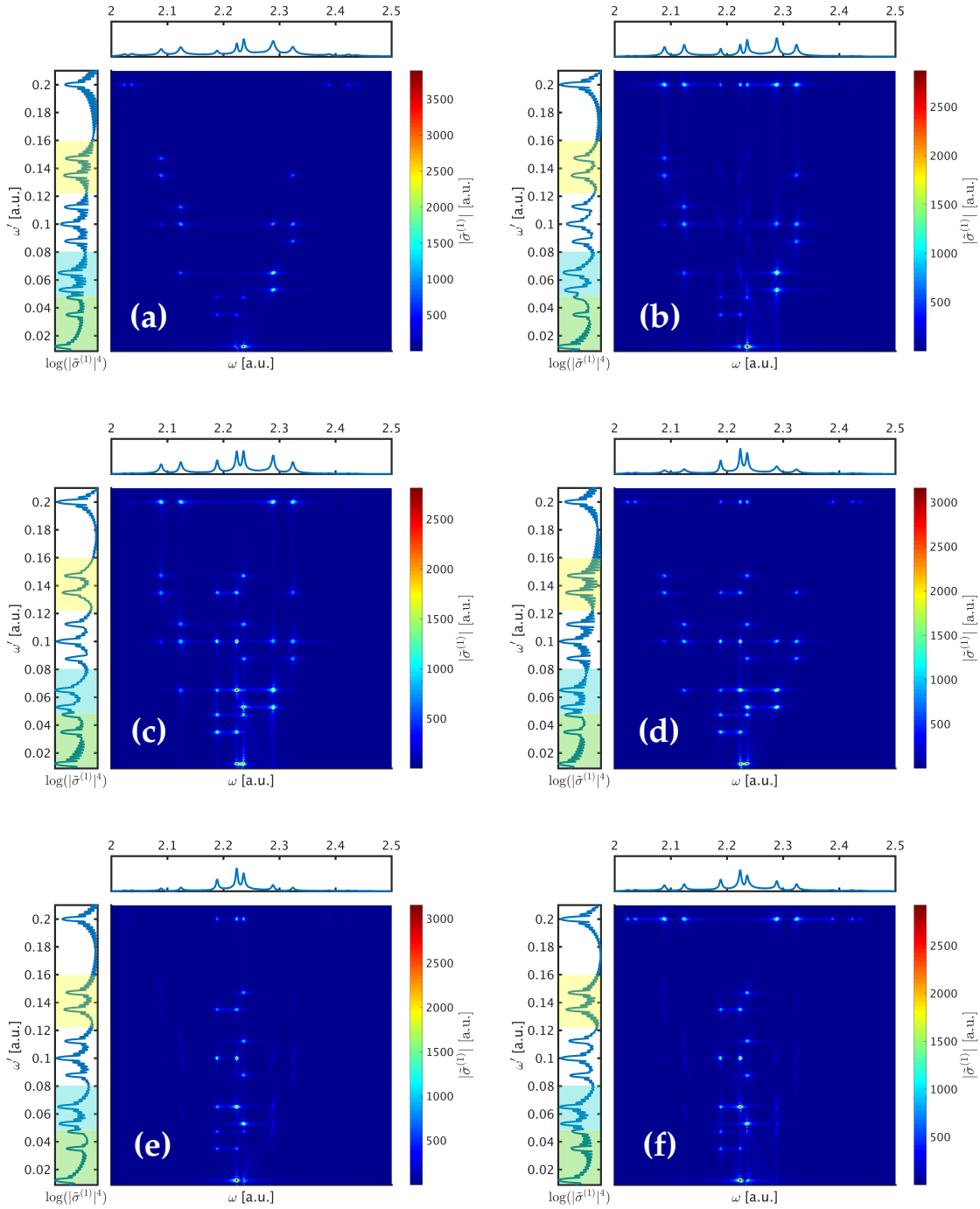

FIGURE 4.8: Individual impact of different excitation paths in ATAS spectrum $|\tilde{\sigma}^{(1)}(\omega, \omega')|$ and their interference. The oscillations caused by (a) excitation by one XUV photon and decay from a dressed state; (c) excitation and decay from the dressed states; (e) excitation to a dressed state and decay form non-dressed state are shown in the left column. On the right side (b,d,f) ATAS spectra calculated excluding the corresponding term from the left side (a,c,e) are shown.

Chapter 5

Numerical simulation of ATA signal of dressed Xe atom

Some of the results presented in this chapter have been published in Ref. [69], of which I am the first author, and has been included verbatim:
Kolbasova, Hartmann, Jin, Blättermann, Ott, Son, Pfeifer, Santra, Phys. Rev. A **103**, 043102 (2021).

Here, I explore the possibility of the experimental observation of core-excited wave-packet coherence by ATAS of Xenon. By using an attosecond XUV pulse a core-excited wave packet is initiated. In order to probe the wave packet and monitor its evolution in time, a time-delayed ultrashort laser pulse in the near-infrared (NIR) regime is employed and the resulting modification of the transmitted XUV spectrum is detected. The main goal of my study is to explore XUV-NIR transient absorption spectra and to elucidate as to whether excited-electron dynamics or inner-shell hole dynamics are encoded in the time-resolved spectra. In the previous Chapter 4 I provided an elementary explanation of the signals one can obtain in ATAS experiments based on a perturbative treatment for both pump and probe pulses. In the current work, I apply a non-perturbative treatment for the probe pulse to accommodate a wide range of experimentally accessible pulse properties. In the end of this chapter I provide a comparison of our theoretical predictions with the experiment carried out by T. Pfeifer's group.

In order to make a careful comparison with experiment it is crucial to use the exact shape of the pulse in simulation. The analytical treatment I present in a previous chapter is not possible for any shape of the laser pulse. Thus in this chapter I investigate the possibility

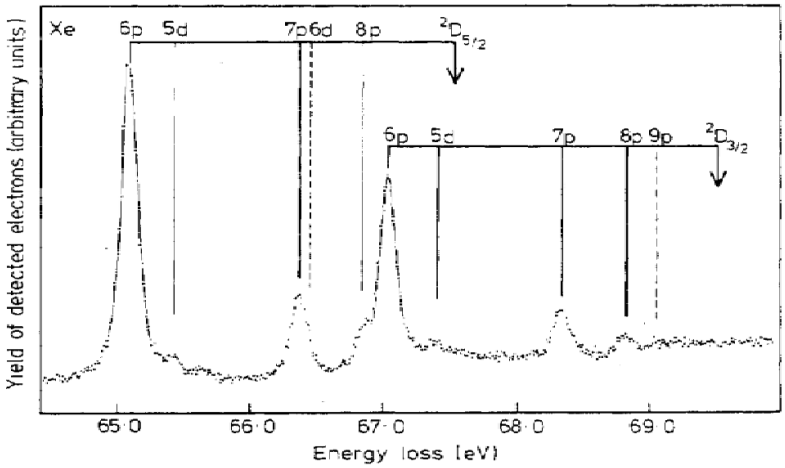

FIGURE 5.1: Energy-loss spectrum of xenon, obtained at an incident electron energy of 1.5 keV and with an energy resolution of 70 meV. The broken lines indicate the probable positions of weak transitions. Figure is taken from [87] (DOI: 10.1088/0022-3700/10/12/026).

of the experimental observation of core-excited wave-packet coherence by ATAS by *numerical* simulations for the Xe atom. Particularly, I am interested in two scenarios: when the initial wave-packet dynamics is induced by XUV only - similarly to the situation discussed in a previous chapter; and when the initial wave-packet dynamics is induced by XUV in the presence of an additional optical dressing field. In the considered setup a broadband XUV pulse with a central frequency $\omega_{\text{xuv}} \approx 65$ eV resonantly excites an electron from the $4d$ shell populating Rydberg states. Energies of the excited states of Xe were experimentally investigated by G.C. King et al. using electron impact with high resolution. The energy-loss spectrum of xenon, obtained at an incident electron energy of 1.5 keV is presented in Figure 5.1, which is taken from Ref. [87]. In this spectrum one can see the peaks corresponding to bright states ($4d^{-1}np^1$), which could be excited from the Xe ground state by absorption of one XUV photon, and two dark states $4d^{-1}5d^1$ and $4d^{-1}6d^1$. Other states, such as ns or nf, were too difficult to detect in their experiment.

We perform simulations of the XUV-NIR transient absorption spectra for Xe atom, excited by XUV in the absence and presence of an additional dressing field using the XCID code [80]. We use the calculated dipole moment $D^{(1)}(t)$ to find $|\tilde{\sigma}^{(1)}(\omega, \omega')|$ employing Eqs. (3.21) and (3.53). The result of Fourier transformed ATA signal is presented in Figure 5.2. In accordance with the theoretical predictions from the previous chapters, Figure 5.2 (a) illustrates the oscillations $\omega' = 2\omega_{IR}$ for all absorption peaks. The presence of the dressing pulse provides an additional oscillation energy $\omega' = \omega_{IR}$.

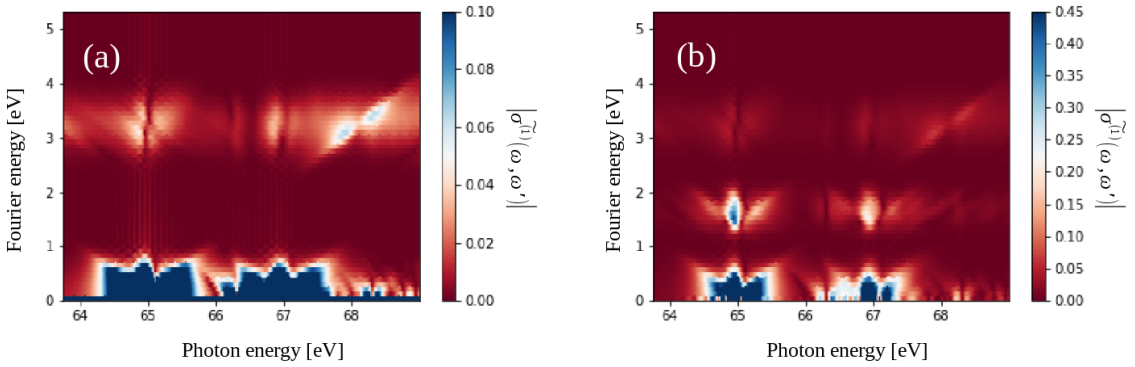

FIGURE 5.2: Fourier transformed ATA signal of Xe atom induced by a time-delayed NIR pulse and (a) XUV, or (b) XUV in the presence of an additional NIR dressing field. $|\tilde{\sigma}^{(1)}(\omega,\omega')|$ is calculated with XCID code. XUV pulse parameters: $\omega_{\text{xuv}} = 65.28$ eV, duration 0.4 fs, strength 3.5 TW/cm^2; NIR pulse parameters: $\omega_{\text{IR}} = 1.66$ eV, duration ≈ 5 fs, strength 1.12 TW/cm^2. Dressing field is a copy of an NIR pulse ($\approx 5\%$ of its intensity), centered and propagated together with the XUV pulse.

Since relativistic effects in the Xe atom can play an important role in the processes under investigation, some transitions that may be observed in a real experiment are not covered in our XCID calculations. To be able to verify the significance of relativistic effects in Xe core-hole dynamics I also perform numerical calculations using the Xe model, which is built using relativistic configuration-interaction method. More specifically, relativistic effects are taken into account using the Dirac-Coulomb Hamiltonian and the basis wave functions are obtained from a local potential corresponding to an effective average configuration [88, 89]. Since the angular quantum number j of the electronic hole is not expected to be conserved in fully relativistic atomic-structure theory, the actual eigenstates, which could be probed in ATAS experiment cannot be expected to have well-defined j. Indeed, the calculations with the relativistic multiconfiguration Dirac-Hartree-Fock method show that some states of Xe are a mixture of configurations with different angular momentum j of the hole. Taking into account such states allows to capture in our numerical calculations the transitions that can not be reproduced by TDCIS.

5.1 Calculation of atomic parameters for Xe

To build a reliable atomic model it is crucial to use realistic parameters for the states involved. Even though there are lots of experimental data available regarding electromagnetic transitions in various atomic species, these data are not sufficiently complete. Therefore, the first-principles atomic-structure software is employed to calculate the missing information.

In the simulations presented in this chapter, I use the atomic structure and transition dipole matrix elements calculated by R. Jin with the Flexible Atomic Code (FAC) [90]. A set of orbitals is constructed based on the Dirac-Fock-Slater effective local potential for the ground configuration of neutral Xe. A diagonalization of the Hamiltonian matrices for core-excited states is performed which are constructed from initial and final nonrelativistic electron configurations.

Further, I employ transition energies from experimental data [87, 91], whenever available, and complement them with energies from the FAC calculations. Only few Xe $4d$-excited dark states have been so far observed experimentally. For those known levels, our FAC calculations differ almost uniformly from experimental values by $\sim 1.7\,\mathrm{eV}$. Accordingly, I correct all calculated energies using this shift.

In the Xe model employed I distinguish between bright (dipole-allowed) and dark (dipole-forbidden) states. I include the states with principal quantum number $n \leq 8$ for the bright and $n \leq 20$ for the dark states and confirm that our results are converged with this choice. Parameters of the states are listed in Table in Appendix A. Assuming the lifetime of all excited states to be defined by the Auger decay of a $4d$ hole, I replace the energy eigenvalues $\tilde{E}_k$ in Eq. (3.19) with $\tilde{E}_k - i\Gamma/2$. Here, $\Gamma = 0.111\,\mathrm{eV}$ is the decay width of a $4d$ hole, corresponding to a lifetime of $\sim 6\,\mathrm{fs}$ [92]. Thus, the state vector $|\tilde{\Psi}, t\rangle$ that underlies the autocorrelation function $C(t, t_0)$ [see Eq. (3.20)] undergoes exponential decay.

As a consequence of its large spectral bandwidth, the attosecond XUV pump pulse can excite the Xe atom from its ground state $J^P = 0^+$ to any of the bright states $J^P = 1^-$, creating a wave packet with a high degree of coherence. We assume the probe laser field not to be strong enough to affect the Xe ground state. However, it can couple a bright state 1^- to a dark state J^+, by exchanging one NIR photon with the atom, or it can couple to another bright state 1^- by exchanging two NIR photons. Since the ground state 0^+ and the dark states J^+ have the same parity, the latter cannot be excited via one-photon absorption from the ground state (i.e., the corresponding transition dipole moments are zero); but in the presence of the dressing laser field, they can give rise to accessible light-induced states (LIS) [83, 84, 85]. The LIS in the absorption spectrum are then interpreted, in the frequency domain, as the intermediate states of processes that involve the absorption or emission of an additional dressing NIR photon.

In Figure 5.3, the computed XUV cross section of Xe without any additional electromagnetic field (red curve) and dressed by a field with a photon energy of $\sim 0.7\,\mathrm{eV}$ and a peak intensity of $\sim 5 \times 10^{10}\,\mathrm{W/cm^2}$ (green curve) are presented. In the absence of a dressing field, the attosecond XUV pulse coherently populates the Xe bright states $4d^9np^1$ ($n \geq 6$). When the

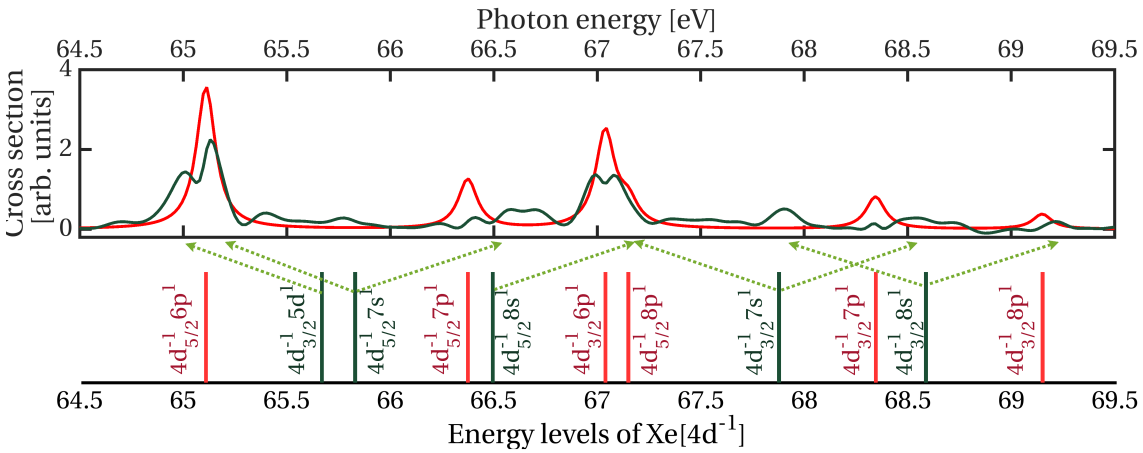

FIGURE 5.3: XUV cross section of Xe (upper panel) in the absence (red) and presence (green) of a dressing field $\omega_{IR} = 0.7$ eV, and energy levels of Xe (lower panel) with one excited $4d$ electron (red: bright states, green: dark states). Arrows designate which dark states correspond to the most important LIS. Adapted from Ref. [69] ©2021 APS .

atom gets dressed by the laser field, transitions to LIS become available. Dipole-allowed LIS can be observed as additional absorption lines. When the bright and dark states are not one-NIR-photon resonant with each other, the LIS energy is one NIR photon away from the dark state. However, when they are in resonance, the result is a so-called Autler-Townes doublet, where the energy is determined by light-induced Rabi splitting [74]. Similarly, in the nonresonant case, there are, in general, AC Stark shifts. In the lower panel of Figure 5.3, the dotted arrows show the parent dark state for the most important LIS. Accessibility of LIS and their corresponding particle-hole wave-packet dynamics depends on the phase properties of the NIR laser field, which provides rich manifolds of dynamics to be explored with time-delayed ATAS.

5.2 Wave-packet dynamics induced by XUV only

From the dependence of the XUV transient-absorption cross section $\sigma(\omega, \tau)$ on the time delay τ between the attosecond XUV and the NIR laser field, one can study the dynamics of inner-shell-excited particle-hole wave packets induced by the XUV pulse (superpositions of odd-parity states only). In the following, I take the Fourier transform of $\sigma(\omega, \tau)$ with respect to τ. Figure 5.4 shows 2D maps of the square root of the resulting XUV one-photon cross section $\sqrt{|\tilde{\sigma}(\omega, \omega')|}$ for photon energies ω that cover the main $4d$-excited states. The square root allows us to make more features visible on the figures presented below. Here

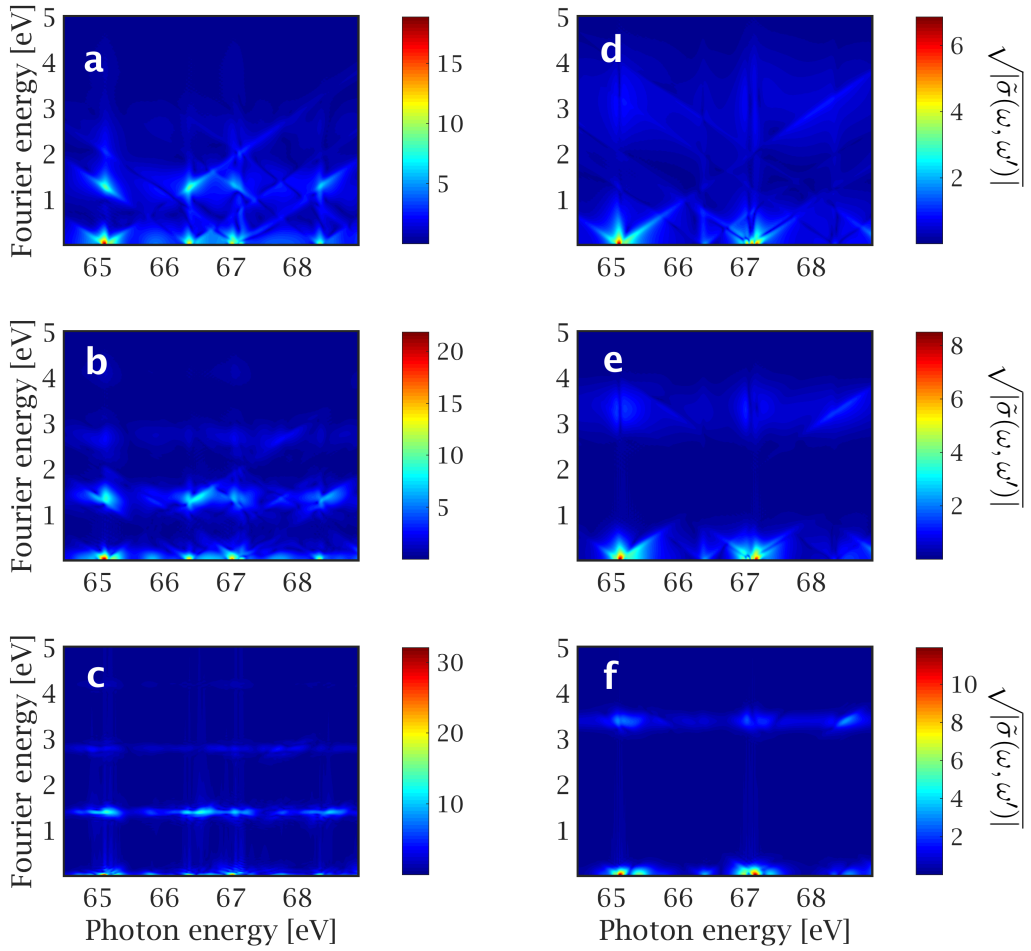

FIGURE 5.4: Square root of the Fourier transform amplitude of the XUV cross section $\sigma(\omega,\tau)$ of Xe ($\sqrt{|\tilde{\sigma}(\omega,\omega')|}$). In (a)-(c) the photon energy of the probe field is $\omega_{IR} = 0.7\,\text{eV}$ and in (d)-(f) $\omega_{IR} = 1.7\,\text{eV}$. The duration of the probe field is one period of the field, T, in (a) and (d), two periods $2T$ in (b) and (e), and $6T$ in (c) and (f). Adapted from Ref. [68] ©2021 APS.

and below ω' is the Fourier energy associated with τ.

As a probe field, I use a Gaussian-shaped NIR field

$$\varepsilon_d(t) = A_{IR}\,\text{Re}\left[e^{-\frac{4\ln(2)}{\chi_{IR}^2}(t-t_0)^2}e^{i\omega_{IR}t}\right], \tag{5.1}$$

with an amplitude of $A_{IR} = 0.0012$ a.u. The central frequency ω_{IR} is chosen as $0.7\,\text{eV}$ for

(a)-(c) and 1.7 eV for (d)-(f), and the pulse duration χ_{IR} is one optical cycle $T = 2\pi/\omega_{IR}$ for (a,d), two times T for (b,e), and six times T for (c,f), where $T = 2.4$ fs for $\omega_{IR} = 1.7$ eV and $T = 6.0$ fs for $\omega_{IR} = 0.7$ eV.

The dynamics of inner-shell-excited particle-hole wave packets induced by the XUV pulse lead to oscillations of the atomic cross section as a function of the time delay. Fourier energies ω' of these oscillations corresponds to the energy differences among the interfering states of the wave packet. This interference appears as "diagonal" features from one odd-parity state to another on the 2D map $\sqrt{|\tilde{\sigma}(\omega,\omega')|}$ in Figs. 5.4 (a,d). The peaks around $\omega' \approx 1.3$ eV correspond to the interference of bright states with the same angular momentum j of the $4d$ hole but different principal quantum number of the Rydberg p electron ($n = 6$ and $n = 7$), i.e., the difference between $4d_{5/2}^{-1}6p^1$ and $4d_{5/2}^{-1}7p^1$ ($66.375 - 65.110 = 1.265$ eV) and between $4d_{3/2}^{-1}6p^1$ and $4d_{3/2}^{-1}7p^1$ ($68.345 - 67.039 = 1.306$ eV). On the other hand, the peaks around $\omega' \approx 2$ eV result from the interference of bright states with different angular momentum j of the $4d$ hole but the same n of the excited p electron (for example, 1.929 eV for $n = 6$ and 1.970 eV for $n = 7$). The latter peaks are strongly suppressed relative to the former peaks due to weak coupling between states with different angular momentum j of the $4d$ hole. Due to dipole selection rules, transition from one odd-parity state to another requires an even number of photons. Therefore, the resonances $\omega' \approx 1.3$ eV and $\omega' \approx 2$ eV are more pronounced in Figure 5.4 (a), where the photon energy is $\omega_{IR} = 0.7$ eV, than in Figure 5.4 (d) ($\omega_{IR} = 1.7$ eV), as $2\omega_{IR}$ is closer to those resonances.

The strong peaks around $\omega' \approx 3.4$ eV in Figs. 5.4 (d-f) rather appear as a "horizontal" feature. Although one can see in Figure 5.4 (d) the "diagonals" between the states $4d_{5/2}^{-1}6p^1$ ($\omega = 65.110$ eV) and $4d_{3/2}^{-1}7p^1$ ($\omega = 68.345$ eV), for the state $4d_{3/2}^{-1}6p^1$ ($\omega = 67.039$ eV) there is no such diagonal, because there is no coupled bright state at $2\omega_{IR}$ away (i.e., neither at 64 eV nor at 70 eV is there a coupling partner included in the simulation). However, its cross section also reveals fairly strong $\omega' \approx 3.4$ eV oscillations with the time delay. The reason is the following. When the duration of the probe pulse becomes longer than the lifetime of the $4d$-excited state, the observation of the inner-shell-excited particle-hole wave packet dynamics induced by the XUV becomes more difficult. The laser field creates active valence-electron dynamics throughout its duration, which strongly affects the atomic cross section for all absorption peaks. Accessibility of those states directly depends on the laser field potential, which leads to the "horizontal" features on the 2D map of $\sqrt{|\tilde{\sigma}(\omega,\omega')|}$ in Figs. 5.4 (c,f). The dominant frequency of the cross section oscillations as a function of the time delay between the XUV and NIR pulses becomes $\omega' = 2n\omega_{IR}$ ($n = 1, 2, ...$). Thus, the horizontal features are around $\omega' \approx 1.4$ eV in Figure 5.4 (c) and $\omega' \approx 3.4$ eV in Figure 5.4 (f). This tendency already appears for the pulse duration of $2T$ in Figure 5.4 (b,e). These horizontal 2ω structures

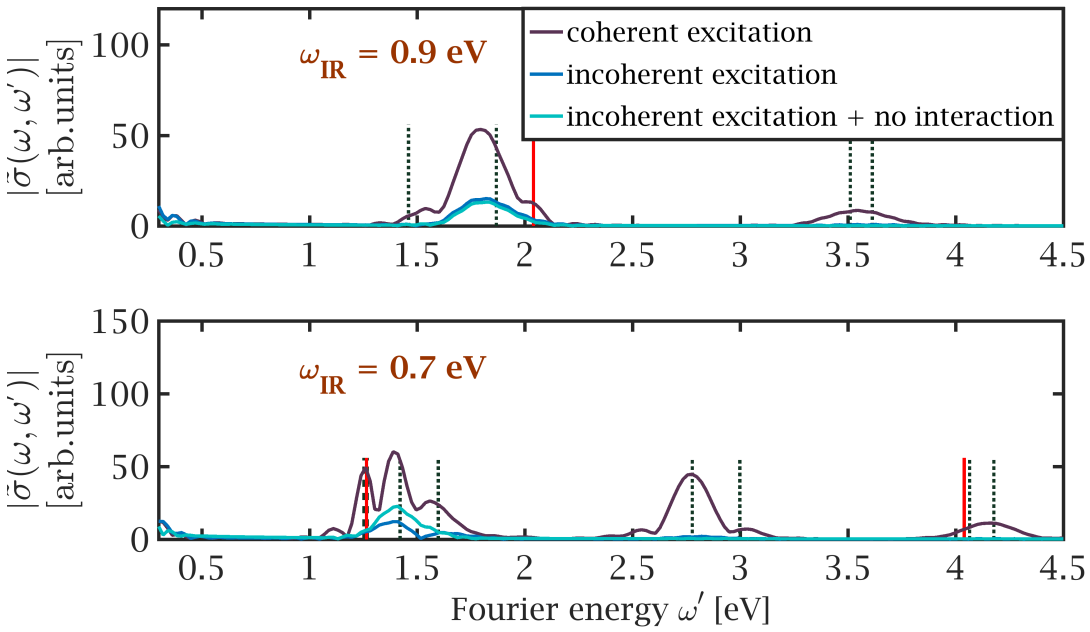

FIGURE 5.5: Fourier-transformed XUV cross section $|\tilde{\sigma}(\omega,\omega')|$ for the $4d_{5/2}^{-1}6p^1$ state of Xe at $\omega = 65.1$ eV. The duration of the laser pulse is $4T$ and the photon energy ω_{IR} is 0.9 eV (upper panel) and 0.7 eV (lower panel). Red vertical lines are used to mark bright-state–bright-state resonances and black dashed lines for LIS–bright-state resonances. Adapted from Ref. [68] ©2021 APS.

become broader with shorter pulses due to the larger Fourier bandwidth.

In Figure 5.5, the Fourier spectrum of the main absorption peak $4d_{5/2}^{-1}6p^1$ ($\omega \approx 65.1$ eV) is presented for a probe-pulse duration of $4T$. The upper panel corresponds to $\omega_{IR} = 0.9$ eV and the lower one to $\omega_{IR} = 0.7$ eV. These energies ω_{IR} of the laser field were chosen in order to create more interesting wave packet dynamics and to be able to observe more resonances $\omega' \approx 2n\omega_{IR}$ ($n = 1, 2, ...$). Different colors are used for three different cases: (i) coherent excitation; (ii) "incoherent" excitation, where only the $4d_{5/2}^{-1}6p^1$ state is allowed to be excited by the XUV field; and (iii) only $4d_{5/2}^{-1}6p^1$ is allowed to be excited by the XUV and no interactions are allowed between the bright states through the dark states. Relatively short probe-pulse durations provide an energy spectrum that is sufficiently broad to observe inner-shell-excited wave packet dynamics induced by the XUV. The red vertical lines mark the bright–bright resonance positions for the $4d_{5/2}^{-1}6p^1$ state. The black dotted lines represent the bright-state–LIS transitions. Although the bright–LIS interference peak at $\omega' = 2\omega_{IR}$ is dominant for both values of ω_{IR}, the bright–bright interference peaks at

$\omega' = 2\,\text{eV}$ (upper panel) and $\omega' = 1.3\,\text{eV}$ (lower panel) can still be seen under coherent excitation. For incoherent excitation, those bright–bright interference peaks are absent.

The main challenge with detecting the inner-shell hole dynamics is that their impact on the NIR-modulated XUV cross section is much weaker than the impact of the Rydberg-electron dynamics induced by the probe field. By reducing the duration of the NIR laser field one can decrease the effect of the latter dynamics, but it will also increase the width of the interference peaks in the Fourier spectrum. In order to observe inner-shell hole dynamics, the optimal laser pulse duration is comparable with the lifetime of the excited state ($\chi_{IR} \approx 1/\Gamma$). Also the NIR photon energy needs to be close to the resonance $\omega_{IR} = |E_1^- - E_2^-|/2$, where E_1^- and E_2^- are the energies of two bright states with different inner-shell holes (but the same state for the Rydberg electron). Another important requirement for observing inner-shell hole dynamics is sufficiently large dipole moments between the E_1^- / E_2^- states and a dark state E_i^+ that can couple them.

5.3 Wave-packet dynamics induced by XUV in the presence of a dressing field

In this section, I study the situation when the XUV pulse overlaps with a dressing NIR field that is a weak copy of the probe NIR field (i.e., the dressing field is to be carefully distinguished from the probe field). Being in temporal overlap with the XUV pulse, the NIR dressing field enables us to investigate the coherent coupling and wave-packet dynamics between both odd-parity and even-parity inner-shell excited states [93, 65]. The intensity of such dressing NIR field usually reaches 1-5% of the delayed probe NIR field, which is sufficient to induce significant couplings, as demonstrated in the following.

In Figure 5.6 I investigate the dependence of the absorption peak oscillations on the strength of the probe A_{IR} and dressing A_d pulses. Here $\omega_{IR} = 1\,\text{eV}$ is used. Oscillation at $\omega' = 2\omega_{IR}$ reveals the processes that involve the absorption of two laser photons, such as interference between two one-time dressed states, or between the original state and the double-dressed state. The cross section of these two-photon processes is proportional to the product of the strength of the fields, which causes the dressing. For the process where the dressing is caused by the probe field only, the cross section is $\tilde{\sigma}(\omega, \omega' = 2\omega_{IR}) \propto A_{IR}^2$, and for the process involving both probe and dressing fields, it gives $\tilde{\sigma}(\omega, \omega' = 2\omega_{IR}) \propto A_{IR}A_d$. Oscillations at $\omega' = \omega_{IR}$ appear only in the presence of the dressing field, because it creates coherence between odd-parity and even-parity atomic eigenstates. They reflect processes in which three laser photons are involved, one of them being a dressing-field photon. Thus, to

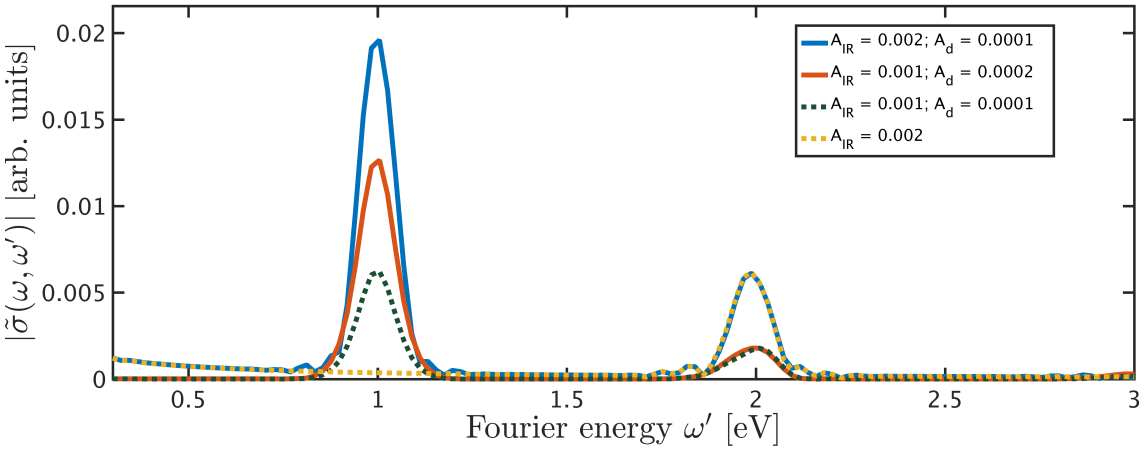

FIGURE 5.6: Fourier-transformed XUV cross section $|\tilde{\sigma}(\omega,\omega')|$ of Xe at $\omega = 65.1$ eV in the presence of a dressing field for different strengths of the probe (A_{IR}) and dressing (A_d) fields ($\omega_{IR} = 1$ eV).

leading order in A_d, $\tilde{\sigma}(\omega,\omega' = \omega_{IR})$ is proportional to $A_d A_{IR}^2$. These scalings are confirmed by Figure 5.6.

Figure 5.7 shows the square root of the Fourier-transformed ATAS of Xe for a dressing field with an amplitude of $A_d = 0.2A_{IR}$. Note that 20% of the amplitude corresponds to 4% of the intensity. For the short pulses in Figs. 5.7 (a,d) the "diagonal" features, corresponding to the dynamics inside the wave packet, are created by the XUV pulse in presence of the dressing NIR field. Originally the present dressing field provides a coupling with one photon ω_{IR} between the bright and dark states, such as bright state $4d_{3/2}^{-1}6p^1$ ($4d_{5/2}^{-1}6p^1$) and dark state $4d_{3/2}^{-1}6s^1$ ($4d_{5/2}^{-1}6s^1$). Although the intensity of the dressing field is weak, it leads to a very strong coupling in the case of $\omega_{IR} = 1.7$ eV. For example, the diagonal features around 1.3 eV in Figure 5.7 (d) are more prominent than those in Figure 5.4 (d). For the long pulses in Figs. 5.7 (c,f), the "horizontal" features emerge around 1.4 eV and 2.1 eV in (c), and 1.7 and 3.4 eV in (f), respectively, which correspond to $\omega' = n\omega_{IR}$ ($n = 1, 2, 3, ...$).

To analyze these oscillations in more detail I present in Figure 5.8 the Fourier-transformed ATAS at the main absorption peak $4d_{5/2}^{-1}6p^1$ in the presence of the dressing field. The photon energy ω_{IR} and pulse duration are the same as used in Figure 5.5. In contrast to Figure 5.5, the resonances between bright states and dark states are visible (black solid lines), which are caused by the coherence between odd-parity and even-parity atomic eigenstates. The strongest oscillations have Fourier energies $\omega' = n\omega_{IR}$ ($n = 1, 2, 3...$) for both photon energies shown. The strength of these oscillations depends on whether harmonics of ω_{IR} are energetically close enough to drive an interference between two excitation paths, as well as

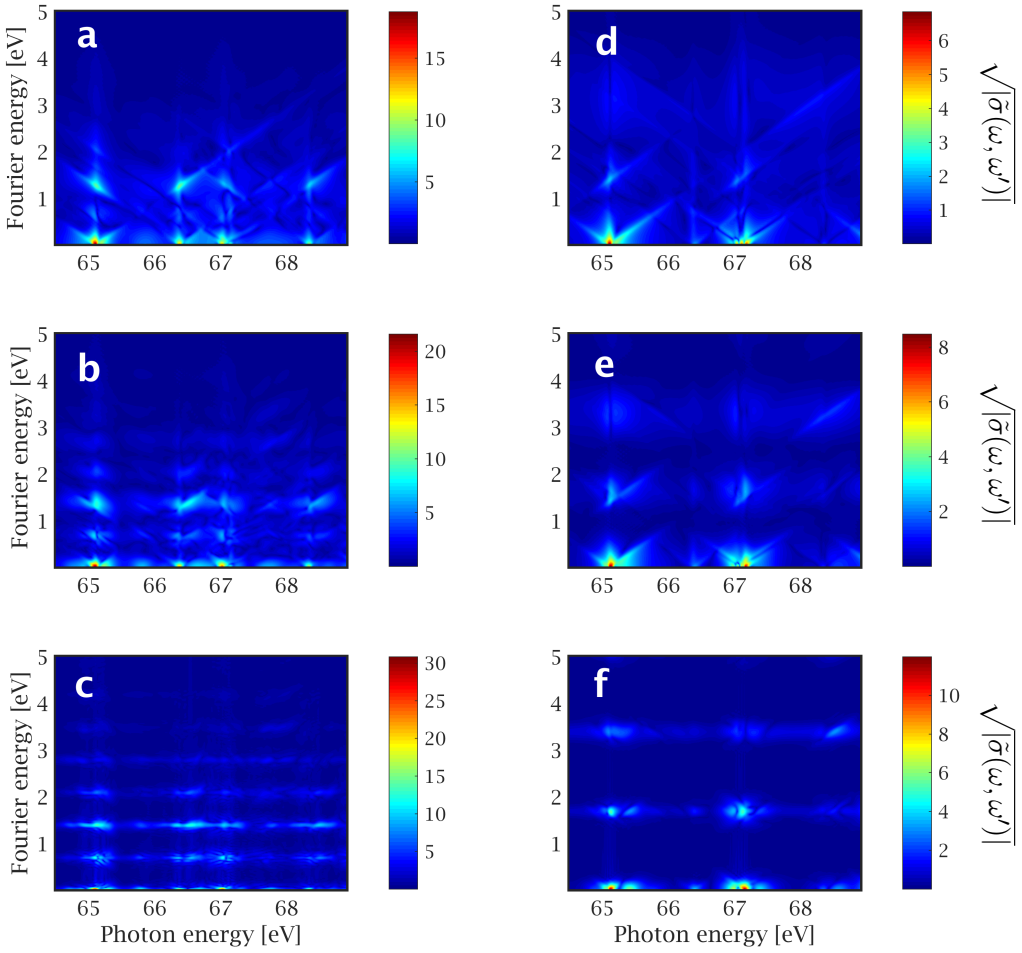

FIGURE 5.7: Square root of the Fourier transform amplitude of the XUV cross section of Xe ($\sqrt{|\tilde{\sigma}(\omega,\omega')|}$) in the presence of a dressing field. In (a)-(c) the photon energy of the probe field is $\omega_{IR} = 0.7\,\text{eV}$ and in (d)-(f) $\omega_{IR} = 1.7\,\text{eV}$. The duration of the probe field is one period of the field, T, in (a) and (d), two periods $2T$ in (b) and (e), and $6T$ in (c) and (f). Adapted from Ref. [68] ©2021 APS.

on the strength of the dipole moments of the states involved in the interaction.

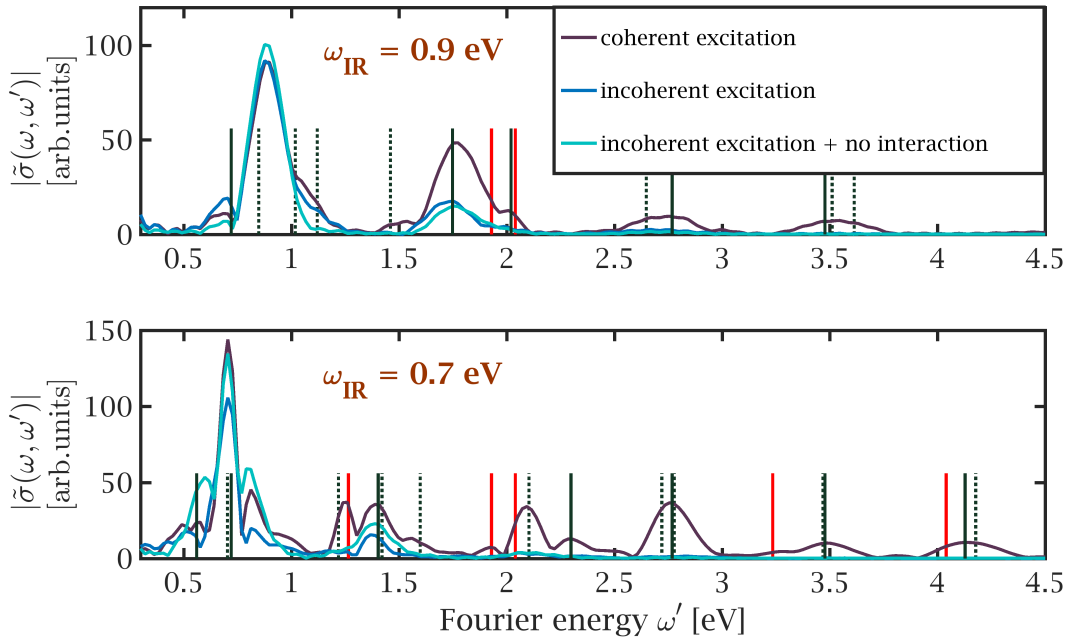

FIGURE 5.8: Fourier-transformed XUV cross section in the presence of a dressing field with amplitude $A_d = 0.2A_{IR}$ for the $4d_{5/2}^{-1}6p^1$ state with $\omega = 65.1\,\text{eV}$ fixed. The duration of the laser pulses is $4T$ and the photon energy ω_{IR} is $0.9\,\text{eV}$ (upper panel) and $0.7\,\text{eV}$ (lower panel). Red solid lines mark bright–bright resonances, black solid lines mark bright–dark resonances, and black dashed lines indicate LIS–bright resonances. Adapted from Ref. [68] ©2021 APS.

5.4 Comparison with experiment

In the experiment, a helium-filled, differentially-pumped hollow-core fiber (Femtolasers Kaleidoscope) and chirped mirrors (PC70, Ultrafast Innovations) were used to generate almost octave-spanning NIR pulses at a central photon energy of $\omega_{IR} = 1.6\,\text{eV}$ and 1-mJ pulse energy from a commercial Ti:sapphire laser system (Femtolasers HE/HR). The pulses are characterized using the DScan technique [94, 95], which reveals a pulse-intensity duration of $4.3\,\text{fs}$. The coherent XUV light is produced from HHG in neon driven by the NIR pulses and has a continuous spectrum over the range of 40-$70\,\text{eV}$ photon energy. The NIR and XUV pulses co-propagate, and an aperture controls the NIR power without affecting the central XUV beam. Using a piezo-driven split-mirror, which is combined with a spatial filter unit, a time delay of sub-30 attosecond stability was introduced between the NIR and XUV pulses. Afterwards, both beams are reflected off a toroidal mirror, which refocuses

the beams into the target gas cell, after which an XUV spectrometer is used to measure the spectrum of the transmitted XUV light with 45 meV resolution [96]. The thin-foil aluminum filters used in the spatial filter unit to block the NIR light are known to contain micro-holes that allow a small fraction of the NIR pulse to pass. This leakage is temporally locked to the XUV radiation and constitutes a weak replica of the main NIR pulse with typically a few percent of its power, realizing the dressing-pulse geometry as described in Section 5.3.

When the XUV pulse interacts with the xenon atom at photon energies above $65\,\mathrm{eV}$, electronic transitions from the $4d$ core shell to unoccupied np levels ($n \geq 6$) are triggered (note that transitions to nf levels are suppressed in Xe [97]). For each principal quantum number n, a fine-structure doublet of absorption lines is created due to spin-orbit interaction [98] of the hole. Here, the focus was on the absorption lines at $65.11\,\mathrm{eV}$ and $67.04\,\mathrm{eV}$ for the case of $n = 6$, because these are the strongest transitions of the series. These core-excited states decay rapidly via the Auger process leading to lifetimes of less than $6.5\,\mathrm{fs}$, which corresponds to natural line widths of approximately $0.1\,\mathrm{eV}$, respectively, with the natural line shape, to a good approximation, being described by a Lorentzian profile [98, 92]. Compared to the $1.31\,\mathrm{eV}$ splitting of the Xe^+ $5p$ hole states that have also been encountered in previous experiments [26, 99, 100], the spin-orbit splitting of these core-excited states is substantially stronger and amounts to $1.93\,\mathrm{eV}$ (for $n \to \infty$, the energy splitting converges to $1.97\,\mathrm{eV}$ [98]). Note that the above absorption lines correspond to the energies used in our calculation as listed in Table A.1 ($4d_{5/2}^{-1}6p^1$ and $4d_{3/2}^{-1}6p^1$).

Figure 5.9 presents a comparison of the experimental and simulated Fourier-transformed XUV cross sections as a function of ω and ω'. In simulation 1 (Fig. 5.9), the laser pulse $\varepsilon(t)$ measured experimentally in front of the HHG gas cell was employed. Although the simulated spectrum reproduces most of the features of the experimental spectrum, some of them are missing. The second stronger oscillation of the main peaks of the experimental spectrum has a Fourier energy $\omega' = 2\,\mathrm{eV}$. It is absent in the simulated spectrum 1. It can be seen more clearly in the Fig. 5.10, where a slice of the XUV cross section at $\omega = 65.1\,\mathrm{eV}$ in the ω' and τ domains is presented. In simulation 2 (Fig. 5.9)a modified pulse with a much stronger 2-eV energy component is used. It allows to achieve a better agreement with the experimentally observed spectra.

A comparison of the pulse shapes (Fig. 5.11) and a description of how to construct the pulse shape is presented at the end of this section. The intensity of the probe field defines the depth of the cross section $\sigma(\omega, \tau)$ attenuation (in the lower panel of Figure 5.10), and the intensities of the probe and dressing fields together determine the strength of oscillations with the time delay τ. Guided by this correlation, the strength of the probe field was chosen

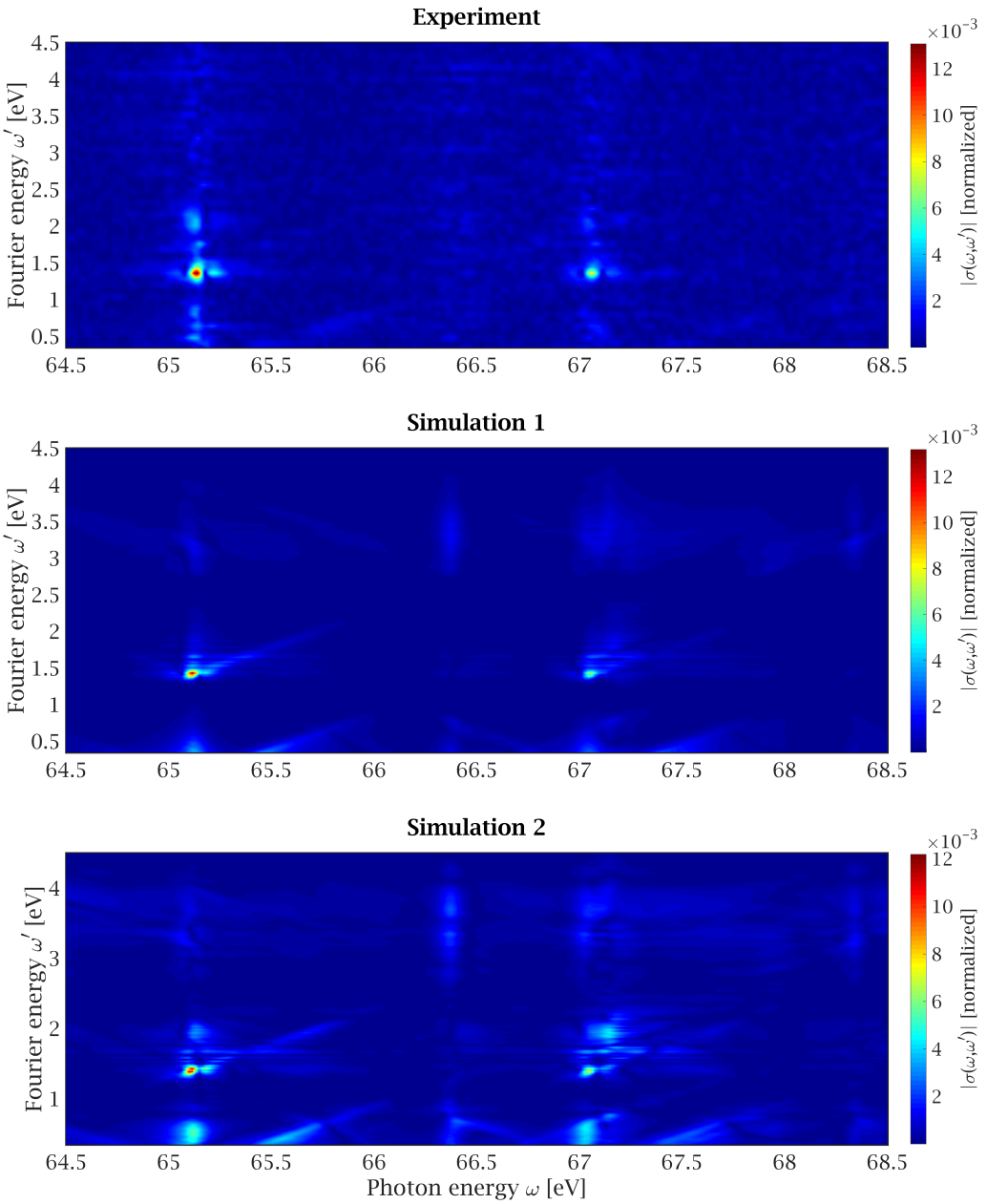

FIGURE 5.9: Square root of experimental and simulated XUV spectra $|\tilde{\sigma}(\omega, \omega')|$. In simulation 1, the nominal pulse shape from experiment is used. In simulation 2, a modified pulse shape is used as described in the text.

as $A_{IR} = 0.0009$ a.u. and 0.0012 a.u. for simulations 1 and 2, respectively. The intensity of the dressing pulse is 5% of the intensity of the probe laser field in both cases.

The diagonal streaks in the experimental panel are reproduced in both simulation panels.

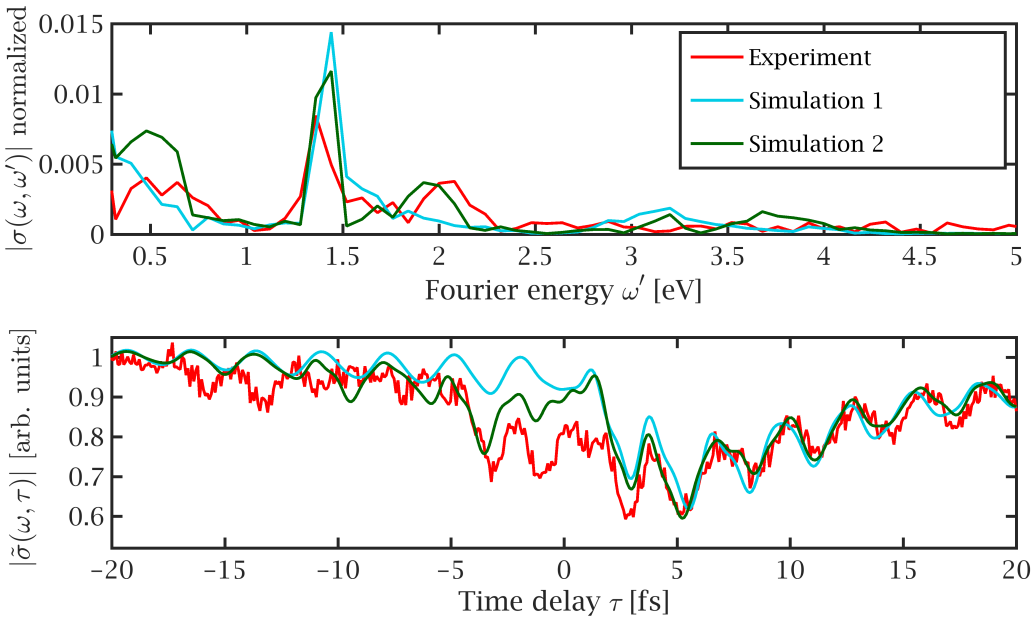

FIGURE 5.10: Experimental and simulated XUV cross sections at $\omega = 65.1\,\text{eV}$ in the Fourier energy and time delay domains. Adapted from Ref. [68] ©2021 APS.

All three panels in Figure 5.9 show pronounced $4d_{5/2}^{-1}6p^1$ ($\omega = 65.110\,\text{eV}$) and $4d_{3/2}^{-1}6p^1$ ($\omega = 67.039\,\text{eV}$) peaks at $\omega' \approx 1.4\,\text{eV}$. The associated time-domain dynamics are a consequence of dressing-field-mediated coupling between the $6p$ and $6s$ Rydberg-electron states. Without the dressing field, the $1.4\,\text{eV}$ beating disappears.

Looking at the τ dependence of the XUV cross section in Figure 5.10, one can see that the discrepancy between simulation 1 and experiment appears near $\tau = 0$ and at negative delay, i.e., when the XUV pulse overlaps with or comes after the NIR pulse. When the XUV pulse comes first ($\tau > 0$), both simulations are in good agreement with experiment. The discrepancies at negative τ might be an indication that the NIR field interacting with the Xe atoms differs from the NIR field characterized in front of the HHG gas cell. This could be caused by laser field interaction with the optics or plasma in the HHG gas cell. Field Ionizing Media (FIM) are known to be able to add a chirp to the trailing part of a laser pulse [101]. Owing to the phase modulation induced by plasmas in FIM, the laser frequency increases with time (positive chirp) at the leading edge, and then decreases (negative chirp) back to the original frequency in the remaining part of the pulse [102]. Guided by this, the chirp effect was applied to the experimentally measured spectral amplitude $A(\omega)$ and

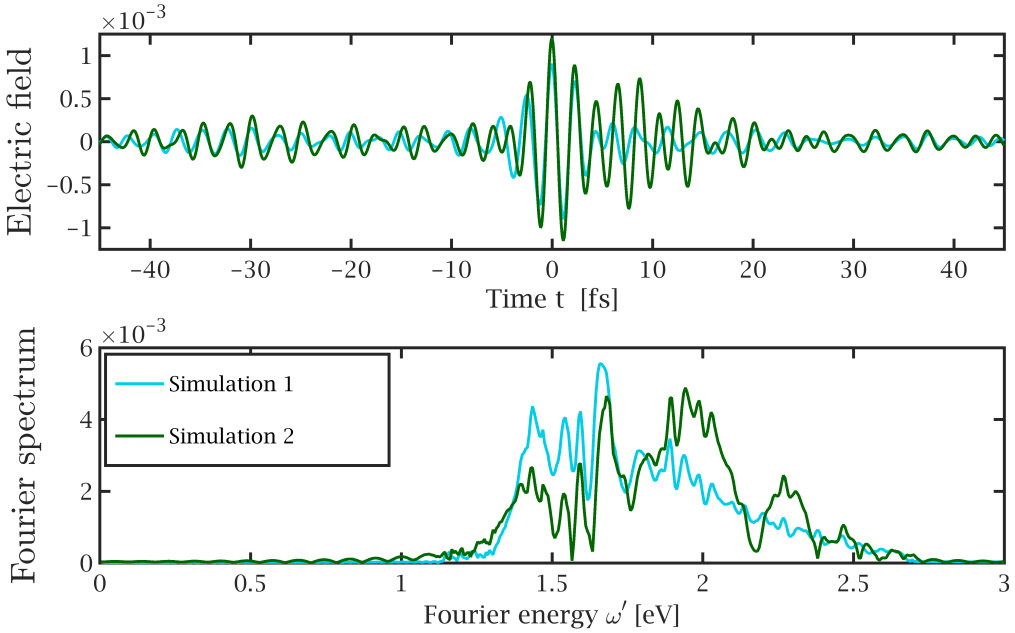

FIGURE 5.11: Pulses used in simulations 1 and 2, in the Fourier energy and time domains. Adapted from Ref. [68] ©2021 APS.

spectral phase $\phi(\omega)$,

$$\varepsilon_{ch}^{\pm}(\omega) = A(\omega)e^{-i\phi(\omega)} \exp\{\pm ia\omega^2\}. \tag{5.2}$$

Then, I add together their inverse Fourier transforms $\varepsilon_{ch}^{\pm}(t)$, applying the switching function $f(t) = \frac{1}{2}\left\{1 + \frac{2}{\pi}\arctan\left(\frac{t-b}{c}\right)\right\}$,

$$E_{ch}(t) = f(t)\varepsilon_{ch}^{-}(t) + \{1 - f(t)\}\,\varepsilon_{ch}^{+}(t). \tag{5.3}$$

Here a, b, and c are free parameters. The magnitude of the FIM-induced chirp depends on the properties of the HHG gas cell, including the percentage of ionization of the HHG target gas. If this phenomenon leads to an enhancement of the pulse spectrum in the vicinity of 2 eV, laser-mediated coupling to $4d^{-1}ns^1$ ($n > 10$) and $4d^{-1}nd^1$ ($n \geq 8$) Rydberg states will be activated. In the simulation 2 parameters $a = 15\,\text{fs}^2$, $b = 0\,\text{fs}$, and $c = 0.8\,\text{fs}$ are employed. This choice gives improved agreement with the experimental results and is consistent with Refs. [103, 104], where a dynamic blue shift from a carrier wavelength of 750 nm (1.65 eV) to some 550 nm (2.25 eV) was observed in HHG in Ne. Even though our guess regarding the pulse-phase modifications in the HHG gas cell does not provide perfect agreement with experiment for the XUV cross section in the negative delay domain ($\tau < 0$), it reproduces the main features of the XUV cross section and gives fairly good agreement in the Fourier

energy domain (Figures 5.9 and 5.10). This makes it plausible that the FIM-induced chirp effect may have affected the experimental data.

5.5 Conclusion

I demonstrated that various aspects of coherent electron dynamics can be revealed when wave packets prepared by an attosecond pump pulse are probed using an NIR pulse. It is shown that inner-shell hole dynamics are much more difficult to detect than Rydberg-electron dynamics, because the dynamics of the inner-shell hole are defined mostly by the degree of coherence of the wave packet initially created by the XUV pulse, whereas Rydberg electrons get strongly dressed by the NIR pulse, thereby producing strong quantum coherence effects that are reflected in the ATAS. Typically, the transition dipole moment between states with different angular momentum j of the hole is much weaker than for states with the same j. This makes the evolution of wave-packet components with different hole j mostly independent from each other and, thus, not so sensitive to the presence of the probe field. For this reason, the ATA Xe spectrum calculated using the XCID code (Figure 5.2) shows the same interference pattern as the ATA spectrum calculated taking into account a mixture of configurations with different aperture angular momenta j. The presented analysis suggests that, in order to detect inner-shell hole dynamics using an NIR probe field, it is necessary to minimize the effect of the laser field on the Rydberg levels, which can be done by decreasing the field exposure time and by using fields that are far off resonance.

I show that the presence of a dressing field or a slight modification of the spectrum of the probe pulse can dramatically change the simulated ATAS results. Thus, our work also suggests that a precise NIR pulse characterization in the target region behind the HHG gas cell is necessary for a qualitatively and quantitatively accurate interpretation of experimental ATAS data, due to the high sensitivity of Rydberg electrons to the NIR electric fields.

Part II

Pulse characterization using machine learning approach

Chapter 6

Multiphoton autocorrelation in Ar

In this chapter we explore the multiphoton autocorrelation in Ar atom in order to be able to use it for the characterization of laser pulse. We use the XCID code for numerical simulations of Ar ionization by the autocorrelated laser field, i.e., two identical time-delayed copies of the same pulse. The ionization probability depends on the parameters of the ionizing laser field, such as photon energy, pulse intensity and duration. These parameters are known for each time delay for the autocorrelated laser field. I investigate a simple approximation function, which provides a flexibility in time-delay resolution of ionization probability functions. The results of this chapter are later used in Chapter 7 to develop a machine-learning-based technique for laser pulse characterizations.

6.1 Experimental setup

In my simulations I consider the laser field autocorrelation obtained by splitting the initial laser pulse $E_0(t)$ in two identical copies and further recombination after inserting a certain time-delay τ. In Fig. 6.1 a scheme of the simplest experimental setup for this purpose is presented. The initial beam $E_0(t)$ is characterized by frequency-resolved optical gating method (FROG) after being processed and focused. This beam is split by the beamsplitter (BS1) into two beams $E_1(t)$ and $E_2(t)$. One of them gets delayed by the system of mounting mirrors $E_2(t) \Rightarrow E_2(t+\tau)$. For the recombination after the delay stage a beamsplitter (BS2) is used, instead of a drilled mirror, because it allows to provide the same intensity for each arm on a target. If the beamsplitters BS1 and BS2 have the same thickness, they have exactly the same properties and cause the same dispersion changes in the two arms. This way both arms provide almost identical pulses. However the phase of each pulse changes randomly via different number of bounces of mirror and it's not the same in the two arms. After

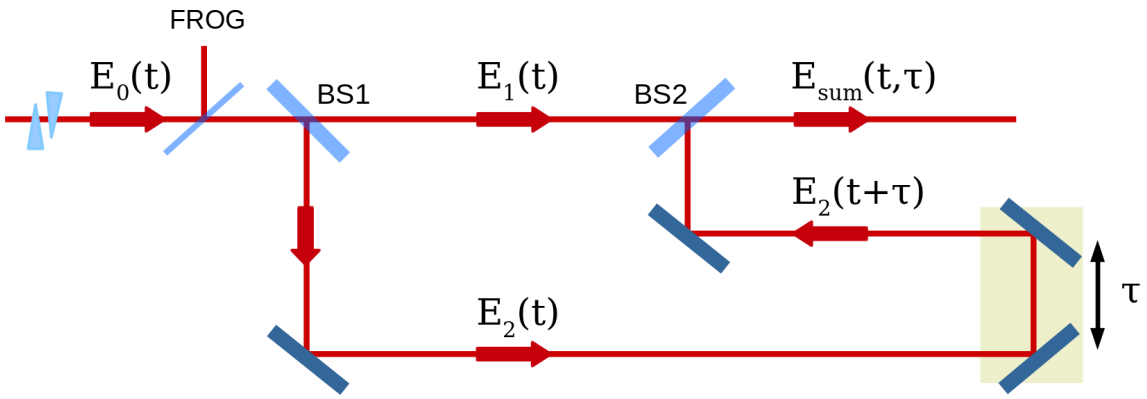

FIGURE 6.1: Experimental setup. BS1 and BS2 are the beamsplitters, FROG is a Frequency-resolved optical gating device.

recombination we obtain the new pulse

$$E_{sum}(t,\tau) = E_1(t) + E_2(t+\tau). \tag{6.1}$$

While traveling through the mirrors and lenses, which are required for the pulse focusing, the pulse can get some unintended modifications. The most common among them is a so-called chirp — a signal in which the frequency increases (up-chirp) or decreases (down-chirp) with time. Chirp is usually expressed in the spectral domain through the range group delay dispersion (GDD), and in this work one expects GDD $= 0$–$20\,\text{fs}^2$. For the broadband pulses, such a range dramatically affects the pulse duration. For example, if we assume a transform-limited (no chirp) duration of $5\,\text{fs}$, a chirp of GDD $= 20\,\text{fs}^2$ increases the pulse duration up to $10 - 12\,\text{fs}$ and the autocorrelation would be much longer. In Figure 6.2 one can see an illustration how the chirp characterized by GDD $\approx 20\,\text{fs}^2$ changes a pulse duration from initial $\chi_t = 200\,\text{a.u.}$ $(4.84\,\text{fs})$ to $\chi_t = 450\,\text{a.u.}$ $(10.89\,\text{fs})$ keeping the spectrum unchanged at the same time. In this work, I assume the experimental setup to be perfect to ensure both pulse and its replica to have the same chirp.

In this work I apply aforementioned approach to characterize a laser pulse with a central photon energy $\omega \approx 1.65\,\text{eV}$ (central wavelength $\lambda \approx 750\,\text{nm}$). In the multiphoton ionization regime, a pulse with an intensity $I = E_{sum}^2$ that satisfies the Keldysh parameter is considered. The duration of the pulse of the $E_0(t)$ is expected to be $5 - 7\,\text{fs}$ transform limited.

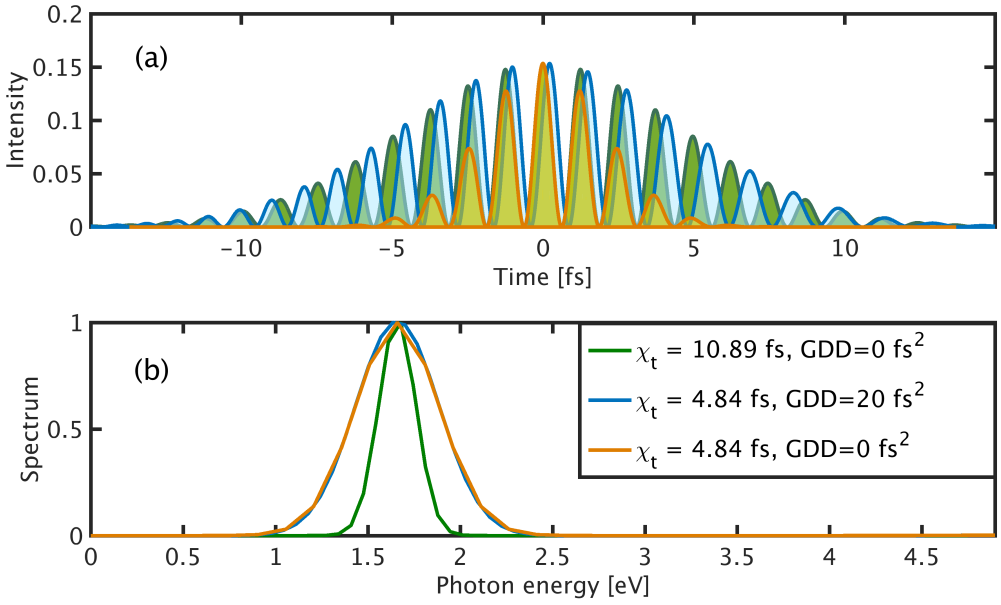

FIGURE 6.2: Comparison of a chirped and not-chirped electric field of a time duration $\chi_t = 4.84$ fs and $\chi_t = 10.89$ fs (a) in a time domain and (b) frequency domain.

6.2 Theoretical background

Theoretical modeling of the atom interaction with a laser field requires the representation of the field in a time domain. Here we derive an expression for a chirped Gaussian pulse in the time domain. In frequency domain the chirp k is usually introduced in electric field as

$$\begin{aligned} E(\omega) &= \exp\left[-\frac{4\log(2)(\omega-\omega_0)^2}{\chi_\omega^2} + ik(\omega-\omega_0)^2 + i\varphi \right] \\ &= \exp\left[-k_0(\omega-\omega_0)^2 + i\varphi \right], \end{aligned} \tag{6.2}$$

where ω_0 is a central frequency of the field, χ_ω is a FWHM of the field spectrum. By introducing parameter k_0,

$$k_0 = \frac{4\log(2)}{\chi_\omega^2} - ik = \frac{\chi_t^2}{16\log(2)} - ik, \tag{6.3}$$

one can see in Eq. 6.2, how the chirp k leads to an increased pulse duration.

Being a complex number, k_0 can be expressed in an exponential representation as

$$k_0 = |k_0|e^{i\alpha_0} = |k_0|\cos\alpha_0 + i|k_0|\sin\alpha_0. \tag{6.4}$$

In such a way one can write an electric field in the time domain as

$$\begin{aligned}\tilde{E}(t) =&\frac{1}{2\pi}\int_{-\infty}^{\infty} E(\omega)e^{-i\omega t}d\omega \\ =&\frac{1}{2\pi}\sqrt{\frac{\pi}{k_0}}e^{\frac{(it)^2}{4k_0}}e^{-i(\omega_0 t+i\varphi_0)} \\ =&\frac{1}{2\sqrt{\pi|k_0|}}e^{-\frac{t^2}{4|k_0|}\cos\alpha_0}e^{-i(\omega_0 t-\varphi_0+\frac{\alpha_0}{2}-\frac{t^2}{4|k_0|}\sin\alpha_0)}.\end{aligned} \tag{6.5}$$

The real electric field in the time domain reads

$$\begin{aligned}E(t) =&\mathrm{Re}\Big[\tilde{E}(t)\Big] \\ =&\frac{1}{2\sqrt{\pi|k_0|}}e^{-\frac{t^2}{4|k_0|}\cos\alpha_0}\cos\Big(\omega_0 t-\varphi_0+\frac{\alpha_0}{2}-\frac{t^2}{4|k_0|}\sin\alpha_0\Big) \\ =&\frac{1}{2\sqrt{\pi|k_0|}}e^{-at^2}\cos\Big(\omega_0 t-\varphi-bt^2\Big),\end{aligned} \tag{6.6}$$

where $a=\frac{\cos\alpha_0}{4|k_0|}$ and $b=\frac{\sin\alpha_0}{4|k_0|}$. The actual time duration X of the chirp-modified pulse, i.e., the FWHM of its envelope, can be found with the following formula:

$$X^2=\frac{2\log(2)4|k_0|^2}{\mathrm{Re}[k_0]}=\frac{\chi_t^4+8^2\log(2)^2k^2}{\chi_t^2}; \tag{6.7}$$

6.3 Numerical parameters of XCID

Using the TDCIS package of XCID code, we performed calculations on an argon (Ar) atom. The electronic configuration for Ar is [Ne]$3s^2 3p^6$. In our calculations, we only allow the $3p$ and $3s$ orbitals to be active, whereas all other orbitals are frozen (not affected by the laser field). The laser field amplitude in our calculations is $E_0 = 0.015$ a.u. and its frequency $\omega = 0.061$ a.u. Classically, an ionized electron that can recollide with its parent ion can travel $r \approx E_0/\omega^2 = 4$ a.u. before recollision. Therefore, to perform a precise and stable calculation we chose the edge of the grid at $r_{max} = 80$ a.u. and a grid size of $N = 300$ grid points. In numerical calculations when the wave packet reaches the end of the numerical grid, artificial reflections arise, which lead to unphysical results. They can be suppressed by applying a complex absorbing potential (CAP) [105, 106, 107, 108, 109, 110] near the end of

the grid. Thus, the single-electron part of the Hamiltonian

$$\hat{H}_0 = \hat{F} - i\zeta\hat{W}, \tag{6.8}$$

is the sum of the time-independent Fock operator $\hat{F}$ and a complex absorbing potential CAP

$$W(r) = \theta(r - r_{abs})(r - r_{abs})^2, \tag{6.9}$$

where $\theta(r)$ is the Heaviside step function, and r is the distance from the origin. This CAP is zero until the absorption radius r_{abs}, after which it is a quadratically growing potential. The CAP strength ζ has to be chosen carefully to avoid reflections from the grid wall r_{max} or the CAP [105, 110]. In our calculations $\zeta = 0.5$. In order to eliminate any CAP-induced perturbation of recolliding trajectories, we have put our absorbing potential at $r_{abs} = 50$ a.u. The maximum angular-momentum value allowed in our calculations for the dipole is $l_{max} = 10$ and the orbitals with Hartree-Fock energies higher than 20 a.u. (real part of the orbital energies) were determined to not contribute significantly and have been omitted from the propagation calculations

6.4 Analysis of multiphoton autocorrelation of Ar

In this section, I analyze delay patterns of multiphoton autocorrelation of an Ar calculated with TDCIS and explore the dependence of the ionization probability $P(\tau)$ on pulse parameters. Using the representation of the $E(t)$ described above [Eq. (6.6)], I have added a new option of the chirped pulse to the TDCIS code, and calculated the ionization probability of Ar atom exposed to a pair of identical laser pulses $E_1(t)$ and $E_2(t + \tau)$ delayed relative to each other. Pulse $E_1(t)$ differs from $E_2(t)$ only through the phase value ϕ. The calculations were performed using a large set of pulse parameters: the FWHM of the pulse intensity was considered in the range $200 \leq \chi_t \leq 550$ a.u., the phase ϕ of each pulse replica can vary from 0 to 2π, and the chirp k can take values in the range $0 \leq k \leq 15000$ a.u. For each set of parameters the calculations were done for 51 time-delay points τ.

For any set of pulse parameters and any time-delay point τ, the ionization probability $P(\tau)$ depends on a phase difference $\Delta\phi = \phi_1 - \phi_2$, but not on a specific combination of ϕ_1 and ϕ_2. Besides, the ionization probability for the negative phase shift $P(\tau, -\Delta\phi)$ is exactly the same as the positive phase shift but inverted in time $P(-\tau, \Delta\phi)$, which is illustrated in Figure 6.3 on the example of the relative phase shift $\Delta\phi = \pi/4$ and $\Delta\phi = -\pi/4$.

Moreover, in the setup considered in this work, the ionization probability does not depend

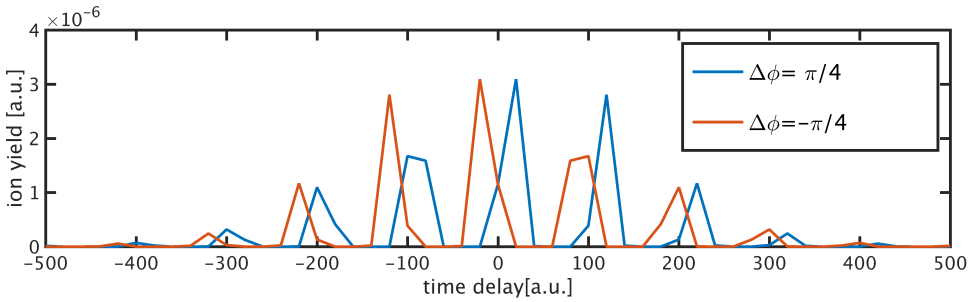

FIGURE 6.3: Comparison of the time-delay pattern of the Ar ion yield for the case of $\Delta\phi = \pi/4$ (blue curve) and $\Delta\phi = -\pi/4$ (red curve). Both curves are exact copies of each other but inverted in time.

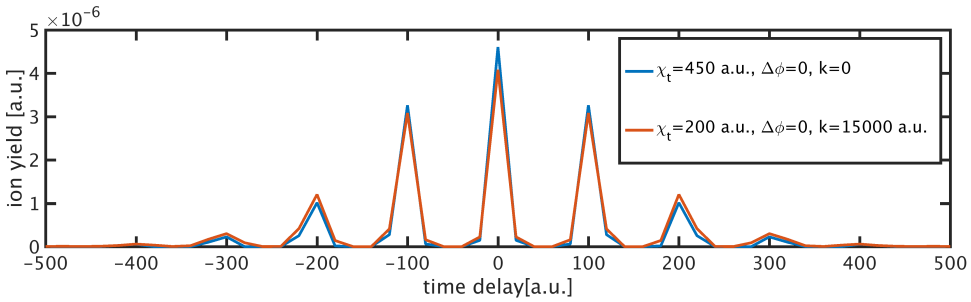

FIGURE 6.4: Comparison of the time-delay pattern of the Ar ion yield for the case of the pulse FWHM $\chi_t = 450$ a.u. and $k = 0$ a.u. (blue), and a case $\chi_t = 200$ a.u. and $k = 15000$ a.u. For both cases the actual pulse duration is almost the same, but the spectrum width is different (see Figure 6.3)

on the sign of a chirp, i.e. $P(\tau, k) = P(\tau, -k)$. In Figure 6.4 we compare the dependence of the ionization probability on the time delay for the pulse $\chi_t = 450$ a.u. with $k = 0$ a.u. and the pulse $\chi_t = 200$ a.u. with $k = 15000$ a.u. (which are shown in Figure 6.2). Although these pulses look quite dissimilar in both domains, the corresponding ionization probabilities are very much alike. However, our technique is sensitive enough to distinguish between them. The envelope of the $P(\tau)$ for the pulse $\chi_t = 450$ a.u. has a smaller FWHM compared to the pulse $\chi_t = 200$ a.u. with $k = 15000$ a.u., because the latter provides a broader width of the spectrum.

In such a way, for any set of pulse parameters χ_t, $\Delta\phi$, k, and for each time delay τ, the ion yield is determined by

- the duration of the combined pulse $E_{sum}(t, \tau) = E_0(t) + E_0(t + \tau)$;
- the interference spectrum of the combined pulse at the given τ;
- the intensity of the combined pulse $I_{sum} = E^2_{sum}$;

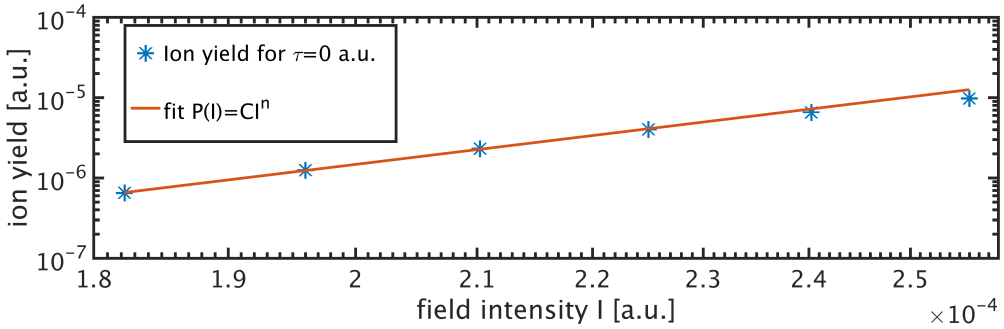

FIGURE 6.5: Dependence of the ion yield on the field intensity I shows a range of intensities, which satisfy a power-law $P(I) = CI^n$, where $C = 1.873510^{26}$ and $n = 8.679$. The illustration is given for overlapping ($\tau = 0$) pulses with no relative phase delay between them ($\Delta\phi = 0$), $I = E_0^2$ and spectrum FWHM $\chi_t = 400$ a.u.

The dependence of the ionization probability on the intensity of the pulse $I_{sum} = E_{sum}^2$ is not uniform for all the pulse parameters and has to be clarified for each specific combination of χ_t and k. For a given delay $\tau = 0$, I performed a number of TDCIS calculations for a range of intensities and then fit a power law

$$P(I) = CI^n, \tag{6.10}$$

where C and n are parameters. In Figure 6.5 we illustrate that, for the range of the pulse intensities $0.00018 < I < 0.00023$ a.u. (field strength $0.0135 < E_0 < 0.015$ a.u.), the ionization probability dependence on the field intensity $P(I)$ fits the power law in Eq. (6.10) with $C = 1.873510^{26}$ and $n = 8.679$. The binding energy for the upper shell of Ar is $E_b \approx 15.7$–15.9 eV, thus ionization requires at least 9–10 of photons $\omega = 1.65$ eV. However, as the short pulses provide a broad photon energy spectrum, the ionization may on occasion require a smaller amount of photons, which will lead to $n < 9$ in a power law in Eq. (6.10).

In general, for any given pulse $E_0(t)$, the ionization probability $P(\tau)$ depends on the local intensity for the corresponding time delay. However, as demonstrated in Figure 6.6, if I universally use the power law determined for the time delay $\tau = 0$ for all other time delays, the prediction error is relatively small. In Figure 6.6 (a) and (c) we present ionization probability $P(\tau)$, calculated with the TDCIS code (data points are shown with circles) for a different intensities of the pulse $E_0(t)$. From the known delay pattern $P(\tau)$ at a field strength of $E_0 = 0.015$ a.u., I retrieve the delay patterns for other intensities (predicted $P(\tau)$ are shown with a solid lines in Figure 6.6 (a) and (c)), by using the power law determined

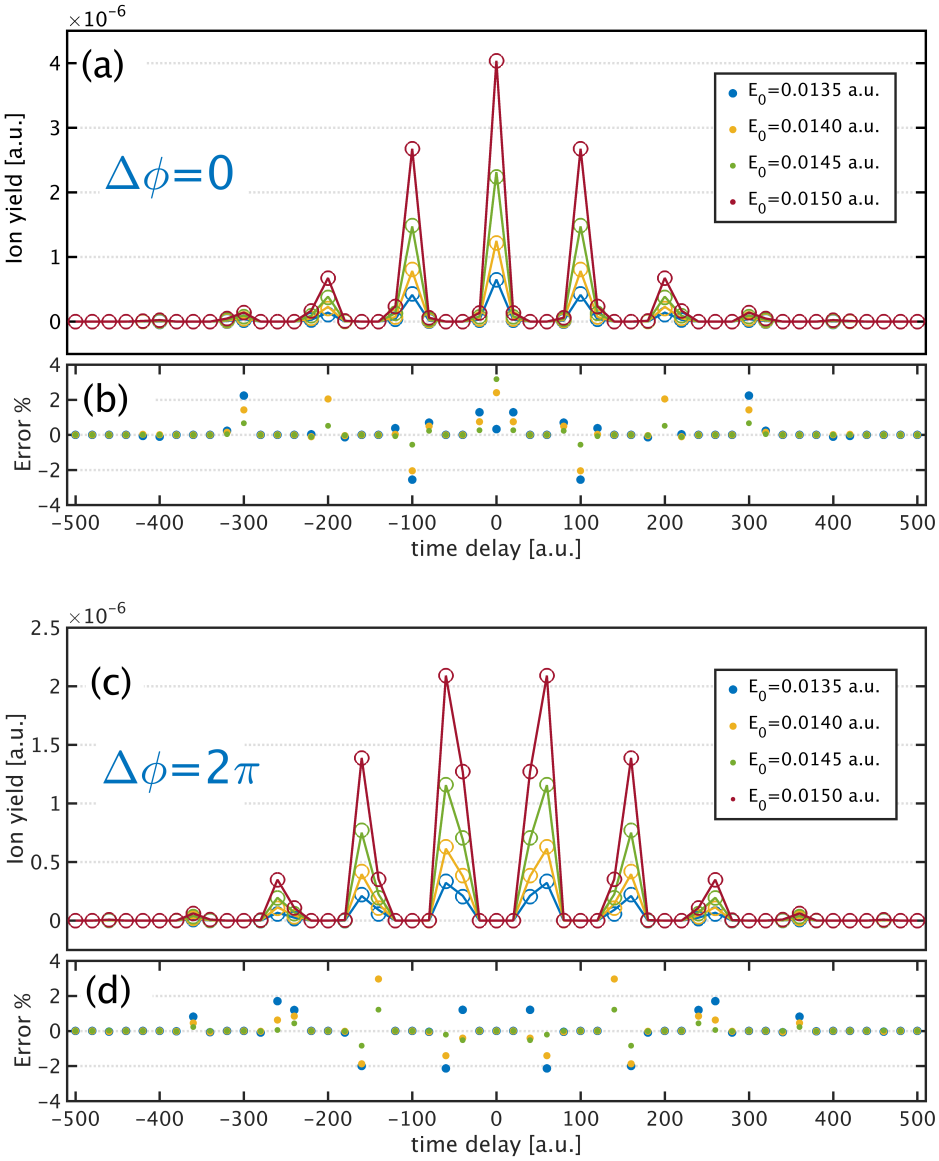

FIGURE 6.6: Application of the power law Eq. (6.10) defined for the $\tau = 0$ time delay to other time delays is examined. The ionisation probability time-delay pattern for the pulse $E_0 = 0.015$ a.u. is extrapolated on the cases of lower field intensities, using the same power-law for all time delays. In (a) and (c) the ionization probability $P(\tau)$ calculated with TDCIS code (data points are shown with circles) is compared with a extrapolated curve, calculated using $P_{E_0}(\tau) = P_{E_0=0.015}(\tau)(E_0/0.015)^n$ for a range of field intensities $I = E_0^2$. Panels (b) and (d) show the prediction error in percent units. Accuracy of a power-law is illustrated by the example of pulse $\chi_t = 400$ a.u., $k = 0$ with a phase shift $\Delta\phi = 0$ and $\Delta\phi = 2\pi$

for the time delay $\tau = 0$. In the Figure 6.6 (b) and (d) one can see the corresponding percentage prediction error for each time delay and each field strength. The prediction error does not exceed 4%. In both Figures (a) and (c) we use the same power law, determined for the time delay $\tau = 0$ and $\Delta\phi = 0$, which shows that the same power-law can be used with the same prediction accuracy for any value of $\Delta\phi$.

6.5 Approximation with a simple formula

In order to provide a choice of resolution in the time-delay patterns of the ionization probability $P(\tau)$ without running an additional TDCIS calculations, we introduce the approximation function:

$$P'(\tau) = P_0 \left[G(\tau - t_0) \cos \left[\omega'(\tau - t_0) + \frac{\phi'}{2} \right]^{nG(\tau - t_0)^m} \right]^2, \tag{6.11}$$

where $G(\tau) = \exp\left[-4\ln(2)\tau^2/\sigma^2\right]$ is a Gaussian envelope with a full width at half maximum σ. The amplitude P_0 of the function $P'(\tau)$ and parameters σ, ω', ϕ', n and m are free parameters, which have to be adjusted for the best fit of $P'(\tau)$ with the known points of $P(\tau)$. The envelope of $P(\tau)$ is centred at $\tau = t_0$, where the two laser fields have zero time delay. The oscillation frequency ω' is the same as the photon energy of the pulse ω.

The parameter ϕ' let us capture the dependence of $P(\tau)$ on the phase shift $\Delta\phi$ of the pulses ($\phi' \approx \Delta\phi$). Comparison of the phase shift $\Delta\phi$ and phase of a fitting function ϕ' for the 100 arbitrary pulses is presented in Fig. 6.7. The fitting parameters for two cases, which differ from each other only through the phase difference $\Delta\phi$, are the same. Thus, knowing the ionization probability $P(\tau)$ for a certain $\Delta\phi$ value, one can easily extrapolate it to other values of $\Delta\phi$ using Eq. (6.11).

To find the best fitting parameters, we use the lmfit package in Python. For any given pulse duration χ_t and chirp k, the best fit accuracy comes for the case of $\Delta\phi = 0$, because $P(\tau)$ for $\tau = 0$ provides the best guess for P_0 parameter. A good strategy turns out to be finding the fitting parameters σ, t_0, ϕ', n and m for the case of $\Delta\phi = 0$ and using them as an initial guess for fitting $P(\tau)$ for other pulses with the same duration χ_t and chirp k. In Figure 6.8 the fitted data for the pulses of $\chi_t = 200$ a.u. but $k = 0$ and $k = 15000$ a.u. are presented to demonstrate sufficiently small fitting errors (an average fitting error of less than 1% per delay point) for sufficiently well-sampled maxima.

Taking into consideration the mapping between parameters of the laser pulse $E_0(t)$ and parameters of the corresponding approximation function $P'(\tau)$ we can use the latter in a

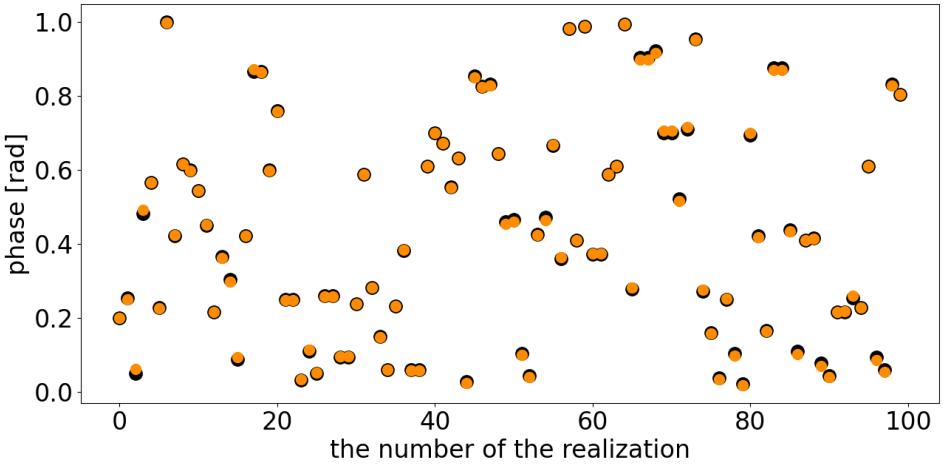

FIGURE 6.7: Comparison of the phase shift $\Delta\phi$ (black dots) and phase of a fitting function ϕ' (orange dots) for the 100 arbitrary pulses.

machine learning algorithm to retrieve the shape of the pulse. For the machine learning algorithm it is better to switch from the standard pulse parameters such as duration χ_t and chirp k to a set of new parameters presented in a table below:

Actual duration of a single pulse $E_0(t)$:	$X = \sqrt{\frac{\chi_t^4 + 16^2 \log(2)^2 k^2}{\chi_t^2}}$
Spectral width of a single pulse $E_0(t)$:	$\chi_\omega = \frac{8\log(2)}{\chi_t}$
Strength of a single pulse $E_0(t)$:	E_0
Phase difference between $E_0(t)$ and $E_0(t+\tau)$:	$\Delta\phi$

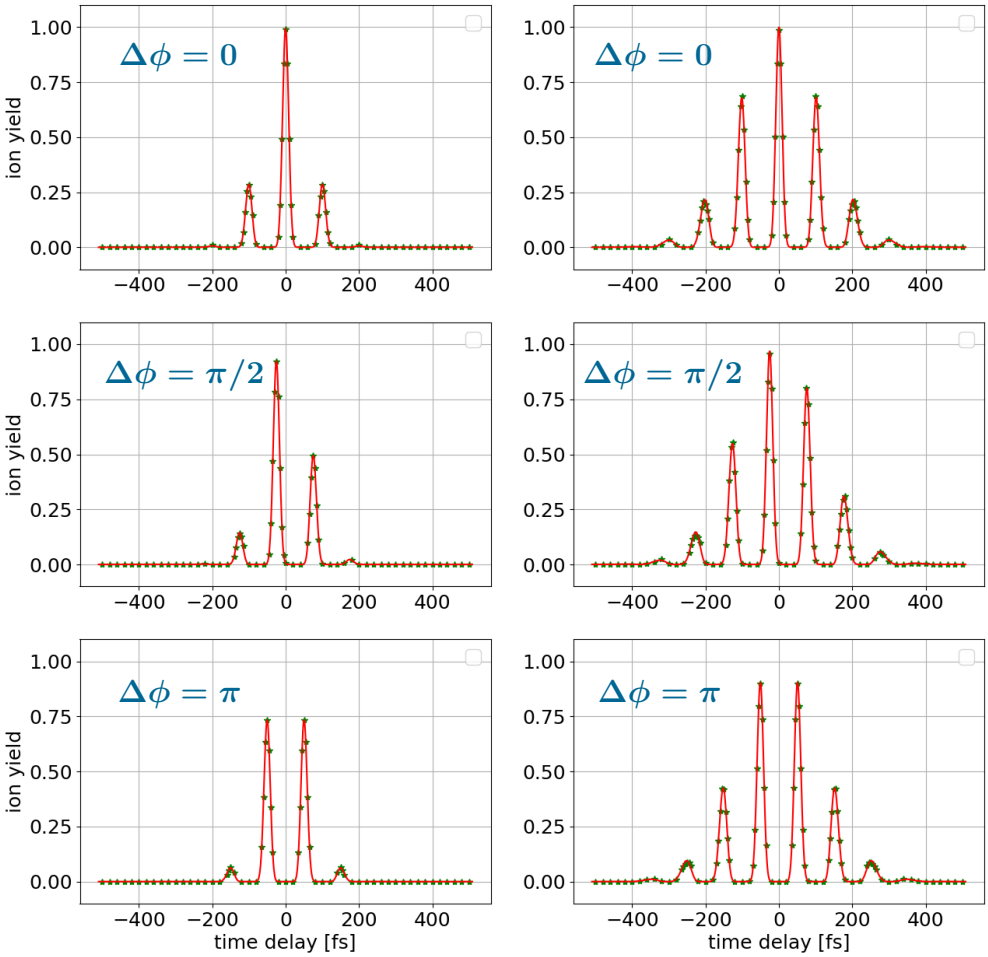

FIGURE 6.8: Approximation of the calculated ion yield $P(\tau)$ (green stars) with the fitting function $P'(\tau)$ (red line) for the pulse $\chi_t = 200$ a.u. with the $k = 0$ (left panels) and $k = 12000$ a.u. (right panels) and different phase shifts $\Delta\phi$.

Chapter 7

Machine learning

In this chapter I present a machine learning model to retrieve the best approximation function for the laser pulse. It takes into consideration the mapping between the autocorrelation of the laser field and the corresponding ionization-probability time-delay pattern of Ar. This method involves approximating the time-delay pattern by a few-parameter function. Feeding these parameters to the machine learning model as a training set provides us with the predicted pulse shape. Multiphoton autocorrelations in Ar are calculated with the TDCIS code.

7.1 Linear regression

Regression analysis is a technique that finds the relationship between a dependent and an independent variable (one or more than one). In order to understand in detail I start by explaining the simplest of the regression models, i.e., linear regression. The linear regression algorithm is one of the fundamental supervised machine-learning algorithms due to its relative simplicity and well-known properties. In linear regression the model assumes the linear relationship between the dependent variable y and the set of independent variables $\mathbf{X} = (x_1, ..., x_n)$: $y = \beta_0 + \beta_1 x_1 + ... + \beta_n x_n + \xi$, where n is the number of predictor, β_i are the regression coefficients, and ξ is the random error. Linear regression calculates the predicted weights $(b_0, b_1, ..., b_n)$, which are used to define the regression function $f(\mathbf{X}) = b_0 + b_1 x_1 + ... + b_n x_n$. $f(\mathbf{X})$ captures the dependencies between the inputs and outputs. The prediction, $f(\mathbf{X}_i)$, for each observation $i = 1, ..., N$ should be in a close proximity to the actual response y_i. Tracking the differences $f(\mathbf{X}_i) - y_i$ will finally provide us with the residuals, smaller the residual the better is the prediction. In order to achieve the best

weights the sum of squared residuals for all observations should be minimum.

$$\eta = \sum_{i=1}^{N} (f(\mathbf{X}_i) - y_i)^2. \tag{7.1}$$

This approach is called the method of least squares. However, for our purposes, the assumption of a linear relationship between input and output may be too rough of an approximation.

7.2 Ensemble Learning

Depending on the type of the dataset i.e., linear or non-linear one needs to choose a regression model. In this work, I use the so-called ensemble-learning method [111]. A model that consists of more than one individual model is known as an ensemble model. It is a technique which calculates the predictions from various machine learning algorithms together without any dependence on one another so as to predict results more accurately than any single model. Noise, bias and variance are some of the important factors that cause errors in learning models. Models based on the ensemble method reduce these factors and provide stability and accuracy of predicted results. Ensemble learning algorithms can be sub-divided as follows.

Boosting is an iterative, sequential technique which utilizes weighted averages to turn weak learners into strong learners. The learner algorithms are always learning from the data but are not always completely accurate. Sometimes they are weak and poor when it comes to learning the relationships between inputs and target. Boosting adjusts the weight of an observation based on the last regression. The first algorithm is trained on the entire data set and the subsequent algorithms are built by fitting the residuals (differences between observed and predicted values of data) of the first algorithm. One algorithm is learning from other which in turn boosts the learning. Boosting in general decreases the bias error. It has shown better predictive accuracy than bagging (described below) but it also tends to overfit the training data. Therefore, parameter tuning becomes an important part of boosting algorithms to make it avoid overfitting.

Bootstrapping (or *Bagging*) is a technique in which random samples are selected from the overall dataset with replacement (subsets of training data set) for predicting results. It gives a much better insight towards bias and variance within the dataset. Exposing different subsets to each model is the key to use their collective output at the end. The combination

of multiple models decreases variance and produces more reliable predictions than a single model. Hence, the problem of overfitting is taken care of.

$Stacking$ is a method based on the concept of meta learners where it combines models of different types. It considers heterogeneous weak learners and operates them in parallel and finally combines them using a meta-model to make predictions based on the different weak model outputs. It consists of the following steps: $i)$ splitting the training data set into two disjoint sets, $ii)$ training different base learners on one of the sets, $iii)$ testing the trained base learners on the second set and $iv)$ using the predictions from the base learners as inputs and considering the correct responses as the output, a higher level learner is trained.

7.3 Random forest regression

The traditional machine learning algorithms usually give low accuracy, and can easily undergo overfitting. In this work, I use one of the random forest (RF) algorithms [111]. It does not have this problem since it is a combination of machine learning algorithms like multiple decision trees. It belongs to the category of bagging technique. The algorithm is combined with a series of tree regressors, each tree cast a unit vote for the most popular regressor, then combine these results and gives the final sort result. This scheme allows to improve the accuracy and avoid overfitting. The RF algorithm is not biased, since, there are multiple trees and each tree is trained on a subset of data. Basically, the algorithm relies on the power of "the crowd", therefore the overall biasedness of the algorithm is reduced. The RF algorithm is usually very stable, and even if a new data point is introduced to the dataset the overall algorithm is not affected much since new data may impact one tree, but it is very hard for it to impact all the trees.

The RF method consists of the following steps: pick a number N of random records from the dataset, build a decision tree based on these N records, then choose the number of trees one wants in the algorithm and repeat first two steps. For a new record, each tree in the forest predicts a value for output. The final value can be calculated by taking the average of all the values predicted by all the trees in forest. In RF, each decision tree in the ensemble is constructed from a sample taken with replacement from the training set. The best split of each decision node of a tree is found either from all input features or a random subset with an adjusted size. Individual decision trees typically exhibit high variance and tend to overfit, but these two sources of randomness serve to decrease the variance of the forest estimator. The injected randomness in forests yields decision trees with somewhat decoupled prediction errors. By taking an average of those predictions, the overall error is getting smaller. RF achieves a reduced variance by combining diverse trees. The reduction

of variance yields an overall better model. The scikit-learn implementation we use in our work combines regressors by averaging their probabilistic prediction, instead of letting each regressor vote for a single answer [112].

7.4 Pulse characterization

Here, I will explain the step-by-step evaluation of the best pulse parameters using machine learning via the RF method. First, I provide the algorithm with a learning data set: for the pulses with known spectrum width χ_ω and real pulse duration X I provide with the corresponding parameters t_0, σ, ϕ', n and m of the ionization-probability approximation function $P'(\tau)$ [Eq. (6.11)], as it is shown in a table below.

χ_ω	X	t_0	σ	ϕ'	n	m
0.021	390.632	4.518e-02	7.158	1.232e-01	4.995	0.275
0.020	367.897	2.363e-18	6.886	1.000e+00	7.291	0.011
0.019	282.843	-2.042e-17	5.224	9.999e-01	7.450	-0.008
0.019	483.472	1.535e-16	8.825	4.233e-10	7.111	0.046
0.019	548.992	2.643e-17	9.785	1.000e+00	7.123	0.116
...	...	...	...	...	...	...
0.009	637.559	-1.315e-02	10.437	7.327e-01	9.457	0.171
0.009	688.291	2.334e-02	11.195	2.672e-01	9.401	0.200
0.009	688.291	-2.334e-02	11.195	7.327e-01	9.401	0.200
0.009	574.116	3.764e-03	9.457	2.672e-01	9.568	0.136
0.009	574.116	-3.762e-03	9.457	7.327e-01	9.568	0.136

We let the algorithm find correlations between the features and the target (pulse parameters) in the learning data. The correlation has been calculated using Pearson's correlation coefficient [113], which is based on the method of covariance. It measures the relationship between two continuous variables. The strength of the relationship depends on the value of the correlation coefficient and its value varies from -1 to +1. A correlation matrix is presented in Figure 7.1 where each cell represents the correlation coefficients for different variables. This matrix shows the correlation between all the possible pairs of values. The correlation map shows a strong negative correlation between χ_ω and coefficient n (correlation coefficient is -0.91) and strong positive correlation between X and coefficient σ (correlation coefficient is 0.99). High correlation between parameters X and χ_ω of the laser field with one of parameters of the approximation function $P'(\tau)$ gives an opportunity to

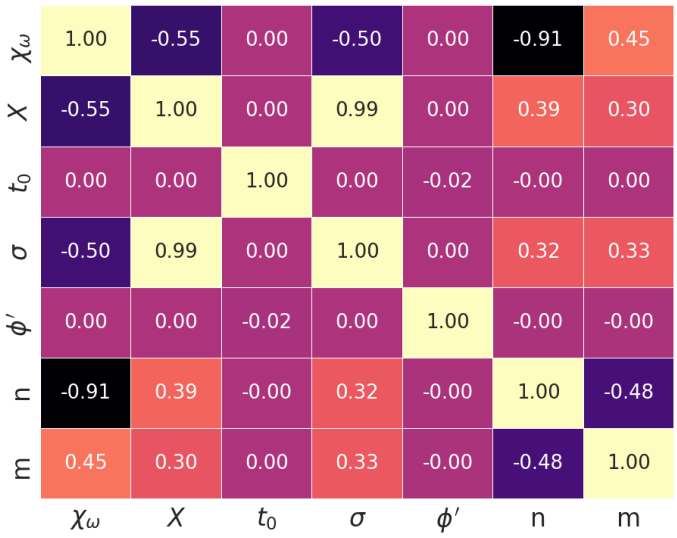

FIGURE 7.1: Correlation matrix.

reconstruct the shape of the laser pulse from the Ar gas ionization response. Instead, the low-correlated features are filtered out by the algorithm and are not used for prediction.

To proceed, we use a RF algorithm to find the best prediction model. The search is accompanied by a grid-search cross-validation method to determine the optimal values to be used for the hyperparameters of our model from a specified range of values. Grid-search cross-validation is an exhaustive search over hyperparameters. There are many parameters in the RF method that require attention to come up with optimised values of hyperparameters i.e., *n_estimators* – number of trees in the forest, *max_depth* – maximum depth of the tree, *max_features* – number of features (σ, n and m etc.) to be used, *min_sample_split* – minimum number of samples required to split a node along with other parameters. Grid-search cross-validation uses the list of parameters provided and performs an exhaustive search by implementing a "fit" and a "score" method along with several other methods like predict, *predict_proba* and *decision_function*. Finally, a grid is created and the parameters of the estimators used to apply these methods are optimized by cross-validation over a specified parameter grid. Model validation techniques serve for assessing how the results of a statistical analysis will generalize to an independent data set. Learning the parameters of a prediction function and testing it on the same data is a methodological mistake, as a model that would just repeat the labels of the samples that it has just seen would have a perfect score but would fail to predict anything useful on yet unseen data. This situation is called overfitting. To avoid it, we hold out part of the available data as a test set, when performing

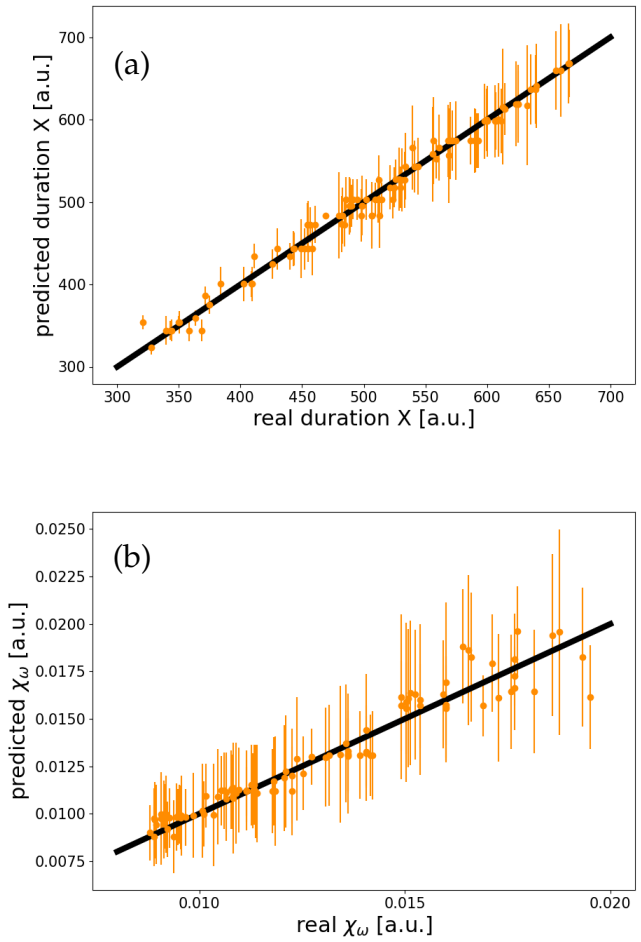

FIGURE 7.2: Comparison of the actual parameters (a) duration X and (b) spectrum width χ_ω of the 100 pulses with the predicted values found with a best prediction model by RF algorithm. Black line shows the trend of a perfect prediction.

a (supervised) machine learning experiment.

In our case the best model from grid-search for prediction of pulse duration X has an accuracy of 98.86 % and for spectrum width of the pulse χ_ω is 99.77 %. In Figs. 7.2 we present an accuracy of the best prediction model for (a) the real pulse duration X and (b) the spectrum width χ_ω. In Fig. 7.2 the actual values of the pulse parameters are given on x-axis and the predicted values on y-axis. Orange points with the error bars provide the comparison of a predicted and actual value of parameter (a) duration X, and (b) spectrum width χ_ω. Black line shows the trend of a perfect guess. The accuracy of prediction for the duration X is rather good. Prediction for the spectrum width χ_ω is more efficient for the pulses of a

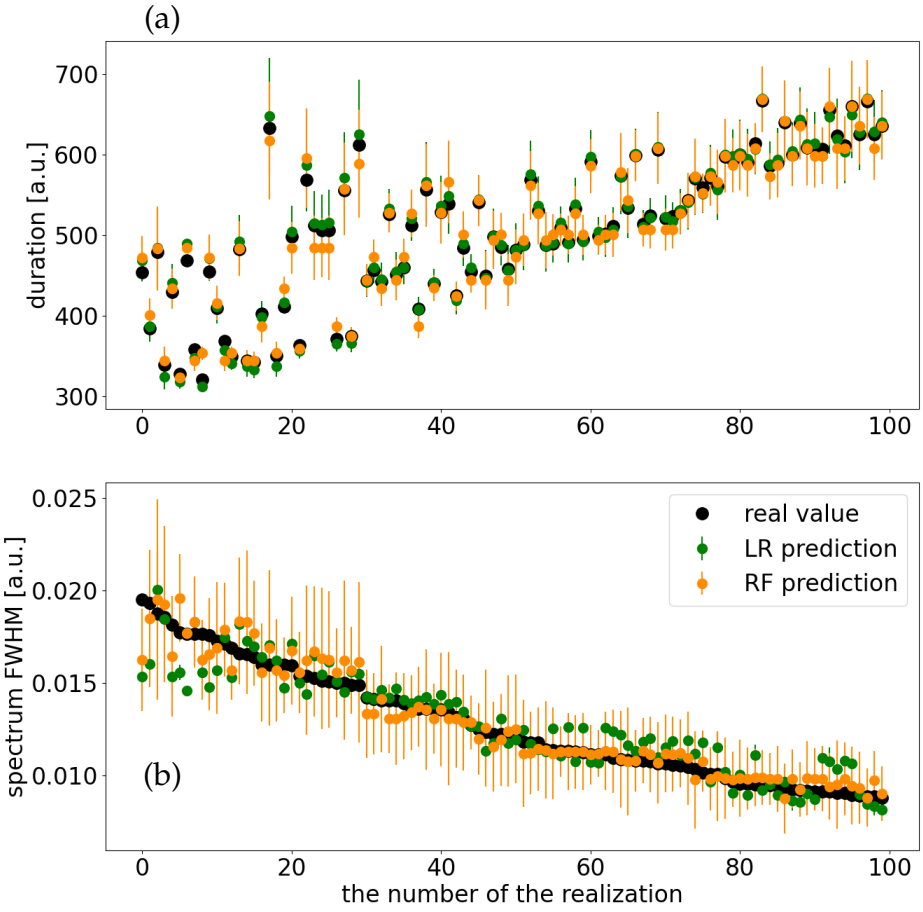

FIGURE 7.3: Comparison of the actual parameters (a) duration X, and (b) spectrum width χ_ω of the 100 pulses (black dots) with the predicted values. Orange dots with errorbar represent the values found with a best prediction model by RF algorithm. Green dots with errorbar represent the values found with a linear regression algorithm.

narrow spectrum.

In order to demonstrate the validity of the analysis in terms of final predictions, we compare the results of RF method with linear regression model. In Fig. 7.3 a comparison with a linear regression algorithm prediction is presented. The actual values of the pulse parameters are shown with black color and the predicted with our RF algorithm values with orange dots with error bars. Green dots correspond to a values predicted with a linear regression algorithm. One can see that prediction with the RF algorithm works pretty good for both duration and spectrum prediction, whereas the linear regression technique gives

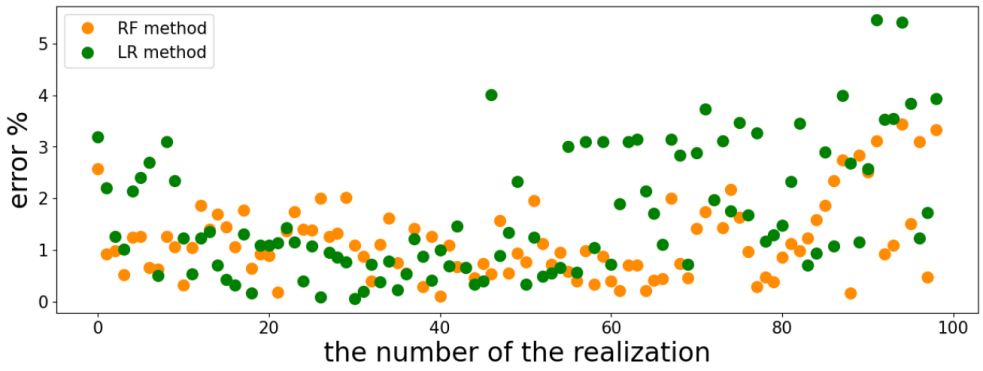

FIGURE 7.4: Comparison of the overall error in pulse reconstruction using linear regression (green dots) and RF techniques (orange dots).

worse results in a spectrum FWHM prediction.

The overall error in the pulse reconstruction from the $P(\tau)$ function in our technique is less than 4 %. In Figure 7.4 the overall error for the pulse prediction for a linear regression technique is compared with the prediction error with RF algorithm. In Figure 7.5 we present the comparison of the actual pulse $E_0(t)$ (shown in black) used in simulations with the pulse shape predicted by RF method (orange line) and with linear regression model (green line). It can be noted that Figure 7.5 consists only of those cases with the largest prediction error.

7.5 Conclusion

The machine learning method I presented in this chapter characterizes laser pulses with a good accuracy. The approximation function $P'(\tau)$ from Chapter 6 [Eq. (6.11)] that I use in this method is very simple and does not capture all the features of the $P(\tau)$. Finding a better approximation function will improve the accuracy of the pulse characterization. However, even with a $P'(\tau)$ from Eq. (6.11) the accuracy of a pulse characterization is already satisfactory. Decision trees are computationally expensive to train and, they carry a big risk of overfitting, and tend to find local optima because they cannot go back after they make a split. To address these weaknesses, we turn to RF which illustrates the power of combining many decision trees into one model. Exploiting a RF technique makes our method flexible for more sophisticated approximation functions, which could have more fitting parameters or/and which parameters could have strongly non-linear dependence on the actual pulse parameters. It can be concluded from the above mentioned machine learning analysis that the RF method can be applied to train and predict pulse shapes based on the pulse parameters.

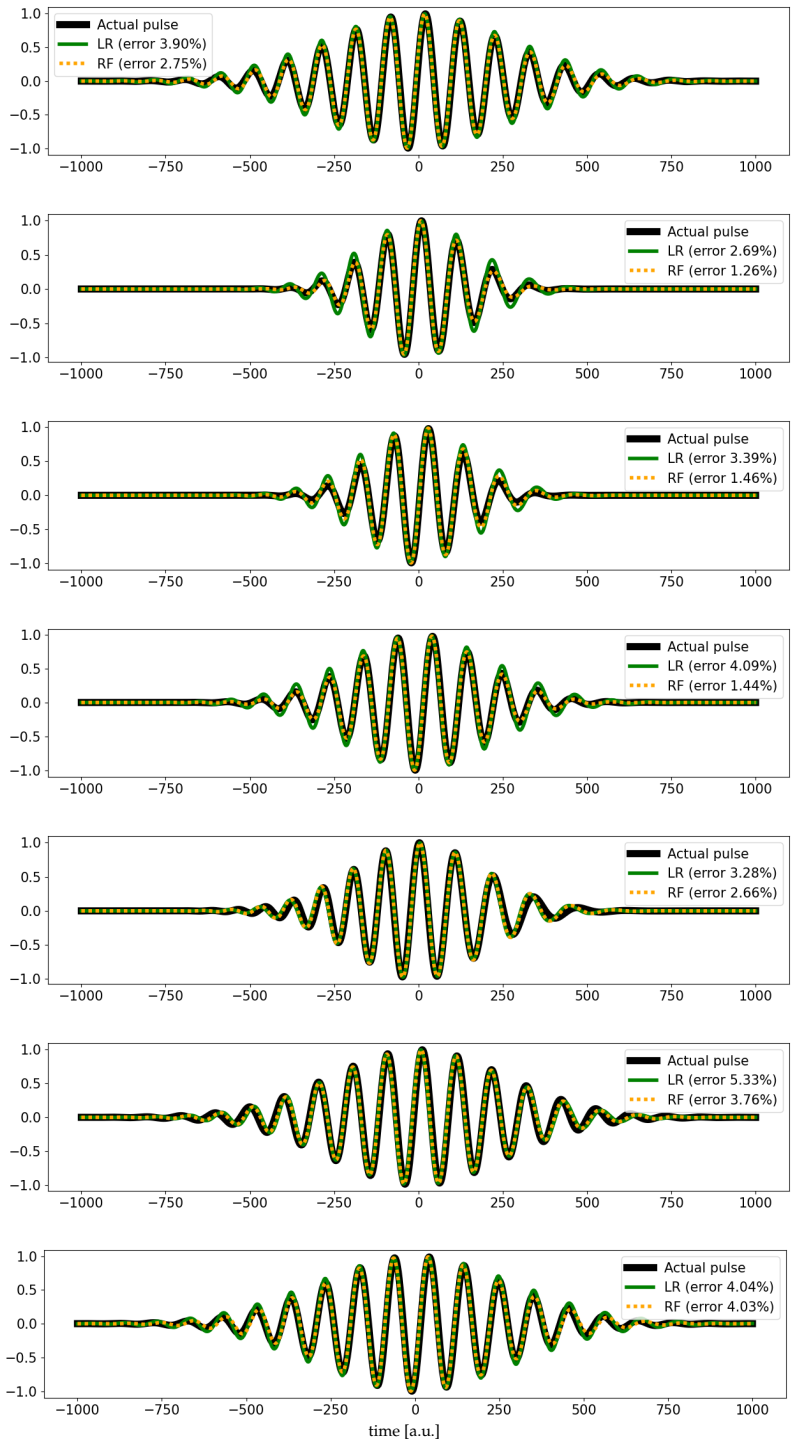

FIGURE 7.5: Comparison of the actual pulse E_0 shape used in simulations $P(\tau)$ with the pulse shape found by our method from the $P(\tau)$ (orange line), and by linear regression technique (green line) is presented for the cases with the biggest prediction error.

Chapter 8

Summary and outlook

Within my doctoral work, I performed a theoretical study of the processes driven in the atomic systems under the influence of a time-delayed electromagnetic field. Depending on the field parameters, different processes in the atom can be driven and thus various phenomena can be studied. The XUV pulse provides access to processes involving the inner shells of the atom. Conversely, an NIR field affects mostly the Rydberg electrons and upper shells of the atom. Depending on the strength of the NIR field acting on the atom either electronic excitation or ionization may be induced. In this work, we characterized the inner-atomic dynamics, via excitation of the atom by a time-delayed attosecond XUV and femtosecond optical field. In addition, we were able to characterize the laser field, and retrieve its pulse parameters by calculating the autocorrelation function of the field during multiphoton ionization processes of the atom.

I have derived an analytical theory of attosecond transient absorption spectroscopy for perturbatively dressed systems, which is applicable to the analysis of processes observed in pump-probe experiments, provided both the pump and the probe fields are sufficiently weak. The presented technique is suitable for more complicated systems as well. The time-delayed dressing of the excited system provides a tool for the detection of the interference processes inside of the system, as well as coupling between the system states. The analytical expressions derived allow for the study of different aspects of the dynamic inside of the system separately from each other. Thus, the derived theoretical framework may provide insight as to how particular laser-driven atomic phenomena reveal themselves experimentally.

I proceeded by applying the aforementioned analytical theory to a model atom so as to explore the capabilities of ATAS. Having a freedom to choose the parameters of the system allows us to highlight different features, which in principle can be observed using ATAS

technique with weak XUV and NIR pulses. By exploring the dependence of the ATA spectrum on the parameters of the atom, it was shown how different excitation paths interfere with each other, which caused oscillations in the XUV cross section of an XUV photon absorption with a time delay. It is illustrated that the time-delay cross-section oscillation is sensitive to the magnitude and the relative phase (sign) of the dipole moment between the states of the atom involved in a process. Also, the dependence of ATA spectrum on the pulse parameters revealed that shorter pulses are more suitable for observations of inner-atomic dynamics. By limiting the available excitation pathways and examining them separately, it is shown how they participate in the general ATA spectrum. In such a way the destructive and constructive interference of a process is illustrated.

Finally, I have applied the developed theory to a real atomic system. I have presented a numerical simulation of an ATAS experiment on a Xe atom and compared our results with the experiment. It is demonstrated that various aspects of coherent electron dynamics can be revealed when wave packets prepared by an attosecond pump pulse are probed using an NIR pulse. It was demonstrated that inner-shell hole dynamics are much more difficult to detect than Rydberg-electron dynamics. The dynamics of the inner-shell hole are defined mostly by the degree of coherence of the wave packet initially created by the XUV pulse. Conversely, Rydberg electrons produce strong quantum-coherence effects due to the dressing by the NIR pulse, which are reflected in the ATA spectrum. The transition dipole moment between states with different angular momentum j of the (inner-shell) hole is much weaker than for the states with the same j. Therefore, the evolution of wave-packet components with a different j of the corresponding hole, are mostly independent from each other, and thus not so sensitive to the presence of the probe field. Our analysis suggests that, in order to detect inner-shell hole dynamics using an NIR probe field, it is necessary to minimize the effect of the laser field on the Rydberg levels, which can be done by decreasing the field exposure time and by using fields that are far off resonance.

Also in my work, it is shown that the presence of a dressing field or a slight modification of the spectrum of the probe pulse can dramatically change the ATA spectrum. Thus, a precise NIR pulse characterization is necessary for a qualitatively and quantitatively accurate interpretation of experimental ATAS data.

Thus, the second part of my work is devoted to precise pulse characterization. I present a machine-learning method to characterize a laser pulse with a good accuracy. The method is based on the analysis of a multiphoton autocorrelation in Ar. First, I calculated the multiphoton autocorrelation for a larger variety of data using the XCID code for multichannel

ionization dynamics, which exploits TDCIS method for treating atomic processes. Studying the obtained time-delay patterns, I found an approximation function of few parameters, which allows for an arbitrary change in resolution of a calculated time-delay pattern without the need for additional calculations with XCID (which can be extremely time consuming). Secondly, I have trained a machine-learning model to find correlations between the parameters of the pulse and parameters of the approximation function for the corresponding ionization-probability delay pattern. Thus, eventually a tool is obtained to retrieve pulse parameters from observed ionization probabilities. Our method is flexible to deal with experimentally measured time-delay patterns with not-well-defined zero time delay, or patterns measured with a different (even non-uniform) time-delay steps. Moreover, our method can be applied for a characterization of the pulse of a different photon energy as well. Though, approximation function that is used in our method is very simple to use and highly time efficient, it however does not capture all the features of the ionization-probability time-delay dependence. Finding a better approximation function will improve the accuracy of the pulse characterization. However, even with the suggested approximation function from Eq. (6.11) the accuracy of pulse characterization is already satisfactory.

Appendix A

TABLE A.1: Energies and transition dipole moments of the $4d$-excited states of Xe used in our ATAS calculations, significant for convergence. The states listed below ground state (GS) are dark states, whereas the states listed horizontally in the first row are $J^P = 1^-$ bright states. The values in parentheses are for $np_{1/2}$; otherwise for $np_{3/2}$.

state, J^P		$4d_{5/2}^{-1}6p^1$	$4d_{3/2}^{-1}6p^1$	$4d_{5/2}^{-1}7p^1$	$4d_{3/2}^{-1}7p^1$	$4d_{5/2}^{-1}8p^1$	$4d_{3/2}^{-1}8p^1$
	E, eV	**65.110**	**67.039**	**66.375**	**68.345**	**67.150**	**69.150**
GS	**0**	−0.182	−0.138 (0.052)	−0.106	−0.015 (–0.083)	−0.072	−0.020 (–0.054)
$4d_{3/2}^{-1}6s_{1/2}^1 2^+$	**65.67**	−0.039	−8.989 (3.521)	0.000	−0.032 (–0.796)	0.000	−0.042 (–0.302)
$4d_{5/2}^{-1}6s_{1/2}^1 2^+$	**63.707**	9.548	0.075 (0.092)	1.047	0.000 (0.000)	0.444	0.000 (0.000)
$4d_{3/2}^{-1}7s_{1/2}^1 2^+$	**67.877**	0.088	−8.029 (2.757)	−0.038	−3.805 (–19.266)	0.002	−0.466 (–1.829)
$4d_{5/2}^{-1}7s_{1/2}^1 2^+$	**65.830**	9.200	−0.127 (–0.066)	19.236	−0.069 (0.050)	2.324	−0.004 (0.000)
$4d_{3/2}^{-1}8s_{1/2}^1 2^+$	**68.587**	0.022	−1.810 (0.695)	0.061	−2.735 (–17.592)	−0.034	−11.786 (–30.662)
$4d_{5/2}^{-1}8s_{1/2}^1 2^+$	**66.538**	1.948	−0.029 (–0.013)	19.052	0.062 (–0.078)	32.021	−0.045 (0.050)
$4d_{3/2}^{-1}9s_{1/2}^1 2^+$	**68.907**	0.012	−0.944 (0.369)	0.014	−0.703 (–3.565)	0.046	−9.644 (–28.448)
$4d_{5/2}^{-1}9s_{1/2}^1 2^+$	**66.858**	1.004	−0.016 (–0.007)	3.561	0.011 (–0.016)	31.964	0.037 (–0.067)
$4d_{3/2}^{-1}10s_{1/2}^1 2^+$	**69.078**	0.008	−0.620 (0.244)	0.007	−0.367 (–1.793)	0.010	−2.084 (–5.374)
$4d_{5/2}^{-1}10s_{1/2}^1 2^+$	**67.028**	0.657	−0.010 (–0.004)	1.765	0.006 (–0.008)	5.581	0.006 (–0.013)
$4d_{3/2}^{-1}11s_{1/2}^1 2^+$	**69.179**	0.006	−0.453 (0.179)	0.005	−0.240 (–1.159)	0.005	−1.044 (–2.631)
$4d_{5/2}^{-1}11s_{1/2}^1 2^+$	**67.130**	0.479	0.000 (–0.003)	1.134	0.004 (–0.006)	2.692	0.003 (–0.006)
$4d_{3/2}^{-1}12s_{1/2}^1 2^+$	**69.245**	0.005	−0.353 (0.140)	0.004	−0.176 (–0.841)	0.000	−0.671 (–1.677)
$4d_{5/2}^{-1}12s_{1/2}^1 2^+$	**67.195**	0.373	0.000 (0.000)	0.821	0.003 (–0.004)	1.706	0.002 (–0.004)
$4d_{3/2}^{-1}13s_{1/2}^1 2^+$	**69.289**	0.004	−0.286 (0.113)	0.000	−0.137 (–0.653)	0.000	−0.486 (–1.209)
$4d_{5/2}^{-1}13s_{1/2}^1 2^+$	**67.239**	0.302	0.000 (0.000)	0.636	0.002 (–0.003)	1.225	0.001 (–0.003)
$4d_{3/2}^{-1}14s_{1/2}^1 2^+$	**69.321**	0.003	−0.239 (0.095)	0.000	−0.111 (–0.529)	0.000	−0.376 (–0.934)
$4d_{5/2}^{-1}14s_{1/2}^1 2^+$	**67.271**	0.252	0.000 (0.000)	0.515	0.002 (–0.003)	0.945	0.001 (–0.002)
$4d_{3/2}^{-1}15s_{1/2}^1 2^+$	**69.345**	0.003	−0.203 (0.081)	0.000	−0.093 (–0.441)	0.000	−0.304 (–0.755)
$4d_{5/2}^{-1}15s_{1/2}^1 2^+$	**67.295**	0.214	0.000 (0.000)	0.429	0.001 (–0.002)	0.763	0.001 (–0.002)
$4d_{3/2}^{-1}16s_{1/2}^1 2^+$	**69.364**	0.002	−0.176 (0.070)	0.000	−0.079 (–0.377)	0.000	−0.254 (–0.629)
$4d_{5/2}^{-1}16s_{1/2}^1 2^+$	**67.314**	0.186	0.000 (0.000)	0.366	0.001 (–0.002)	0.636	0.001 (–0.002)
$4d_{3/2}^{-1}17s_{1/2}^1 2^+$	**69.378**	0.002	−0.155 (0.061)	0.000	−0.069 (–0.327)	0.000	−0.217 (–0.537)
$4d_{5/2}^{-1}17s_{1/2}^1 2^+$	**67.328**	0.163	0.000 (0.000)	0.318	0.001 (–0.002)	0.542	0.001 (–0.001)

Continued on next page

Table A.1 – continued from previous page

state, J^P		$4d^{-1}_{5/2}6p^1$	$4d^{-1}_{3/2}6p^1$	$4d^{-1}_{5/2}7p^1$	$4d^{-1}_{3/2}7p^1$	$4d^{-1}_{5/2}8p^1$	$4d^{-1}_{3/2}8p^1$
	E, eV	**65.110**	**67.039**	**66.375**	**68.345**	**67.150**	**69.150**
GS	**0**	−0.182	−0.138 (0.052)	−0.106	−0.015 (−0.083)	−0.072	−0.020 (−0.054)
$4d^{-1}_{3/2}18s^1_{1/2}2^+$	**69.389**	0.002	−0.137 (0.055)	0.000	−0.061 (−0.288)	0.000	−0.189 (−0.466)
$4d^{-1}_{5/2}18s^1_{1/2}2^+$	**67.339**	0.145	0.000 (0.000)	0.279	0.001 (−0.001)	0.471	0.001 (−0.001)
$4d^{-1}_{3/2}19s^1_{1/2}2^+$	**69.399**	0.002	−0.123 (0.049)	0.000	−0.054 (−0.256)	0.000	−0.166 (−0.411)
$4d^{-1}_{5/2}19s^1_{1/2}2^+$	**67.349**	0.130	0.000 (0.000)	0.249	0.001 (−0.001)	0.414	0.000 (−0.001)
$4d^{-1}_{3/2}20s^1_{1/2}2^+$	**69.407**	0.002	−0.111 (0.044)	0.000	−0.049 (−0.230)	0.000	−0.148 (−0.366)
$4d^{-1}_{5/2}20s^1_{1/2}2^+$	**67.357**	0.117	0.000 (0.000)	0.223	0.001 (−0.001)	0.369	0.000 (−0.001)
$4d^{-1}_{5/2}5d^1_{3/2}2^+$	**65.439**	1.051	0.000 (0.000)	1.622	0.005 (−0.008)	2.274	0.002 (−0.006)
$4d^{-1}_{5/2}5d^1_{5/2}2^+$	**65.439**	4.693	0.000 (0.000)	7.310	0.023 (−0.037)	10.330	0.010 (−0.027)
$4d^{-1}_{3/2}5d^1_{5/2}2^+$	**67.408**	0.098	−4.935 (−2.958)	0.052	5.944 (−6.669)	0.034	6.723 (−10.642)
$4d^{-1}_{3/2}5d^1_{3/2}2^+$	**67.409**	−0.029	−0.513 (5.785)	0.000	−8.621 (−2.275)	0.000	−12.389 (−0.935)
$4d^{-1}_{5/2}5d^1_{5/2}0^+$	**65.647**	3.624	0.000 (0.000)	5.637	0.018 (−0.028)	7.956	0.008 (−0.019)
$4d^{-1}_{3/2}5d^1_{3/2}0^+$	**67.513**	−0.043	3.149 (−1.040)	−0.022	0.629 (5.027)	−0.014	1.960 (6.746)
$4d^{-1}_{5/2}6d^1_{3/2}2^+$	**66.495**	0.252	0.000 (−0.001)	−2.938	0.000 (−0.029)	−1.495	0.000 (0.019)
$4d^{-1}_{5/2}6d^1_{5/2}2^+$	**66.495**	2.068	−0.030 (−0.010)	−21.661	−0.023 (0.082)	−10.576	0.000 (0.000)
$4d^{-1}_{3/2}6d^1_{5/2}2^+$	**68.475**	0.038	−2.063 (−1.384)	−0.115	−17.572 (20.009)	0.016	−6.607 (11.368)
$4d^{-1}_{3/2}6d^1_{3/2}2^+$	**68.475**	−0.013	−0.045 (2.271)	0.025	26.151 (9.130)	−0.001	14.159 (3.112)
$4d^{-1}_{5/2}6d^1_{5/2}0^+$	**66.495**	1.565	−0.007 (−0.015)	−16.526	−0.093 (−0.147)	−8.097	0.056 (0.095)
$4d^{-1}_{3/2}6d^1_{3/2}0^+$	**68.475**	0.005	1.230 (−0.302)	−0.167	−2.861 (−15.956)	0.100	−3.272 (−7.981)
$4d^{-1}_{5/2}7d^1_{3/2}2^+$	**66.963**	0.371	−0.004 (−0.002)	0.688	0.001 (−0.001)	−9.928	−0.004 (−0.017)
$4d^{-1}_{5/2}7d^1_{5/2}2^+$	**66.968**	1.355	−0.021 (−0.008)	2.617	0.005 (−0.012)	−34.973	−0.002 (0.064)
$4d^{-1}_{3/2}7d^1_{5/2}2^+$	**69.014**	0.028	−1.402 (−1.053)	0.016	2.515 (−2.204)	−0.085	−27.138 (36.900)
$4d^{-1}_{3/2}7d^1_{3/2}2^+$	**69.020**	0.000	−0.240 (1.523)	−0.004	−2.564 (−0.616)	0.010	43.188 (10.952)
$4d^{-1}_{5/2}7d^1_{5/2}0^+$	**66.982**	1.057	−0.010 (−0.009)	2.025	0.006 (0.003)	−27.479	−0.104 (−0.139)
$4d^{-1}_{3/2}7d^1_{3/2}0^+$	**69.027**	−0.004	0.881 (−0.260)	0.009	0.000 (1.536)	−0.172	−9.172 (−25.357)
$4d^{-1}_{5/2}8d^1_{3/2}2^+$	**67.191**	0.940	−0.015 (−0.006)	1.758	0.004 (−0.008)	3.157	0.002 (−0.007)
$4d^{-1}_{5/2}8d^1_{5/2}2^+$	**67.188**	0.325	−0.005 (−0.002)	0.597	0.001 (−0.002)	1.030	0.000 (−0.001)
$4d^{-1}_{3/2}8d^1_{5/2}2^+$	**69.238**	0.020	−0.990 (−0.780)	0.012	1.773 (−1.530)	0.009	2.709 (−3.140)
$4d^{-1}_{3/2}8d^1_{3/2}2^+$	**69.242**	0.000	−0.223 (1.071)	0.000	−1.816 (−0.656)	−0.002	−2.976 (−0.137)
$4d^{-1}_{5/2}8d^1_{5/2}0^+$	**67.199**	0.749	−0.009 (−0.006)	1.394	0.005 (−0.001)	2.477	0.004 (0.002)
$4d^{-1}_{3/2}8d^1_{3/2}0^+$	**69.246**	−0.005	0.635 (−0.197)	0.000	0.091 (1.163)	0.008	0.211 (1.751)
$4d^{-1}_{5/2}9d^1_{3/2}2^+$	**67.312**	0.197	−0.003 (−0.001)	0.345	0.001 (−0.001)	0.585	0.000 (−0.001)
$4d^{-1}_{5/2}9d^1_{5/2}2^+$	**67.314**	0.725	−0.011 (−0.004)	1.284	0.004 (−0.006)	2.226	0.002 (−0.005)
$4d^{-1}_{3/2}9d^1_{5/2}2^+$	**69.363**	0.016	−0.750 (−0.585)	0.009	1.262 (−1.105)	0.007	1.844 (−2.227)
$4d^{-1}_{3/2}9d^1_{3/2}2^+$	**69.365**	0.000	−0.173 (0.818)	0.000	−1.331 (−0.507)	0.000	−2.296 (−0.338)
$4d^{-1}_{5/2}9d^1_{5/2}0^+$	**67.319**	0.566	−0.008 (−0.004)	0.999	0.003 (−0.002)	1.725	0.003 (0.000)
$4d^{-1}_{3/2}9d^1_{3/2}0^+$	**69.368**	−0.005	0.484 (−0.154)	0.000	0.084 (0.857)	0.002	0.307 (1.359)
$4d^{-1}_{5/2}10d^1_{3/2}2^+$	**67.388**	−0.057	0.000 (0.000)	−0.095	0.000 (0.000)	−0.149	0.000 (0.000)
$4d^{-1}_{5/2}10d^1_{5/2}2^+$	**67.389**	0.592	0.000 (0.000)	1.010	0.003 (−0.005)	1.648	0.001 (−0.004)

Continued on next page

Table A.1 – continued from previous page

state, J^P		$4d^{-1}_{5/2}6p^1$	$4d^{-1}_{3/2}6p^1$	$4d^{-1}_{5/2}7p^1$	$4d^{-1}_{3/2}7p^1$	$4d^{-1}_{5/2}8p^1$	$4d^{-1}_{3/2}8p^1$
	E, eV	**65.110**	**67.039**	**66.375**	**68.345**	**67.150**	**69.150**
GS	**0**	−0.182	−0.138 (0.052)	−0.106	−0.015 (–0.083)	−0.072	−0.020 (–0.054)
$4d^{-1}_{3/2}10d^1_{5/2}2^+$	**69.438**	−0.012	0.600 (0.431)	−0.007	−0.911 (0.865)	−0.005	−1.237 (1.625)
$4d^{-1}_{3/2}10d^1_{3/2}2^+$	**69.439**	0.000	−0.112 (0.672)	0.000	−1.071 (–0.361)	0.000	−1.763 (–0.220)
$4d^{-1}_{5/2}10d^1_{5/2}0^+$	**67.393**	0.448	0.000 (0.000)	0.763	0.003 (–0.002)	1.242	0.002 (–0.001)
$4d^{-1}_{3/2}10d^1_{3/2}0^+$	**69.441**	−0.004	0.385 (–0.124)	−0.002	0.072 (0.664)	0.000	0.256 (1.010)
$4d^{-1}_{5/2}11d^1_{3/2}2^+$	**67.437**	0.022	0.000 (0.000)	0.038	0.000 (0.000)	0.063	0.000 (0.000)
$4d^{-1}_{5/2}11d^1_{5/2}2^+$	**67.438**	0.486	0.000 (0.000)	0.809	0.002 (–0.004)	1.267	0.001 (–0.003)
$4d^{-1}_{3/2}11d^1_{5/2}2^+$	**69.487**	−0.010	0.500 (0.273)	−0.005	−0.601 (0.726)	−0.004	−0.746 (1.265)
$4d^{-1}_{3/2}11d^1_{3/2}2^+$	**69.488**	−0.003	−0.024 (0.595)	0.000	−0.952 (–0.196)	0.000	−1.487 (0.000)
$4d^{-1}_{5/2}11d^1_{5/2}0^+$	**67.441**	0.367	0.000 (0.000)	0.609	0.002 (–0.002)	0.953	0.001 (–0.001)
$4d^{-1}_{3/2}11d^1_{3/2}0^+$	**69.489**	−0.004	0.316 (–0.102)	−0.002	0.060 (0.534)	0.000	0.209 (0.786)
$4d^{-1}_{5/2}12d^1_{3/2}2^+$	**67.470**	0.020	0.000 (0.000)	0.035	0.000 (0.000)	0.055	0.000 (0.000)
$4d^{-1}_{5/2}12d^1_{5/2}2^+$	**67.471**	0.408	0.000 (0.000)	0.667	0.002 (–0.003)	1.016	0.001 (–0.003)
$4d^{-1}_{3/2}12d^1_{5/2}2^+$	**69.521**	−0.008	0.420 (0.179)	−0.004	−0.417 (0.613)	−0.003	−0.477 (1.015)
$4d^{-1}_{3/2}12d^1_{3/2}2^+$	**69.521**	−0.004	0.019 (0.520)	0.000	−0.831 (–0.107)	0.000	−1.253 (0.078)
$4d^{-1}_{5/2}12d^1_{5/2}0^+$	**67.474**	0.308	0.000 (0.000)	0.503	0.002 (–0.002)	0.764	0.001 (–0.001)
$4d^{-1}_{3/2}12d^1_{3/2}0^+$	**69.522**	−0.003	0.266 (–0.087)	−0.002	0.052 (0.443)	0.000	0.174 (0.636)
$4d^{-1}_{5/2}13d^1_{3/2}2^+$	**67.496**	−0.011	0.000 (0.000)	−0.017	0.000 (0.000)	−0.023	0.000 (0.000)
$4d^{-1}_{5/2}13d^1_{5/2}2^+$	**67.497**	0.349	0.000 (0.000)	0.564	0.002 (–0.003)	0.842	0.001 (–0.002)
$4d^{-1}_{3/2}13d^1_{5/2}2^+$	**69.546**	−0.007	0.360 (0.177)	−0.004	−0.389 (0.514)	−0.003	−0.449 (0.845)
$4d^{-1}_{3/2}13d^1_{3/2}2^+$	**69.547**	−0.003	0.000 (0.437)	0.000	−0.684 (–0.120)	0.000	−1.019 (0.014)
$4d^{-1}_{5/2}13d^1_{5/2}0^+$	**67.498**	0.263	0.000 (0.000)	0.425	0.001 (–0.002)	0.633	0.001 (–0.001)
$4d^{-1}_{3/2}13d^1_{3/2}0^+$	**69.547**	−0.003	0.228 (–0.075)	−0.001	0.045 (0.375)	−0.001	0.148 (0.530)
$4d^{-1}_{5/2}14d^1_{3/2}2^+$	**67.517**	−0.029	0.000 (0.000)	−0.045	0.000 (0.000)	−0.064	0.000 (0.000)
$4d^{-1}_{5/2}14d^1_{5/2}2^+$	**67.517**	0.302	0.000 (0.000)	0.484	0.002 (–0.002)	0.711	0.001 (–0.002)
$4d^{-1}_{3/2}14d^1_{5/2}2^+$	**69.568**	−0.006	0.313 (0.165)	−0.003	−0.352 (0.439)	−0.002	−0.405 (0.718)
$4d^{-1}_{3/2}14d^1_{3/2}2^+$	**69.567**	−0.002	−0.012 (0.375)	0.000	−0.579 (–0.118)	0.000	−0.856 (–0.012)
$4d^{-1}_{5/2}14d^1_{5/2}0^+$	**67.518**	0.229	0.000 (0.000)	0.366	0.001 (–0.002)	0.537	0.001 (–0.001)
$4d^{-1}_{3/2}14d^1_{3/2}0^+$	**69.568**	−0.003	0.198 (–0.065)	−0.001	0.039 (0.324)	−0.001	0.127 (0.451)
$4d^{-1}_{5/2}15d^1_{3/2}2^+$	**67.533**	0.036	0.000 (0.000)	0.056	0.000 (0.000)	0.081	0.000 (0.000)
$4d^{-1}_{5/2}15d^1_{5/2}2^+$	**67.534**	0.265	0.000 (0.000)	0.421	0.001 (–0.002)	0.612	0.001 (–0.002)
$4d^{-1}_{3/2}15d^1_{5/2}2^+$	**69.584**	0.005	−0.275 (–0.151)	0.003	0.316 (–0.382)	0.002	0.362 (–0.621)
$4d^{-1}_{3/2}15d^1_{3/2}2^+$	**69.584**	−0.002	−0.016 (0.328)	0.000	−0.501 (–0.111)	0.000	−0.734 (–0.023)
$4d^{-1}_{5/2}15d^1_{5/2}0^+$	**67.535**	0.201	0.000 (0.000)	0.319	0.001 (–0.002)	0.464	0.001 (–0.001)
$4d^{-1}_{3/2}15d^1_{3/2}0^+$	**69.584**	−0.002	0.175 (–0.057)	−0.001	0.035 (0.283)	−0.001	0.111 (0.391)
$4d^{-1}_{5/2}16d^1_{3/2}2^+$	**67.547**	0.038	0.000 (0.000)	0.060	0.000 (0.000)	0.085	0.000 (0.000)
$4d^{-1}_{5/2}16d^1_{5/2}2^+$	**67.547**	0.234	0.000 (0.000)	0.370	0.001 (–0.002)	0.534	0.001 (–0.001)
$4d^{-1}_{3/2}16d^1_{5/2}2^+$	**69.597**	0.005	−0.244 (–0.137)	0.003	0.284 (–0.337)	0.002	0.325 (–0.544)
$4d^{-1}_{3/2}16d^1_{3/2}2^+$	**69.597**	−0.002	−0.017 (0.290)	0.000	−0.440 (–0.102)	0.000	−0.641 (–0.028)

Continued on next page

Table A.1 – continued from previous page

state, J^P		$4d^{-1}_{5/2}6p^1$	$4d^{-1}_{3/2}6p^1$	$4d^{-1}_{5/2}7p^1$	$4d^{-1}_{3/2}7p^1$	$4d^{-1}_{5/2}8p^1$	$4d^{-1}_{3/2}8p^1$
	E, eV	**65.110**	**67.039**	**66.375**	**68.345**	**67.150**	**69.150**
GS	**0**	−0.182	−0.138 (0.052)	−0.106	−0.015 (–0.083)	−0.072	−0.020 (–0.054)
$4d^{-1}_{5/2}16d^1_{5/2}0^+$	**67.548**	0.179	0.000 (0.000)	0.282	0.001 (–0.001)	0.407	0.001 (–0.001)
$4d^{-1}_{3/2}16d^1_{3/2}0^+$	**69.597**	−0.002	0.155 (–0.051)	−0.001	0.031 (0.251)	−0.001	0.098 (0.343)
$4d^{-1}_{5/2}17d^1_{3/2}2^+$	**67.557**	0.038	0.000 (0.000)	0.060	0.000 (0.000)	0.084	0.000 (0.000)
$4d^{-1}_{5/2}17d^1_{5/2}2^+$	**67.557**	0.210	0.000 (0.000)	0.330	0.001 (–0.002)	0.472	0.001 (–0.001)
$4d^{-1}_{3/2}17d^1_{5/2}2^+$	**69.607**	0.004	−0.219 (–0.126)	0.002	0.257 (–0.300)	0.002	0.293 (–0.483)
$4d^{-1}_{3/2}17d^1_{3/2}2^+$	**69.608**	−0.001	−0.018 (0.259)	0.000	−0.391 (–0.094)	0.000	−0.567 (–0.030)
$4d^{-1}_{5/2}17d^1_{5/2}0^+$	**67.558**	0.161	0.000 (0.000)	0.252	0.001 (–0.001)	0.361	0.000 (–0.001)
$4d^{-1}_{3/2}17d^1_{3/2}0^+$	**69.608**	−0.002	0.139 (–0.046)	−0.001	0.028 (0.224)	−0.001	0.088 (0.305)
$4d^{-1}_{5/2}18d^1_{3/2}2^+$	**67.566**	0.038	0.000 (0.000)	0.058	0.000 (0.000)	0.082	0.000 (0.000)
$4d^{-1}_{5/2}18d^1_{5/2}2^+$	**67.566**	0.189	0.000 (0.000)	0.296	0.001 (–0.002)	0.422	0.000 (–0.001)
$4d^{-1}_{3/2}18d^1_{5/2}2^+$	**69.616**	0.004	−0.198 (–0.115)	0.002	0.235 (–0.270)	0.001	0.266 (–0.432)
$4d^{-1}_{3/2}18d^1_{3/2}2^+$	**69.616**	−0.001	−0.018 (0.233)	0.000	−0.350 (–0.087)	0.000	−0.506 (–0.031)
$4d^{-1}_{5/2}18d^1_{5/2}0^+$	**67.567**	0.145	0.000 (0.000)	0.227	0.001 (–0.001)	0.323	0.000 (–0.001)
$4d^{-1}_{3/2}18d^1_{3/2}0^+$	**69.616**	−0.002	0.126 (–0.042)	−0.001	0.025 (0.202)	−0.001	0.079 (0.273)
$4d^{-1}_{5/2}19d^1_{3/2}2^+$	**67.573**	0.036	0.000 (0.000)	0.056	0.000 (0.000)	0.079	0.000 (0.000)
$4d^{-1}_{5/2}19d^1_{5/2}2^+$	**67.573**	0.171	0.000 (0.000)	0.268	0.001 (–0.001)	0.380	0.000 (–0.001)
$4d^{-1}_{3/2}19d^1_{5/2}2^+$	**69.623**	0.004	−0.180 (–0.106)	0.002	0.215 (–0.244)	0.001	0.244 (–0.390)
$4d^{-1}_{3/2}19d^1_{3/2}2^+$	**69.623**	−0.001	−0.017 (0.211)	0.000	−0.316 (–0.081)	0.000	−0.456 (–0.031)
$4d^{-1}_{5/2}19d^1_{5/2}0^+$	**67.574**	0.132	0.000 (0.000)	0.206	0.001 (–0.001)	0.292	0.000 (–0.001)
$4d^{-1}_{3/2}19d^1_{3/2}0^+$	**69.623**	−0.002	0.115 (–0.038)	−0.001	0.023 (0.184)	−0.001	0.072 (0.247)

Bibliography

[1] F. Krausz, M. Ivanov, *Rev. Mod. Phys.* **81**, 163 (2009).

[2] A. McPherson, *et al.*, *J. Opt. Soc. Am. B* **4**, 595 (1987).

[3] M. Ferray, *et al.*, *J. Phys. B: At. Mol. Opt. Phys.* **21**, L31 (1988).

[4] P. Corkum, *Phys. Rev. Lett.* **71**, 1994 (1993).

[5] J. Krause, K. Schafer, K. Kulander, *Phys. Rev. Lett.* **68**, 3535 (1992).

[6] P. Paul, *et al.*, *Sci.* **292**, 1689 (2001).

[7] P. Á. Corkum, F. Krausz, *Nat. Phys.* **3**, 381 (2007).

[8] M. Y. Ivanov, M. Spanner, O. Smirnova, *J. Mod. Opt.* **52**, 165 (2005).

[9] S. Popruzhenko, D. Bauer, *J. Mod. Opt.* **55**, 2573 (2008).

[10] W. Becker, X. Liu, P. J. Ho, J. H. Eberly, *Rev. Mod. Phys.* **84**, 1011 (2012).

[11] T. Brabec, F. Krausz, *Rev. Mod. Phys.* **72**, 545 (2000).

[12] D. B. Milošević, G. G. Paulus, D. Bauer, W. Becker, *J. Phys. B: At. Mol. Opt. Phys.* **39**, R203 (2006).

[13] P. Agostini, L. F. DiMauro, *Rep. Prog. Phys* **67**, 813 (2004).

[14] J. M. Dahlström, A. L'Huillier, A. Maquet, *J. Phys. B: At. Mol. Opt. Phys.* **45**, 183001 (2012).

[15] T. Pfeifer, *et al.*, *Chem. Phys. Lett.* **463**, 11 (2008).

[16] A. Kamalov, A. L. Wang, P. H. Bucksbaum, D. J. Haxton, J. P. Cryan, *Phys. Rev. A* **102**, 023118 (2020).

[17] B. Piraux, J. Bauer, S. Laulan, H. Bachau, *Eur. Phys. J. D.* **26**, 7 (2003).

[18] S. Hu, L. Collins, *J. Mod. Opt.* **54**, 943 (2007).

[19] A. H. Winney, *et al.*, *Phys. Rev. Lett.* **119**, 123201 (2017).

[20] F. J. Wuilleumier, M. Meyer, *J. Phys. B: At. Mol. Opt. Phys.* **39**, R425 (2006).

[21] J. Köhler, M. Wollenhaupt, T. Bayer, C. Sarpe, T. Baumert, *Opt. Express* **19**, 11638 (2011).

[22] K. Ramasesha, S. R. Leone, D. M. Neumark, *Annu. Rev. Phys. Chem* **67**, 41 (2016). PMID: 26980312.

[23] L. Keldysh, *Sov. Phys. J. Exp. Theor. Phys.* **20**, 1307 (1965).

[24] T. Topcu, F. Robicheaux, *Phys. Rev. A* **86**, 053407 (2012).

[25] S. H. Southworth, *et al.*, *Phys. Rev. A* **76**, 043421 (2007).

[26] Z.-H. Loh, *et al.*, *Phys. Rev. Lett.* **98**, 143601 (2007).

[27] L. Young, *et al.*, *Phys. Rev. Lett.* **97**, 083601 (2006).

[28] R. Santra, R. W. Dunford, L. Young, *Phys. Rev. A* **74**, 043403 (2006).

[29] P. Johnsson, J. Mauritsson, T. Remetter, A. L'Huillier, K. Schafer, *Phys. Rev. Lett.* **99**, 233001 (2007).

[30] T. Glover, *et al.*, *Nat. Phys.* **6**, 69–74 (2009).

[31] P. Ranitovic, *et al.*, *New J. Phys.* **12**, 013008 (2010).

[32] M. Wickenhauser, J. Burgdörfer, F. Krausz, M. Drescher, *Phys. Rev. Lett.* **94**, 023002 (2005).

[33] C. Buth, R. Santra, L. Young, *Phys. Rev. Lett.* **98**, 253001 (2007).

[34] R. Santra, *et al.*, *J. Phys.: Conf. Ser.* **88**, 012052 (2007).

[35] C. Buth, R. Santra, *Phys. Rev. A* **75**, 033412 (2007).

[36] C. Buth, R. Santra, *Phys. Rev. A* **78**, 043409 (2008).

[37] N. Tamai, H. Miyasaka, *Chem. Rev.* **100**, 1875–1890 (2000).

[38] A. G. Joly, K. A. Nelson, *J. Phys. Chem.* **93**, 2876 (1989).

[39] T. Pfeifer, C. Spielmann, G. Gerber, *Rep. Prog. Phys.* **69**, 443 (2006).

[40] A. H. Zewail, *J. Phys. Chem. A* **104**, 5660 (2000).

[41] L. Dhar, J. A. Rogers, K. A. Nelson, *Chem. Rev.* **94**, 157–193 (1994).

[42] H. Petek, S. Ogawa, *Prog. Surf. Sci.* **56**, 239 (1997).

[43] A. Othonos, *J. Appl. Phys.* **83**, 1789 (1998).

[44] C. Voisin, N. Fatti, D. Christofilos, F. Vallee, *J. Phys. Chem. B* **105**, 2264–2280 (2001).

[45] A. Stolow, A. Bragg, D. Neumark, *Chem. Rev.* **104**, 1719–1758 (2004).

[46] K. Sokolowski-Tinten, D. Von Der Linde, *J. Phys.: Condens. Matter* **16**, R1517 (2004).

[47] J. Güdde, U. Höfer, *Prog. Surf. Sci.* **80**, 49 (2005).

[48] E. Nibbering, H. Fidder, E. Pines, *Annu. Rev. Phys. Chem.* **56**, 337 (2005).

[49] P. Kukura, D. McCamant, R. Mathies, *Annu. Rev. Phys. Chem.* **58**, 461 (2007).

[50] M. Gühr, M. Bargheer, M. Fushitani, T. Kiljunen, N. Schwentner, *Phys. Chem. Chem. Phys.* **9**, 779 (2007).

[51] V. Sundstrom, *Annu. Rev. Phys. Chem.* **59**, 53 (2008).

[52] J.-C. Diels, W. Rudolph, *Ultrashort laser pulse phenomena* (Elsevier, 2006).

[53] C. Rullière, T. Amand, X. Marie, *Femtosecond laser pulses* (Springer, 1998), pp. 203–259.

[54] J. Manz, L. Wöste, *Femtosecond chemistry*, vol. 2 (VCH, 1995).

[55] M. Lorenc, *et al.*, *Appl. Phys. B* **74**, 19 (2002).

[56] V. I. Klimov, D. W. McBranch, *Phys. Rev. Lett.* **80**, 4028 (1998).

[57] J. Aßmann, M. Kling, B. Abel, *Angew. Chem. Int. Ed.* **42**, 2226 (2003).

[58] M. Dantus, M. J. Rosker, A. H. Zewail, *J. Chem. Phys.* **87**, 2395 (1987).

[59] E. Goulielmakis, *et al.*, *Nat.* **466**, 739 (2010).

[60] R. Santra, V. Yakovlev, T. Pfeifer, Z.-H. Loh, *Phys. Rev. A* **83**, 033405 (2011).

[61] J. Mauritsson, *et al.*, *Phys. Rev. Lett.* **105**, 053001 (2010).

[62] M. Holler, F. Schapper, L. Gallmann, U. Keller, *Phys. Rev. Lett.* **106**, 123601 (2011).

[63] C. Ott, *et al.*, *Nat.* **516**, 374 (2014).

[64] C. Ott, *et al.*, *Phys. Rev. Lett.* **123**, 163201 (2019).

[65] N. Shivaram, X.-M. Tong, H. Timmers, A. Sandhu, *J. Phys. B: At. Mol. Opt. Phys.* **49**, 055601 (2016).

[66] A. Beck, *et al.*, *New J. Phys.* **16**, 113016 (2014).

[67] W. Cao, E. Warrick, D. Neumark, S. Leone, *New J. Phys.* **18**, 013041 (2016).

[68] D. Kolbasova, R. Santra, *Appl. Sci.* **9**, 1350 (2019).

[69] D. Kolbasova, *et al.*, *Phys. Rev. A* **103**, 043102 (2021).

[70] A. Blättermann, C. Ott, A. Kaldun, T. Ding, T. Pfeifer, *J. Phys. B: At. Mol. Opt. Phys.* **47**, 124008 (2014).

[71] S. Pabst, *et al.*, *Phys. Rev. A* **86**, 063411 (2012).

[72] J. Baggesen, E. Lindroth, L. Madsen, *Phys. Rev. A* **85**, 013415 (2012).

[73] L. Gallmann, *et al.*, *Mol. Phys.* **111**, 2243–2250 (2013).

[74] M. Wu, S. Chen, S. Camp, K. Schafer, M. Gaarde, *J. Phys. B* **49**, 062003 (2016).

[75] S. Mukamel, R. Loring, *J. Opt. Soc. Am. B* **3**, 595 (1986).

[76] S. Mukamel, *Phys. Rev. A* **77**, 023801 (2008).

[77] C. A. Marx, U. Harbola, S. Mukamel, *Phys. Rev. A* **77**, 022110 (2008).

[78] J. Biggs, J. Voll, S. Mukamel, *Phil. Trans. R. Soc. A* **370**, 3709 (2012).

[79] A. Rudenko, *et al.*, *Nature* **546**, 129 (2017).

[80] L. Greenman, *et al.*, *Phys. Rev. A* **82**, 023406 (2010).

[81] S. Pabst, L. Greenman, P. J. Ho, D. A. Mazziotti, R. Santra, *Phys. Rev. Lett.* **106**, 053003 (2011).

[82] G. Floquet, *Ann. Sci. Éc. Norm. Supér.* **12**, 47 (1883).

[83] S. Chen, *et al.*, *Phys. Rev. A* **86**, 063408 (2012).

[84] S. Chen, M. Wu, M. Gaarde, K. Schafer, *Phys. Rev. A* **87**, 033408 (2013).

[85] A. Beck, D. Neumark, S. Leone, *Chem. Phys. Lett.* **624**, 119 (2015).

[86] H. Paul, *Opt. Quantum Electron.* **28**, 1111 (1996).

[87] G. C. King, M. Tronc, F. H. Read, R. C. Bradford, *J. Phys. B: At. Mol. Phys.* **10**, 2479 (1977).

[88] D. H. Sampson, H. L. Zhang, A. K. Mohanty, R. E. Clark, *Phys. Rev. A* **40**, 604 (1989).

[89] H. L. Zhang, D. H. Sampson, A. K. Mohanty, *Phys. Rev. A* **40**, 616 (1989).

[90] M. F. Gu, *Can. J. Phys.* **86**, 675 (2008).

[91] M.-F. Lin, A. N. Pfeiffer, D. M. Neumark, S. R. Leone, O. Gessner, *J. Chem. Phys.* **137**, 244305 (2012).

[92] S. Masui, E. Shigemasa, A. Yagishita, I. A. Sellin, *J. Phys. B: At. Mol. Opt. Phys.* **28**, 4529 (1995).

[93] T. Ding, *et al.*, *Opt. Lett.* **41**, 709 (2016).

[94] M. Miranda, T. Fordell, C. L. Arnold, A. L'Huillier, H. Crespo, *Opt. Express* **20**, 688 (2012).

[95] M. Miranda, *et al.*, *Opt. Express* **20**, 18732 (2012).

[96] V. Stooß, *et al.*, *Rev. Sci. Instrum.* **90**, 053108 (2019).

[97] T. Koizumi, *et al.*, *Phys. Scr.* **1997**, 131 (1997).

[98] D. Ederer, M. Manalis, *J. Opt. Soc. Am.* **65**, 634 (1975).

[99] S. G. Sayres, E. R. Hosler, S. R. Leone, *J. Phys. Chem. A* **118**, 8614 (2014).

[100] M. Sabbar, *et al.*, *Nat. Phys.* **13**, 472 (2017).

[101] M. Geissler, *et al.*, *Phys. Rev. Lett.* **83**, 2930 (1999).

[102] J.-H. Kim, C. H. Nam, *Phys. Rev. A* **65**, 033801 (2002).

[103] M. Hentschel, *et al.*, *Nat.* **414**, 509 (2001).

[104] M. B. Gaarde, M. Murakami, R. Kienberger, *Phys. Rev. A* **74**, 053401 (2006).

[105] A. Goldberg, B. W. Shore, *J. Phys. B: At. Mol. Opt. Phys.* **11**, 3339 (1978).

[106] C. Leforestier, R. E. Wyatt, *J. Chem. Phys.* **78**, 2334 (1983).

[107] G. Jolicard, E. J. Austin, *Chem. Phys. Lett.* **121**, 106 (1985).

[108] U. V. Riss, H. D. Meyer, *J. Phys. B: At. Mol. Opt. Phys.* **26**, 4503 (1993).

[109] R. Santra, L. S. Cederbaum, *Phys. Rep.* **368**, 1 (2002).

[110] J. Muga, J. Palao, B. Navarro, I. Egusquiza, *Phys. Rep.* **395**, 357 (2004).

[111] C. Zhang, Y. Ma, *Ensemble machine learning: methods and applications* (Springer, 2012).

[112] F. Pedregosa, *et al.*, *J. Mach. Learn. Res.* **12**, 2825 (2011).

[113] J. Benesty, J. Chen, Y. Huang, I. Cohen, *Noise reduction in speech processing* (Springer, 2009).

Acknowledgements

First of all, I would like to express my sincere gratitude to my supervisor Professor Robin Santra for the inspiration and support that he gave me in the study of the quantum world. A rare and very precious feature, the ability to combine a great interest and love for science with a knowing the human nature helped Robin to bring together such a wonderful group, to challenge and always inspire each of us in our studies and continuously push forward the boundaries of human knowledge.

I am also grateful to our co-authors on the experimental side for inviting me to work on interesting projects and explaining the technical side of the experiment: Thomas Pfeifer, Christian Ott, Maximillian Hartmann and Alexander Blättermann with their ATAS experiment on the Xe atom; and Francesca Calegari together with Andrea Trabattoni, who suggested to use Ar multiphoton autocorrelation to characterize a laser pulse.

I would like to thank my co-supervisors Sang-Kil Son and Zoltan Jurek for being always welcome for discussion, raising up new interesting questions during my research and guiding me with finding the answers. They were the first people from our group whom I met, who fished me out from the summer student crowd and showed me CFEL - with University of Hamburg on a first floor, Max Planck Society at the second and Deutsches Elektronen-Synchrotron (DESY) - on the top!

My thanks also go to my colleagues, in particular to Antonia Karamatskou, Otfried Geffert, Ludger Inhester, John Bekx, Vladimir Lipp, Rui Jin and Julia Schäfer. Especially I would like to thank my good friend Malik Abdullah for his help and support in difficult situations and for teaching me programming.

Finally, I thank my former supervisor Professor Alexei Grum-Grzhimailo and my best friend Lilia Imasheva, without whom I would hardly have found the way to DESY and had the luck to join Robin Santra's group.